TURUN YLIOPISTON JULKAISUJA
ANNALES UNIVERSITATIS TURKUENSIS

SARJA - SER. A I OSA - TOM. 473

ASTRONOMICA - CHEMICA - PHYSICA - MATHEMATICA

RESEARCH AND DEVELOPMENT OF III-V SEMICONDUCTOR SURFACES FOR IMPROVED DEVICE INTERFACES

by

Jouko Lång

TURUN YLIOPISTO
UNIVERSITY OF TURKU
Turku 2013

From the Materials Research Laboratory
Department of Physics and Astronomy
University of Turku
Turku, Finland

and

National Graduate School of Materials Physics,
Helsinki, Finland

Supervised by

Docent Pekka Laukkanen
Department of Physics and Astronomy
University of Turku
Turku, Finland

Docent Marko Punkkinen
Department of Physics and Astronomy
University of Turku
Turku, Finland

Reviewed by

Professor Peter Liljeroth
Department of Applied Physics
Aalto University School of Science
Espoo, Finland

Professor Matti Alatalo
Department of Mathematics and Physics
Lappeenranta University of Technology
Lappeenranta, Finland

Opponent

Professor Robert M. Wallace
Department of Materials Science and Engineering
University of Texas at Dallas
Dallas, United States

ISBN 978-951-29-5543-5 (PRINT)
ISBN 978-951-29-5544-2 (PDF)
ISSN 0082-7002
Painosalama Oy – Turku, Finland 2013

Contents

Acknowledgments

This thesis would not exist without the guidance, professionalism, support and patience of wonderful people I have had the pleasure of working and living with through the making of this work. First, I would like to express my sincere gratitude to professor emeritus Juhani Väyrynen who saw some potential in me and took me as a summer trainee in the Materials Research Laboratory, Department of Physics and Astronomy, University of Turku in 2008. The rest is history. I also wish to acknowledge the National Graduate School of Materials Physics and Solar III-V project of the Academy of Finland for the financial support.

The work presented in this thesis was carried out in the years 2009-2013 and two wonderful individuals and professionals made the most substantial contribution to this research and the results within; my supervisors Pekka Laukkanen and Marko Punkkinen. Pekka's overwhelming positive attitude to our research has kept the work meaningful to me. Moreover, Marko has taught me the scientific approach to work. I would like to thank our current professor Kalevi Kokko for valuable and important discussions and advice I have received from him. The entire group of Materials Physics is acknowledged for providing me the fruitful and the most pleasant place to work. I also wish to thank the staff of MAX-lab, Lund University Sweden for offering the most pleasant usage of the fanciest thing I have ever seen: a synchrotron. The staff of Optoelectronic Research Centre, Tampere Finland is acknowledged for making the world-class quality MBE films and processing our samples. Special thanks to professor emeritus Markus Pessa for the valuable discussions we have had.

I am honored to have professor Robert M. Wallace as an opponent and I express my sincere gratitude to him. Professors Peter Liljeroth and Matti Alatalo are acknowledged for carefully reviewing this thesis.

I am truly indebted to my loving family, including mother, father and my sister Piia for their loving care and support through the years. Finally, my deepest gratitude goes to my dear wife Satu and our three wonderful and the most extraordinary children: Anton, Ville and Sofia. Without you, all this would be meaningless. I especially thank Satu for keeping me sane and reminding me that there are other things in the world apart from physics.

Abstract

This thesis is devoted to understanding and improving technologically important III-V compound semiconductor (e.g. GaAs, InAs, and InSb) surfaces and interfaces for devices. The surfaces and interfaces of crystalline III-V materials have a crucial role in the operation of field-effect-transistors (FET) and high-efficiency solar-cells, for instance. However, the surfaces are also the most defective part of the semiconductor material and it is essential to decrease the amount of harmful surface or interface defects for the next-generation III-V semiconductor device applications. Any improvement in the crystal ordering at the semiconductor surface reduces the amount of defects and increases the material homogeneity. This is becoming more and more important when the semiconductor device structures decrease to atomic-scale dimensions. Toward that target, the effects of different adsorbates (i.e., Sn, In, and O) on the III-V surface structures and properties have been investigated in this work. Furthermore, novel thin-films have been synthesized, which show beneficial properties regarding the passivation of the reactive III-V surfaces.

The work comprises ultra-high-vacuum (UHV) environment for the controlled fabrication of atomically ordered III-V(100) surfaces. The surface sensitive experimental methods [low energy electron diffraction (LEED), scanning tunneling microscopy/spectroscopy (STM/STS), and synchrotron radiation photoelectron spectroscopy (SRPES)] and computational density-functional-theory (DFT) calculations are utilized for elucidating the atomic and electronic properties of the crucial III-V surfaces. The basic research results are also transferred to actual device tests by fabricating metal-oxide-semiconductor capacitors and utilizing the interface sensitive measurement techniques [capacitance voltage (CV) profiling, and photoluminescence (PL) spectroscopy] for the characterization. This part of the thesis includes the instrumentation of home-made UHV-compatible atomic-layer-deposition (ALD) reactor for growing good quality insulator layers.

The results of this thesis elucidate the atomic structures of technologically promising Sn- and In-stabilized III-V compound semiconductor surfaces. It is shown that the Sn adsorbate induces an atomic structure with (1×2)/(1×4) surface symmetry which is characterized by Sn-group III dimers. Furthermore, the stability of peculiar ζa structure is demonstrated for the GaAs(100)-In surface. The beneficial effects of these surface structures regarding the crucial III-V oxide interface are demonstrated. Namely, it is found that it is possible to passivate the III-V surface by a careful atomic-scale engineering of the III-V surface prior to the gate-dielectric deposition. The thin (1×2)/(1×4)-Sn layer is found to catalyze the removal of harmful amorphous III-V oxides. Also, novel crystalline III-V-oxide structures are synthesized and it is shown that these structures improve the device characteristics. The finding of crystalline oxide structures is exploited by solving the atomic structure of InSb(100)(1×2) and elucidating the electronic structure of oxidized InSb(100) for the first time.

List of papers

The research presented in this thesis consists of experimental work carried out at the Materials Research Laboratory, Department of Physics and Astronomy, University of Turku, Finland and at the MAX-lab synchrotron-radiation research center, Lund University, Sweden. The considerable computational work of this thesis was carried out by using the computational capacity offered by CSC-IT Centre for Science, Finland and the capacity of Finnish Grid Infrastructure (FGI). This thesis consists of the introductory review and the following six papers to which I have contributed.

1 **J. J. K. Lång**, P. Laukkanen, M. P. J. Punkkinen, M. Ahola-Tuomi, M. Kuzmin, V. Tuominen, J. Dahl, M. Tuominen, R. Perälä, K. Schulte, J. Adell, J. Sadowski, J. Kanski, M. Guina, M. Pessa, K. Kokko, B. Johansson, L. Vitos, and I. J. Väyrynen: *Tin-stabilized (1×2) and (1×4) reconstructions on GaAs(100) and InAs(100) studied by scanning tunneling microscopy, photoelectron spectroscopy, and ab initio calculations*. Surface Science **605**, 883 (2011).

2 P. Laukkanen, M. P. J. Punkkinen, **J. Lång**, M. Kuzmin, M. Tuominen, V. Tuominen, J. Dahl, J. Adell, J. Sadowski, J. Kanski, V. Polojärvi, J. Pakarinen, K. Kokko, M. Guina, M. Pessa, and I. J. Väyrynen: *Ultrathin (1×2)-Sn layer on GaAs(100) and InAs(100) substrates: A catalyst for removal of amorphous surface oxides.* Applied Physics Letters **98**, 231908 (2011).

3 **J. J. K. Lång**, M. P. J. Punkkinen, P. Laukkanen, M. Kuzmin, V. Tuominen, M. Pessa, M. Guina, I. J. Väyrynen, K. Kokko, B. Johansson and L. Vitos: *Ab initio and scanning tunneling microscopy study of indium-terminated GaAs(100) surface: An*

indium induced surface reconstruction change in the c(8×2) structure. Physical Review B **81**, 245305 (2010).

4 M. P. J. Punkkinen, P. Laukkanen, **J. Lång**, M. Kuzmin, M. Tuominen, V. Tuominen, J. Dahl, M. Pessa, M. Guina, K. Kokko, J. Sadowski, B. Johansson, I. J. Väyrynen, and L. Vitos: *Oxidized In-containing III-V(100) surfaces: Formation of crystalline oxide films and semiconductor-oxide interface.* Physical Review B **83**, 195329 (2011).

5 Pekka Laukkanen, **Jouko Lång**, Marko Punkkinen, Mikhail Kuzmin Marjukka Tuominen, Muhammad Yasir, Johnny Dahl, Veikko Tuominen, Kalevi Kokko, Ville Polojärvi, Joel Salmi, Ville-Markus Korpijärvi, Arto Aho, Antti Tukiainen, Mircea Guina, Hannu-Pekka Hedman, and Risto Punkkinen: *Synthesis and Characterization of Monocrystalline Tin-Oxide Thin Films on III-V Compound Semiconductor.* Submitted in July 2013

6 **J. J. K. Lång,** M. P. J. Punkkinen, M. Tuominen, H.-P. Hedman, M. Vähä-Heikkilä, V. Polojärvi, J. Salmi, V.-M. Korpijärvi, K. Schulte, M. Kuzmin, M. Guina, K. Kokko, R. Punkkinen, and P. Laukkanen: *Atomic scale engineering of oxide/semiconductor interfaces for improved transistors.* Submitted in October 2013.

My contribution to the papers is as follows: for papers 1, 3 and 6, I had the main responsibility of sample preparations, scanning tunneling microscopy and photoelectron spectroscopy experiments, *ab initio* calculations and writing the manuscripts. For papers 2 and 5 I contributed to sample preparations and experiments. In paper 4, I and docent Laukkanen discovered, for the first time, the formation of the oxygen induced surface reconstructions and I contributed

to further sample preparations, scanning tunneling microscopy and photoelectron spectroscopy experiments and *ab initio* calculations.

The following publications and patent application included my contribution and are related to this work but are not included in the thesis.

- M. Kuzmin, M.P.J. Punkkinen, P. Laukkanen, R.E. Perälä, J.J.K. Lång, J. Dahl, J. Adell, K. Kokko: *Photoemission and density functional theory study of Ge(100): Clean surface and Yb-induced (2×4) reconstruction,* Surface Science **615**, 88-96 (2013).

- M.P.J. Punkkinen, P. Laukkanen, J. Lång, M. Kuzmin, J. Dahl, H. L. Zhang, M. Pessa, M. Guina, L. Vitos, and K. Kokko: *Structure of ordered oxide on InAs(100) surface*, Surface Science **606**, 1837-1841 (2012)

- A. Duzik, J. C. Thomas, J. Millunchick, J. Lång, M. P. J. Punkkinen, and P. Laukkanen: *Surface structure of bismuth terminated GaAs surfaces grown with molecular beam epitaxy.* Surface Science **606**, 1203-1207 (2012).

- M. Kuzmin, M. P. J. Punkkinen, P. Laukkanen, J. J. K. Lång, J. Dahl, M. Tuominen, V. Tuominen, J. Adell, T. Balasubramanian, L. Vitos, and K. Kokko: *Dimer-T_3 reconstruction on the Sm/Si(100)(2×3) surface studied by high-resolution photoelectron spectroscopy and density functional theory calculations.* Physical Review B **84**, 245322 (2011).

- M. Kuzmin, M. P. J. Punkkinen, P. Laukkanen, J. J. K. Lång, J. Dahl, V. Tuominen, M. Tuominen, R. E. Perälä, T. Balasubramanian, J. Adell, K. Kokko, and, I. J. Väyrynen: *Surface core-level shifts on Ge(111)c(2×8): Experiment and theory.* Physical Review B **83**, 245319 (2011).

- M. Ahola-Tuomi, M. P. J. Punkkinen, P. Laukkanen, M. Kuzmin, J. Lång, K. Schulte, N. Räsänen, A. Pietzsch, R. E. Perälä and I. J. Väyrynen: *Properties of self-assembled Bi nanolines on InAs(100) studied by core-level and valence-band photoemission, and first principles calculations.* Physical Review B **83**, 245401 (2011).

- P. Laukkanen, J. Lång, V. Tuominen, J. Dahl, M. Tuominen, M. Punkkinen, J. Väyrynen, Patent application: PCT/FI2011/050991, European Patent Office (2011).

- M. Kuzmin, M.P.J. Punkkinen, P. Laukkanen, R.E. Perälä, V. Tuominen, J.J.K. Lång, M. Ahola-Tuomi, J. Dahl, T. Balasubramanian, B. Johansson, L. Vitos, and I. J. Väyrynen: *Atomic structure of Yb/Si(100)(2×6): Interrelation between the silicon dimer arrangement and Si 2p photoemission line shape.* Physical Review B **82**, 113302 (2010).

- P. Laukkanen, M.P.J. Punkkinen, N. Räsänen, M. Ahola-Tuomi, J. Sadowski, J. Adell, M. Kuzmin, J. Lång, R.E. Perälä, M. Ropo, K. Kokko, L. Vitos, B. Johansson, M. Pessa and I. J. Väyrynen: *Bismuth-stabilized c(2×6) reconstruction on InSb(100) substrate*: Violation of the electron counting model. Physical Review B **81,** 035310 (2010).

- P. Laukkanen, M. P. J. Punkkinen, M. Ahola-Tuomi, J. Lång, K. Schulte, A. Pietzsch, M. Kuzmin, J. Sadowski, J. Adell, R. E. Perälä, M. Ropo, K. Kokko, L. Vitos, B. Johansson, M. Pessa and I. J. Väyrynen: *Core-level shifts of the c(8×2)-reconstructed InAs(100) and InSb(100) surfaces.* Journal of Electron Spectroscopy and Related Phenomena, **177** 52-57 (2010).

- M. Kuzmin, P. Laukkanen, R. E. Perälä, M. P. J. Punkkinen, M. Ahola-Tuomi, J. Lång and I. J. Väyrynen: *Stability, structural and electronic properties of atomic chains on Yb/Ge(111)(3×2) studied by STM and STS.* Physical Review B **81,** 155312 (2010).

- V. Polojärvi, J. Salmi, A. Schramm, A. Tukiainen, M. Guina, J. Pakarinen, E. Arola, J. Lång, I. J. Väyrynen, and P. Laukkanen: *Effects of $(NH_4)_2S$ and NH_4OH surface treatments prior to SiO_2 capping and thermal annealing on 1.3 μm GaInAsN/GaAs quantum well structures.* Applied Physics Letters **97**, 111109 (2010).

- M. P. J. Punkkinen, P. Laukkanen, M. Ahola-Tuomi, J. Pakarinen, M. Kuzmin, A. Tukiainen, R.E. Perälä, J. Lång, M. Ropo, K. Kokko, L. Vitos, B. Johansson, M. Pessa and I. J. Väyrynen: *Core-level shifts of InP(100)(2×4) surface: Theory and experiment.* Surface Science, **603,** 2664 (2009).

- M. P. J. Punkkinen, M. Kuzmin, P. Laukkanen, R. E. Perälä, M. Ahola-Tuomi, J. Lång, M. Ropo, K. Kokko, M. Pessa, I. J. Väyrynen, B. Johansson and L. Vitos: *Stability and structure of rare earth metal and Ba-induced reconstructions on a Si(100) surface.* Physical Review B **80**, 235307 (2009).

Dedicated to the memory of my beloved son,

Veeti

1 Introduction

"Science is the belief in the ignorance of experts"
- Richard Feynman

The revolution of modern technology began in 1947 with the demonstration of first solid state transistor by William Shockley, John Bardeen and Walter Brattain. The first transistor was composed of elemental semiconductor material germanium and two gold contacts. Since then, the rapid development of semiconductor materials and technology have resulted in a variety of electronic and optoelectronic devices which affect our everyday life more than any other innovation has done so far. Although the semiconductor devices have been studied for at least 130 years, the past 60 years have been the triumph of semiconductor technology; during that time the remarkable success and enormous influence on the world economy have been achieved. The keystone for semiconductor technology has been the miniaturizing of the functional semiconductor components in circuits. This is especially true for integrated circuit (IC) technology. Moore's law emboldened scaling of the complementary metal oxide semiconductor (CMOS) transistors has challenged the industrial and academic researchers and engineers for decades.[1-7] The first microprocessor chip was produced by Intel in 1971 and it contained 2300 transistors (per chip). The most recent chip (Ivy Bridge, 2012, Intel) includes as much as 1.4 billion transistors.

The motivation for the aggressive transistor scaling is the increasing amount of functionality within the area of the chip, decreasing switching times, higher clock frequencies and lower power dissipation. However, the technology of logic transistors is coming to a major turning point within a few years as the scaling will face its fundamental limits when the sizes of the smallest structures (i.e., the thickness of the gate oxide film) reaches atomic-scale dimensions.

This has drawn an intensive research for alternative solutions to improve these devices. There is a consensus among researchers that the transistor channel material has to be changed from silicon, which is without any doubt the most dominant material in semiconductor industry, to another material (materials) in order to further enhance the electrical performance of the transistors.

The most potential successors to silicon, in short term CMOS applications and also in long term "beyond CMOS" technology, are III-V compound semiconductors,[1-7] which are already widely used in analog and optoelectronic technology. However, the introduction of new channel material is not straightforward at all, as it is explained in the following chapters. As the dimensions of functional electronic components decrease, the atomic-scale properties of the materials become more and more important. Therefore, the research of the atomic and electronic structures of semiconductor materials is essential in order to achieve a fundamental understanding about these materials and in turn, to develop novel solutions for the devices. Furthermore, the operation of semiconductor devices is, to a large extent, based on the interfaces between different materials. Therefore, the physics of solid surfaces and interfaces, a branch of condensed matter physics, is at central stage for the device development.

In this work, a multitude of experimental surface science techniques are combined with computational methods in order to understand and elucidate the atomic and electronic properties of technologically important III-V compound semiconductor surfaces. It is shown that some III-V surface atomic structures have very useful and perhaps drastic properties regarding, for example, the transistor development. Furthermore, a step from basic research towards device applications is taken in the framework of metal-oxide-semiconductor capacitor (MOSCAP) fabrication and their characterization.

This thesis is organized as follows; Chapter 1 covers the general properties of the III-V compound semiconductors, their surfaces and the impact of surface

reconstructions for device applications. In Chapter 2, the experimental and computational methods are concerned. The results of the papers included in this thesis are summarized in Chapter 3 with discussion. Finally, conclusions are given in Chapter 4.

1.1 General remarks of III-V compound semiconductors and applications

Compound semiconductors are materials, classified according to the elemental groups of their constituents in the periodic table. In general, these compounds can be categorized as binary, ternary or quaternary etc. alloys depending on the number of different atomic constituents making the crystal. The binary III-V compounds include a group III element (B, Al, Ga, In or Tl) and a group V element (N, P, As, Sb or Bi) of the periodic table. For example, GaAs, InAs, InSb, InP and AlAs are binary III-V alloys. Furthermore, $In_xGa_{1-x}As$ and $Al_xGa_{1-x}As$ are examples of ternary III-V compounds which play important role in the so-called band-gap engineering of the semiconductor materials.

In III-V crystals, the outer s^2p^1 valence orbitals of group III atoms overlap with the outer s^2p^3 valence orbitals of group V atoms making sp^3 type bonding hybrid orbitals, mainly covalent of character. The resulting linear combinations of spherical s-type orbital and more directional p-type orbital have a tetrahedral coordination. Therefore, the III-V compounds usually crystallize in cubic zincblende structure with two-atom basis at $\vec{0}$ and $\frac{a}{4}(\hat{x}+\hat{y}+\hat{z})$, where a is the lattice constant of the crystal.[8,9] Due to electronegativity differences between the constituent elements, the III-V compound also has an ionic bonding character. The zincblende structure, illustrated in Fig. 1, is the most common structure among the III-V semiconductors, but some III-V compounds (e.g., GaN) have hexagonal wurtzite structure or they can crystallize into both phases depending on the preparation conditions.

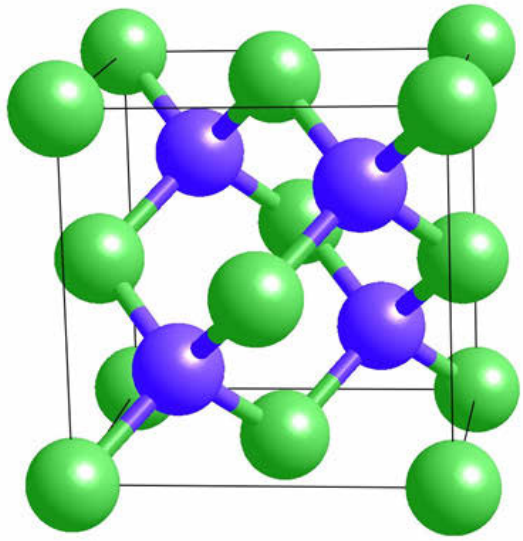

Figure 1. *Zincblende structure of the III-V compound semiconductor. Blue spheres can be As atoms and green spheres can be Ga atoms for example.*

The electronic structures of the III-V compounds, which largely determine the device characteristics, are very versatile among the different III-V compounds. Table I summarizes the basic electronic properties of different semiconductors at 300 K. In general, the energy separation between the highest occupied energy band (i.e., valence band maximum, VBM) and the lowest unoccupied band (i.e., conduction band minimum, CBM) determines the forbidden energy band gap E_G, which can be direct or indirect depending on the relative location of the CBM and VBM in the Brillouin zone of the reciprocal space. Most of the III-V compound semiconductors have direct band gap, in contrast to elemental Si and Ge semiconductors. The direct band gap enables various device applications, most notably the light-emitting ones, due to the allowance of direct optical transitions without the involvement of phonon induced change in the crystal momentum. In addition, the III-V compounds have small electron effective masses compared with many other semiconductors. Since the charge carrier velocity is inversely proportional to the effective mass of electrons or holes in crystal, the III-V materials have very high carrier mobilities which make them suitable materials for high speed and high frequency device applications.

For example, the modern mobile-phone technology relies much on the III-V material -based high-electron-mobility transistors (HEMT) in radio-frequency (RF) applications.

Table I. *The energy band gaps and the effective masses for selected elemental and compound semiconductors at 300 K. Electron and hole masses are presented relative to free electron mass and m_t and m_l denote the transverse and longitudinal effective masses of electrons while m_{lh} and m_{hh} denote the light hole and heavy hole masses respectively. The data is from Refs. 9 and 10.*

Element	E_G(eV)	Electron mass	Hole mass
Si	1.12	m_t=0.19 m_l=0.97	m_{lh}=0.16 m_{hh}=0.50
Ge	0.64	m_t=0.082 m_l=1.6	m_{lh}=0.04 m_{hh}=0.30
GaAs	1.43	0.068	m_{lh}=0.074 m_{hh}=0.62
AlAs	2.16	m_l=2.0	m_{lh}=0.15 m_{hh}=0.76
GaP	2.26	m_t=0.22 m_l=1.12	m_{lh}=0.14 m_{hh}=0.79
GaSb	0.72	0.045	m_{lh}=0.074 m_{hh}=0.62
InAs	0.33	0.023	m_{lh}=0.027 m_{hh}=0.60
InP	1.29	0.08	m_{lh}=0.089 m_{hh}=0.85
InSb	0.16	0.014	m_{lh}=0.027 m_{hh}=0.60

Another technologically attractive property of the III-V semiconductors is the capability of preparing heteroepitaxial lattice-matched ternary or quaternary III-V film stacks.[11] This property enables to explicitly tailor many electrical and physical properties of the device. With the “band-gap engineering” of the semiconductor heterostructures, it is possible to fabricate various devices ranging from lasers and detectors to aforementioned high speed transistors. For example, the quantum well lasers are produced (grown) epitaxially, in such a way that the different band gap material films form for example GaAs-InGaAs-

GaAs quantum well structure where the recombination of electrons and holes occurs when the voltage over the pn-junction (including quantum wells) is applied. Quantum well lasers outperform the conventional laser diodes with very high efficiency. Schematic structure and band diagram of such device is shown in Fig. 2. In addition, high-efficiency solar cells can be fabricated by manufacturing multijunction III-V heterostructures to absorb a large bandwidth of the broad solar spectrum. It is important to note that the above mentioned film stacks are well crystalline and all epitaxial layers have the same lattice-plane as the bottom substrate (the perpendicular lattice constant along the film growth direction can change).

The common target in the research and development of these materials for devices is to improve the crystal quality. Any improvement in the crystal ordering in the films and at their interfaces will decrease the density of harmful interface defects. Taking the quantum well laser as an example, the poor quality (for example structural disorder) of the GaAs-InGaAs interface would disturb the band structure between the materials producing undesirable recombination centers and non-abrupt density of states distribution which ultimately leads to the loss of electron-hole pairs and decoherence of the light emitted. In order to avoid such hindrances, the monitoring and precise control of the crystal growth in very clean vacuum conditions is essential for device development. Since the epitaxial growth of III-V device materials (Molecular Beam Epitaxy, MBE)[11] proceeds via surface reconstructions, the understanding of the atomic and electronic properties of different reconstructions is important for further device development. A role of semiconductor reconstructions is described in more detail in the next Chapter.

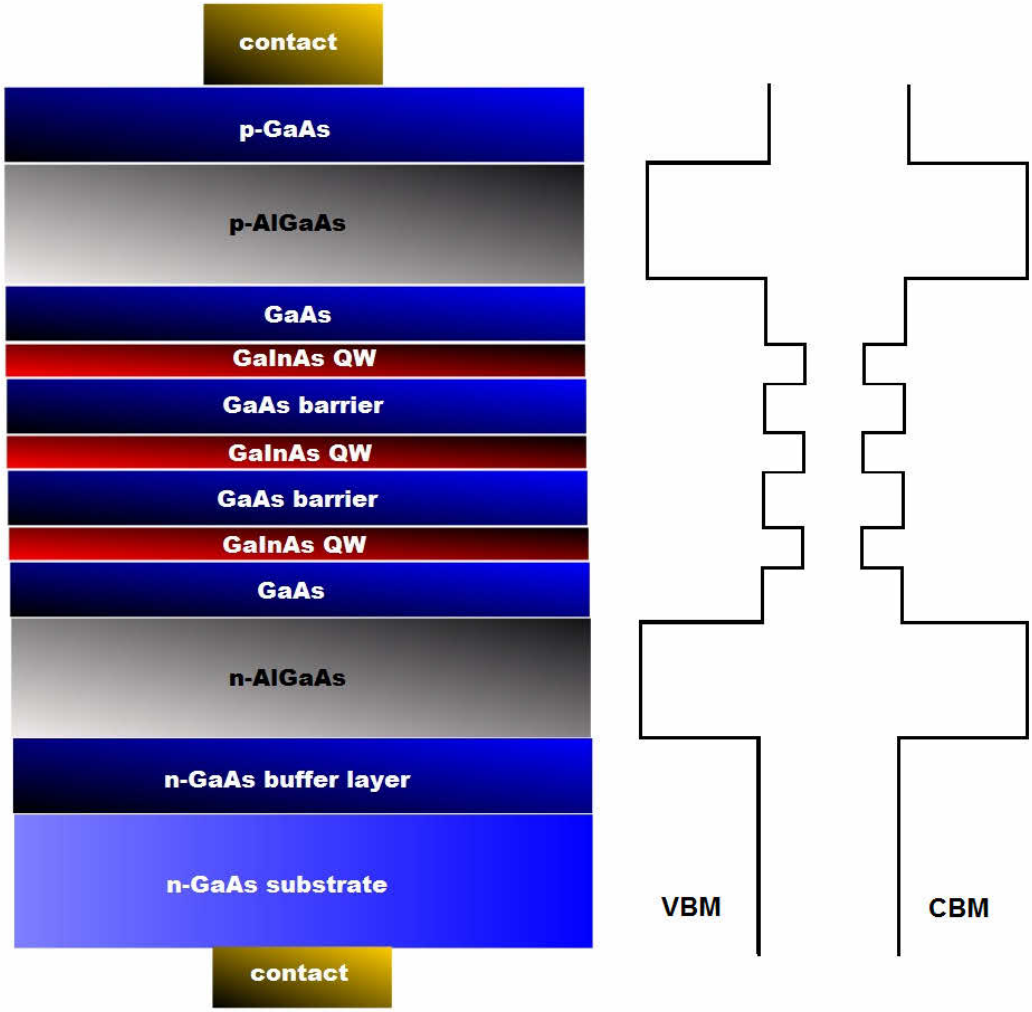

Figure 2. *Schematic film structure of III-V quantum well laser diode and the associated energy band diagram showing relative valence band maximum and conduction band minimum energies for different layers. Electrons and holes are injected into quantum wells by applying a voltage over the pn-junction. Electrons and holes recombine at the quantum well and photons are emitted perpendicular to plane of the figure.*

The lack of good quality interfaces has hampered the development of perhaps the most important application field of modern technology: the logic integrated circuit technology of III-V semiconductors. In Fig. 3, n-channel (i.e., electron channel) metal-oxide-semiconductor field-effect transistor (MOSFET) is

schematically presented. It consists of metal gate contact, source and drain contacts, gate-insulator (oxide) layer and n-doped semiconductor areas as well as p-doped semiconductor substrate. The operation of MOSFET is based on the modulation of the conductivity of the semiconductor channel with an electric field, generated by applying an appropriate gate voltage. Depending on the polarity of the applied voltage and the type of doping of the semiconductor substrate, the depletion of the majority charge carriers or the accumulation and the inversion of the minority carriers may occur. An n-channel MOSFET conducts current when a positive gate voltage generates an inversion layer of electrons near the semiconductor-insulator interface. The electrons are injected and collected by source and drain contacts, respectively, by applying source-drain voltage. N-type implanted regions of the MOSFET provide adequate ohmic "contacts" for the electrons to be injected or collected easily to/from the n-channel. The redeeming feature of the MOSFET's is the energy efficient ability of performing logic operations for which they are widely used in IC-applications. However, the demand for logic transistor operation at high frequencies is high I_{ON} current as well as low I_{OFF} current in the channel.[7] High on-state current is determined by the sheet carrier concentration and the injection velocity of carriers. This is where the III-V compound semiconductors outperform the silicon counterpart by order of magnitude in theory. It has been shown also in practice that the injection velocity in III-V HEMT-structure is more than twice that of silicon at less than half the supply voltage[6] as shown in Fig. 4.

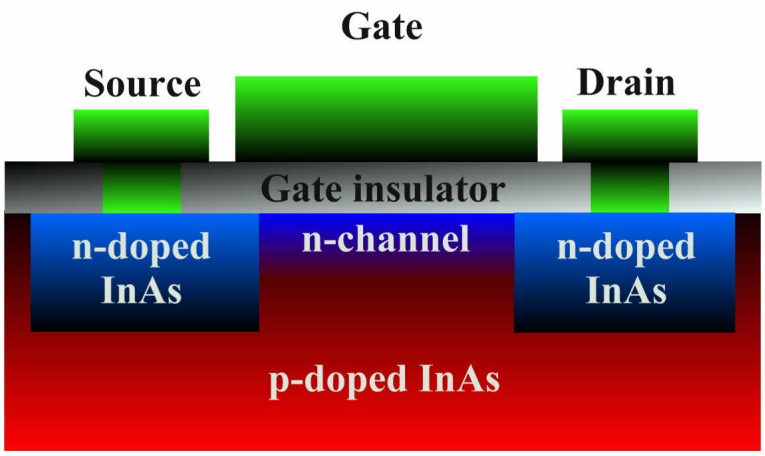

Figure 3. *Schematic presentation of the n-channel Metal Oxide Field Effect Transistor.*

The long-standing problem in utilizing the III-V materials as a part of the MOSFETs is related to the interface between the III-V film and the gate-insulator layer grown on the top of III-V.[7] The quality of the interface is very poor and unfortunately this insulator-semiconductor interface has the most crucial role in the MOSFET operation since the device is conceptually a surface channel device. For reliable and high quality device operation, the insulator-semiconductor interface must be very stable and free of interfacial imperfections and trapped charges. For silicon industry, this problem is solved because the native oxide of silicon (SiO_2) forms miraculously good interface with Si, at least after hydrogen passivation of the interface. Although the resulting SiO_2/Si interface also includes defects (more than 10^{10} cm^{-2} eV^{-1}) it is still low enough for the commercial MOSFET applications.

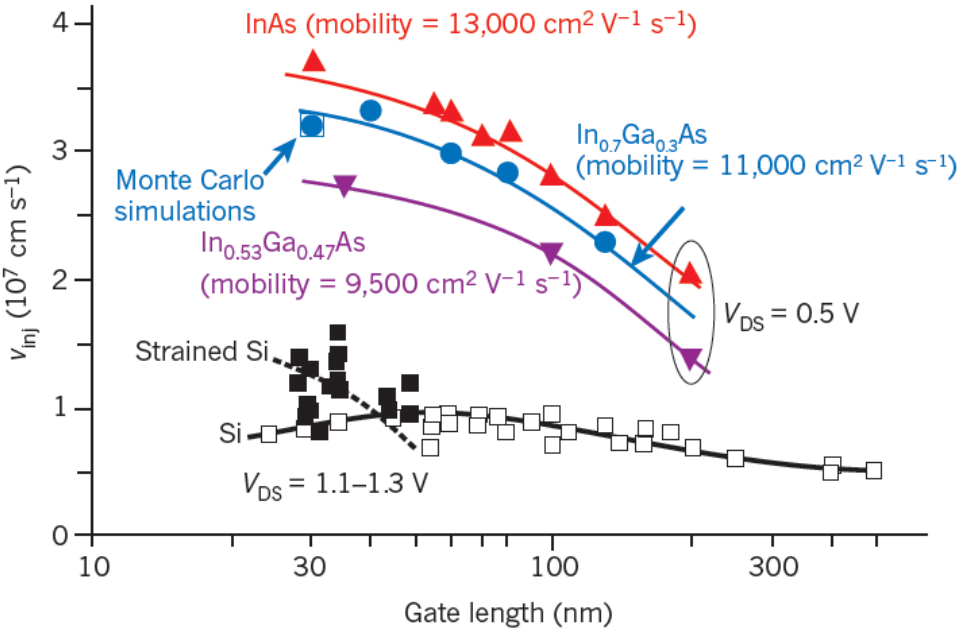

Figure 4. *Measured electron injection velocities for some III-V materials and also for Si for the comparison. The figure is taken from Ref. 6.*

The problem with the insulator/III-Vs arises from the high reactivity of III-V surfaces with oxygen (and oxygen-containing contaminants) which leads to the formation of structurally and electronically poor interface layer between the III-V and the gate-insulator during the manufacturing the insulator film.[2,3,7] In order to understand the low-grade interfaces at atomic level and to find method(s) for avoiding such detrimental defect formation, it is essential to study the III-V surfaces (including adsorbate-covered surfaces) and their atomic structures. The next Chapter covers the general concepts of the III-V compound semiconductor surfaces and how the atoms are arranged (reconstructed) at different conditions for different compounds. The formation of problematic insulator interfaces is concerned more profoundly in Chapter 1.4.

1.2 III-V semiconductor surfaces

Surfaces of the solid materials[12-15] are perhaps the most immediate things we observe in our everyday life, as we live among the solid objects bounded by surfaces. The properties of a solid surface often diverge drastically from bulk solid material. For example, the appearance and characteristics of ordinary iron metal are obviously different from the appearance and characteristics of the iron that has a thin oxide layer on the surface. This iron-oxide, or rust in colloquial language, has very disadvantageous properties for our everyday life and economy as it is generally accepted. Basically, solid surfaces at normal conditions (room temperature and atmospheric pressure) are usually very reactive towards the foreign atoms and molecules of the surrounding environment. Semiconductor materials are no exception and are easily oxidized when cleaved under ambient conditions. These oxidized surfaces are amorphous and far from the ideal systems for physical investigations and characterization and therefore, ultra-high-vacuum (UHV) conditions are required for semiconductor surface studies.

A clean and well-ordered semiconductor surface can be prepared under UHV conditions by cleaving, inert ion bombardment (sputtering) or by MBE techniques. When the clean semiconductor surface is formed, the translation symmetry of the bulk crystal is not conserved and the sp^3 hybrid bonds are broken. Such broken bonds, called dangling bonds, are unsaturated and half-filled by electrons on the ideal semiconductor surface, i.e. the (1×1) bulk-plane. This situation is energetically very unfavorable and the surface will overcome the energy-penalty by minimizing the surface free energy by different mechanisms that are described later in this Chapter.

Considering the thermodynamics, a freshly prepared surface can be considered to be in equilibrium with the constituent atomic reservoirs making the crystal, i.e. the nonstoichiometric surfaces can be examined by allowing the surface to

exchange atoms with the reservoirs,[16] which are characterized by chemical potentials of the elemental system. The stable surface structure has the lowest surface free energy density γ_S:

$$\gamma_S A = E_S - \sum_i \mu_i N_i \tag{1}$$

where A is the surface area, E_S is the total energy of the surface layer, μ_i is the chemical potential of the atomic constituent i and N_i is the number of species i in the system. As the surface is in equilibrium with the bulk constituent reservoir, the upper limit of the chemical potential of species i is determined by the condensed phase of the respective element:

$$\mu_i < \mu_{i(bulk)} \tag{2}$$

On the other hand, in the case of two-atom compound, the sum of the chemical potentials of atomic species i and j must equal the chemical potential of the pair ij making the bulk material at equilibrium conditions:

$$\mu_i + \mu_j = \mu_{ij} = \mu_{i(bulk)} + \mu_{j(bulk)} - \Delta H_f \tag{3}$$

where the ΔH_f is the formation enthalpy of the pair ij. Therefore the boundaries of the chemical potential of species i can be written with inequality:

$$\mu_{i(bulk)} - \Delta H_f < \mu_i < \mu_{i(bulk)} \tag{4}$$

Taking the III-V compound GaAs as an example and exploiting formulae (1)-(4), the surface energy density can be written as:

$$\gamma_S^{GaAs} A = E_S^{GaAs} - \mu_{GaAs} N_{As} - \mu_{Ga}(N_{Ga} - N_{As}) \quad (5)$$

where the surface energy density is a function of μ_{Ga} which varies according to equation (4). The stoichiometry of the surface is determined by $\Delta N = N_{Ga} - N_{As}$ and it defines the surface energy slope as a function of the chemical potential. When the chemical potential is changed, different surface structures can become energetically favorable. For stoichiometric surfaces the surface energy is independent of chemical potential.[15-16] Figure 5 shows an example study of the surface energy for GaAs(100)-Bi surface. This surface phase diagram was obtained computationally by exploiting density functional theory (DFT) and it shows energetically the most favorable Bi-stabilized atomic models for GaAs(100) surface with respect to clean GaAs(100) surface structures at 0 K. As it can be seen, by varying the chemical potential, different atomic structures are stabilized.

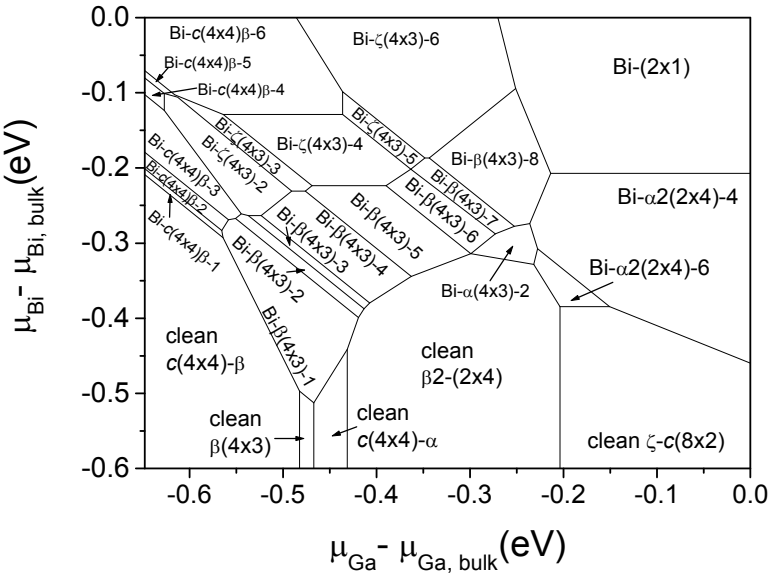

Figure 5. *Calculated phase diagram showing energetically the most stable structures for the Bi-covered GaAs(100) surface in the conceivable chemical potential ranges.*

In general, the experimentally observed surface structure is the one with the lowest free energy that is kinetically accessible under the preparation conditions. This means that there are energy barriers to surface reactions leading to a specific surface structure. For instance, increasing the sample temperature in the experiments should help to overcome the surface energy barriers. However, due to the kinetics, the real surface might have sometimes an atomic structure which total energy is not the lowest one. More general, the observed surface structure corresponds to the local minimum of free energy.

As discussed above, the covalent sp^3 bonds are broken at the surface, leaving dangling bonds with less than two spin paired electrons for each dangling bond. In order to the surface to lower the free energy in this high energy situation, the surface atoms rearrange themselves either by relaxation or surface reconstruction. The latter is described by a drastic change of the translation symmetry of the surface due to formation of new bonds (dimers). In relaxation, the surface atoms are displaced from their bulk position still preserving the symmetry of the lattice. For the III-Vs, the chemical composition of the surface layer may differ from the corresponding bulk composition which results from the charge neutrality requirement of the system. For an autocompensated situation with no space charge, the formation of III-V compound semiconductor surfaces are known to follow the common principles:[15,18,19]

I Minimization of the number of surface dangling bonds

II Tendency for semiconducting electronic structure

The first principle involves the saturation of partially occupied surface dangling bonds via rehybridization or conversion of the dangling bonds into non-bonding orbitals which are completely empty of electrons. This is achieved either by atomic relaxation or surface reconstruction. Both of them usually involve considerable charge transfer from one atomic constituent to another. In the relaxation driven free energy minimization, the surface atom is relaxed towards

the bulk making re-hybridized bond and donating its unpaired dangling bond electron to neighboring atom which in turn can protrude outwards from the bulk. In the surface reconstruction, the neighboring atoms may couple to make new dimer bonds with dangling bond orbitals fully occupied or unoccupied with electrons. Also the symmetry of the surface is usually changed and it is in practice lower than the bulk symmetry.

The second rule emphasizes the tendency for semiconducting energy eigenvalue spectrum of the III-V surface and it is often described by the electron counting model (ECM)[20] for the clean III-V compound semiconductors or generalized ECM (GEC)[21,22] for the adsorbate induced III-V surface structures. ECM is rooted in the equal partitioning of the bonding valence electrons to the nominal bonds in the crystal. The resulting number of electrons per bond in the zincblende III-V semiconductor is two since tetrahedral coordinated group III and group V atom provide nominal 3/4 and 5/4 electrons to each bond. On the surface, there are however partially occupied dangling bonds as it is discussed above. For the III-V compounds, the ECM states that the dangling bonds of electropositive group-III atoms are empty and the dangling bonds of electronegative group-V atoms are fully occupied by electrons for semiconducting atomic structure. This is because the group-III dangling bond energy level locates in the bulk conduction band and the group-V level in the bulk valence band as shown in Fig. 6 for the cases of ZnSe and GaAs.[20,23] The ECM has been successfully applied for predicting and understanding plenty of clean and adsorbate induced low energy III-V surface reconstructions. However, few exceptions have been found where the lowest energy surface does not follow the ECM and shows finite density of states at the Fermi-level.[24,25] In these surfaces, different free energy minimization mechanism, e.g. strain relief, overcome the energy cost of metallicity.

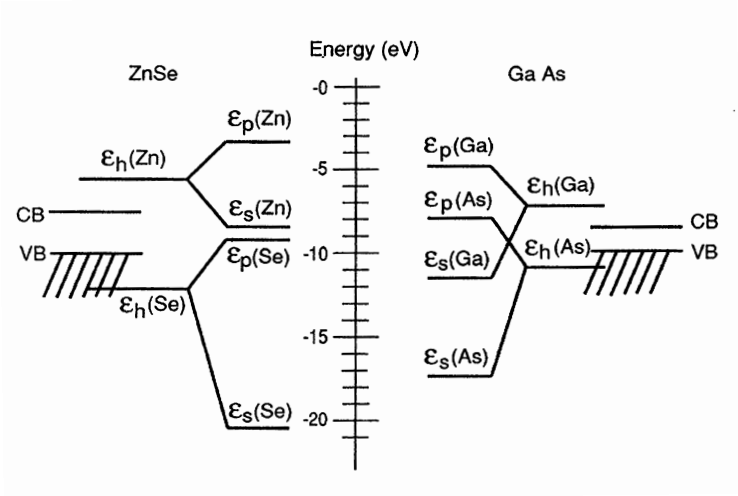

Figure 6. *The energy levels of sp^3 hybridized dangling bond states of ZnSe and GaAs. The figure is taken from Ref. 20.*

For understanding the adsorbate induced surface structures, the GEC heuristics is more applicable.[21,22] As the adsorbate atom can have different valence state and electron affinity compared to host material atoms, the adsorbate can behave as electron bath or sink at the surface. According to GEC, for an arbitrary slab, the number of residual valence electrons remaining for the adsorbate atom on III-V compound semiconductor surface is calculated by:

$$N_R = V_A N_A + 3N_{III} + 5N_V - 2(N_\sigma + N_{ODB}) \quad (6)$$

where V_A and N_A are the numbers of valence electrons and atoms respectively for an adsorbate atom in the crystal, N_{III} and N_V are the numbers of group III and group V atoms respectively, N_σ is the number of sigma (i.e. covalent) bonds and N_{ODB} is the number of occupied dangling bonds. GEC states that the low energy surface structure is the one that minimizes N_R for donor adsorbate atoms and maximizes N_R for acceptor-type adsorbate atoms.

Whether the adsorbate behaves as a donor or acceptor at the surface depends on its relative Pauling electronegativity compared with the host material atoms.

In addition to these surface structure energy minimization mechanisms and guiding principles, the low energy surface structure tends to minimize the electrostatic interactions. The Coulomb interaction between the point charges is characterized by Madelung energy E_M which is minimized for the stable surface structure:

$$E_M = -\frac{1}{2}\sum_{i,j,i\neq j}\frac{q_i \cdot q_j}{\left|\bar{r}_i - \bar{r}_j\right|} \tag{7}$$

The $\bar{r}_i$ in Eq. (7) is the position vector of the point charge i with the charge q_i at the surface.[26,27] The minimization of electrostatic energy partly explains some highly stable surface reconstructions as discussed more profoundly in Chapter 3.3.

The previously described surface free energy minimization principles are helpful for determining and understanding the low energy III-V surface structures. The III-V surfaces have very rich variety of surface structures (reconstructions) depending on the surface preparation conditions. This is especially true for the technologically important low-index III-V(100) surfaces which are also the main field of interest in this work. The surface reconstructions for the materials studied in this work i.e. GaAs(100), InAs(100) and InSb(100), exhibit very similar preparation dependent surface symmetries although the exact atomic structures may differ. A good review about the different atomic structures for different III-V(100) surface reconstructions has been written by Schmidt[28] and therefore all the III-V reconstructions are not covered here. The GaAs(100) surface is undoubtedly the most studied compound semiconductor surface (e.g., Refs. 29-48), and it is known to exhibit a multitude of different reconstructions during the MBE growth for example. Depending on the growth

conditions and/or sample preparation conditions, the symmetry of the surface changes from *c*(4×4) to (2×4) and eventually to (6×6) and *c*(8×2)/(4×2) when the amount of arsenic is decreased, e.g. by decreasing the As partial pressure during the growth or by annealing the substrate and thus desorbing the arsenic under UHV environment. Rather similar trend of surface reconstructions is seen also for InAs(100) and InSb(100), while InP(100) and GaP(100) lack the (4×2) reconstruction and only the (2×4) symmetry is seen in the group III-rich conditions. (These reconstructions are reviewed in detail for example in Refs. 28, 49 and 50). The experiments carried out in this work were mainly done in the group III-rich conditions due to the lack of MBE in the experimental setup and because of the sample cleaning procedure that enhanced the group V element desorption leaving the surface group III-rich. Therefore, it is focused only on the most group V poor reconstruction, which has the *c*(8×2)/(4×2) symmetry. It is noted that the notation used in this thesis for describing the surface symmetries follows the construction of Wood[12-15]. For example, GaAs(100)*c*(8×2) and InSb(100)(1×2)-O.

The atomic structure of the *c*(8×2)/(4×2) reconstruction has remained less clear compared to the *c*(4×4) and (2×4) reconstructions. Earlier, it was assumed that the atomic structure of (4×2) is similar to the famous β(2×4) counterparts seen in the group V rich conditions, with only differing in the atomic composition of the surface layer, i.e. for the β2(4×2) the top surface dimers are composed of group III atoms. Later, Lee *et. al.* suggested rather complex structure called ζ for the Ga-rich GaAs(100)*c*(8×2)/(4×2) reconstruction and it was demonstrated by *ab initio* calculations to be substantially more stable compared to previously suggested β-like (4×2) structures.[51] Most importantly, the ζ model has been found to reproduce all the measurements so far.[51-53] The ζ structure, shown in Fig. 7 includes dimers in the subsurface rather than top layer.

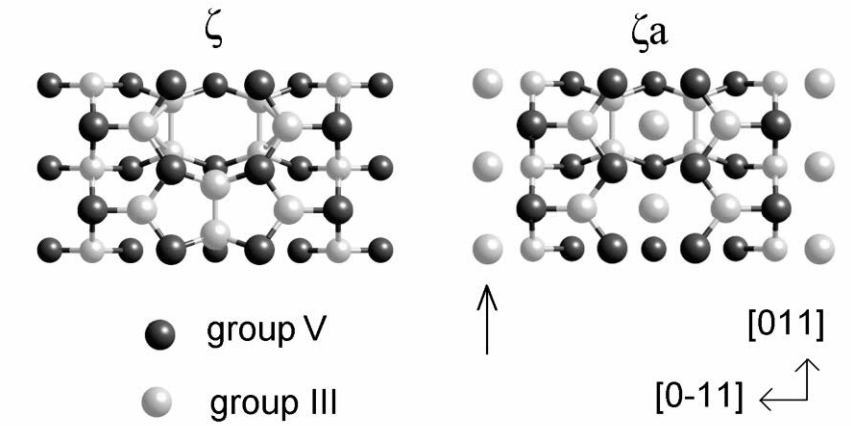

Figure 7. *Two most-likely atomic models, ζ and ζa, which describe the structure of the starting III-V(100)c(8×2) surfaces utilized in this thesis.*

Kumpf *et al.* put forward an atomic structure, which was a generalization of the ζ model for the III-V(100)*c*(8×2) surfaces.[53,54] The generalized model includes two different types of local configurations for the cation atoms. The inherent feature of this model is partial disorder. Miwa *et al.* considered an atomic structure ζa (Fig. 7), which is an ordered variant of the atomic model introduced by Kumpf *et al.* including only those local configurations which were excluded in the original ζ atomic structure.[55] Therefore, the ζ and ζa atomic models include 0% (for ζ) and 100% (for ζa) occupations for the monomer rows marked by an arrow and shown in Fig 7. Additionally, there is a top layer group III dimer in the ζ structure, whereas two non-dimerized group III adatoms in the ζa structure. The partially disordered areas, which were detected by surface X-ray diffraction, may be thought as microscopic mixtures of the ordered ζ and ζa reconstructions. Furthermore, the relative [011]-displacements of the ζ or ζa cells cause the *c*(8×2) periodicity. Surface areas with the pure ζ or ζa structure have been found on III-V(100)*c*(8×2) without significant disorder related to the partial occupancy. According to X-ray diffraction measurements,[53,54] the GaAs(100)*c*(8×2) can be well described with the ζ model, and the InAs(100)*c*(8×2) structure is almost purely of ζa one. Furthermore, the InSb(100)*c*(8×2) is a mixture of the ζ and ζa structures (i.e., is the most

disordered due the partial occupancy). In general, it has been found that the properties of the III-V(100)*c*(8×2) surfaces can be well explained with the ζ and ζa structures.[51-61] However, the stability of ζa has never been demonstrated by *ab initio* calculations on any III-V system.

1.3 Impact of surface structures for III-V devices

As discussed in the previous Chapter, the III-V semiconductor surface (like many semiconductor surfaces in general) often has a modified atomic structure or reconstruction, which is different from the structure of the corresponding plane in the bulk below the surface. These surface reconstructions significantly affect the interfaces produced (grown) on the top of III-V surfaces; usually a different reconstruction on the starting III-V surface leads to a different interface. Therefore, by modifying and processing the III-V surface structures, one can change the properties of the interfaces, which further affect the device operation as described in Chapter 1.1. The purpose of this Chapter is to present three examples of such surface engineering. Two of them concern the molecular-beam-epitaxy of III-V film stacks. The MBE growth procedure,[11] where the material is deposited in the layer-by-layer manner, is essentially a surface process which proceeds via reconstructed III-V growth fronts (i.e. the growing surface is reconstructed during the whole growth). The uncalibrated and poorly controlled MBE growth parameters (e.g. III/V flux ratio and substrate temperature) would rather lead to rough, corrugated and anisotropic atomic structures and low quality reconstructions of the growth fronts than smooth and isotropic surfaces.[11] The structural anisotropy can affect for example to the nucleation of homo/heteroepitaxy causing anisotropic surface diffusion and not unity III/V ratio of the grown crystal.[11,62] This can lead to intermixing of heterostructure interfaces with poor compositional sharpness and morphological roughness with degraded electronic properties. Furthermore, as the modern devices shrink to nanometer dimensions, they become more and

more sensitive to structural quality of the grown surfaces and interfaces. This is especially true for the technologically crucial semiconductor-insulator interface. The third example, which is closely related to the subject of this thesis, addresses to the preparation of oxide / III-V interface, which is particularly important for the research and development of next-generation MOSFET transistors.

1.3.1 Surfactants for epitaxial growth

The quality of the III-V film stacks, grown epitaxially, can be improved by using additional surface species called surfactants on the surface during the growth. By definition, the surfactant can be considered as an entity that lowers the surface free energy and has beneficial properties regarding the crystal quality. In the surfactant mediated growth, the surfactant atoms float at the growth front (but do not incorporate in the crystal) influencing the surface structures occurring during the growth. For example the Stranski-Krastanov type growth mode, which is sometimes highly unwanted, can be substantially suppressed by using appropriate surfactant atoms. This situation is pronounced for example in strained $In_xGa_{1-x}As$ / GaAs(100) heterostructures, which are commonly used in HEMT, microwave devices and near infrared lasers. Due to the lattice mismatch, the In-content and/or the thickness of the alloy is restricted to relatively low values as the high In-concentration leads to the formation of 3D islands which are harmful from the device point of view. It means that the energy cost of the strained heteroepitaxial InGaAs layer exceeds the energy cost related to dislocation formation at some specific InGaAs thickness. As a result, the InGaAs layer relaxes into its own lattice constant and high density of defects (e.g dislocations) are formed. It has been shown however, that with the usage of tellurium or bismuth as a surfactant in the $In_xGa_{1-x}As$-GaAs(100) growth, thicker and flatter structures can be obtained. The Bi surfactant has been reported to smoothen the III-V film and improve the luminescence for

example.[63-67] Furthermore, the critical thickness of InAs wetting layer on InAs/GaAs heterostructure, which is even more strained structure than the $In_xGa_{1-x}As$-GaAs, is only 2 MLs.[68,69] However, by using indium atoms as virtual surfactants, by growing the InAs under In-rich conditions (usually the growth is performed in the As-rich conditions), the critical thickness can be substantially increased, and the resulted interface reveals superior quality and notably improved photoluminescence (PL) intensity.[68-70] It is noted that the threshold current in laser diodes is often inversely proportional to the PL intensity. When the normal InAs(100) growth mode is changed from As-rich to more In-rich, the surface structure changes from usual (2×4) to *c*(8×2)/(4×2) reconstruction. It can be therefore anticipated that this specific surface reconstruction and the atomic structure behind it has profound implications for the formation of good quality InAs/GaAs heterostructure. The atomic structure of technologically useful In terminated III-As(100) surfaces is covered in Paper 3 and Chapter 3.3.

Aforementioned bismuth is also promising surfactant for growing dilute nitrides.[71-73] Dilute nitride materials have been aggressively investigated for multijunction high efficiency III-V solar-cell applications. By introducing nitrogen into the GaAs/InGaAs lattice, the band gap can be tuned to cover a wide spectral band of the solar radiation from near infrared to far infrared region. The lattice-matched GaInP/GaAs/InGaAsN/Ge heterostructures are expected to reach efficiencies around 50 % under 500-sun illumination (by using light concentrators) for example. However, the nitrogen incorporation rapidly degrades the structural and electronic properties of InGaAsN if the mole fraction of N is increased. It has been shown that the nitrogen incorporation to the GaAs lattice can be enhanced by using bismuth as surfactant. At the moment, it is still unclear which Bi-induced reconstruction(s) are helpful in the surfactant growth. Interestingly, M. Masnadi-Shirazi *et al.* have recently[74] demonstrated that a Bi-induced (2×1) reconstruction, which is not normally seen during the III-V epitaxy, is a very useful growth front for $GaAs_{1-x}Bi_x$. The atomic structure behind the (2×1) surface reconstruction is peculiar low energy surface structure as it does not obey the electron counting rule and is therefore

metallic.[20,24,75] In fact, it was previously proposed[75] that the (2×1)-Bi metallic surface structures could have beneficial properties for surface diffusion rates and step-attachment kinetics during crystal growth. Furthermore, the (2×1) reconstruction is atomically smoother than the (2×4) reconstruction for example. As it was seen previously in Fig. 5, the unusual Bi-stabilized (2×1) reconstruction occurs only in the Ga-rich conditions for GaAs(100).

1.3.2 Growth of heteroepitaxial interface

The ideal III-V heterostructure should be compositionally sharp across the heterojunctions. This means that little or no intermixing between the different film materials is preferred. Although the bulk structure and electronic properties may be of good quality (e.g. due to utilizing surfactant mediated growth), the low-grade interface can deteriorate the device by evoking electronic defect states which can act as recombination centers for electrons and holes, as mentioned earlier. Even the bonding environment of the atoms at the interface of different layers can impact to the quality of the device. By tuning the surface structure during the growth of the crucial III-V heterointerface, the device characteristics can be substantially improved. For example, by adding a small amount of indium (about 1 ML), which causes an In-stabilized *c*(8×2)-reconstructed (100) surface on the heteroepitaxial III-V growth front (e.g., InP/InGaAs and InAs/GaSb), has been found to substantially improve the properties of these interfaces for electronics devices.[76-79] Figure 8 shows PL-results from the study of Anan *et al.*[76] They observed even 100-fold improvement in the PL intensity for III-P/III-As heterostructure when about 1 ML of In was deposited before the P_2 exposure and III-P layer growth [thus producing In-induced *c*(8×2)/(4×2) structure on the III-As surface as deduced by reflection high energy electron diffraction (RHEED)]. At the In-stabilized InGaAs(100) surface, the number of Ga-P bonds can be suppressed for the subsequent InP film fabrication.[76] The bonds between gallium and phosphorous

were found to be the main sources for the poor electronic quality of the interface and thus the poor PL-intensity. This research of Anan *et al*.[76] is one of the earliest works of the surface engineering.

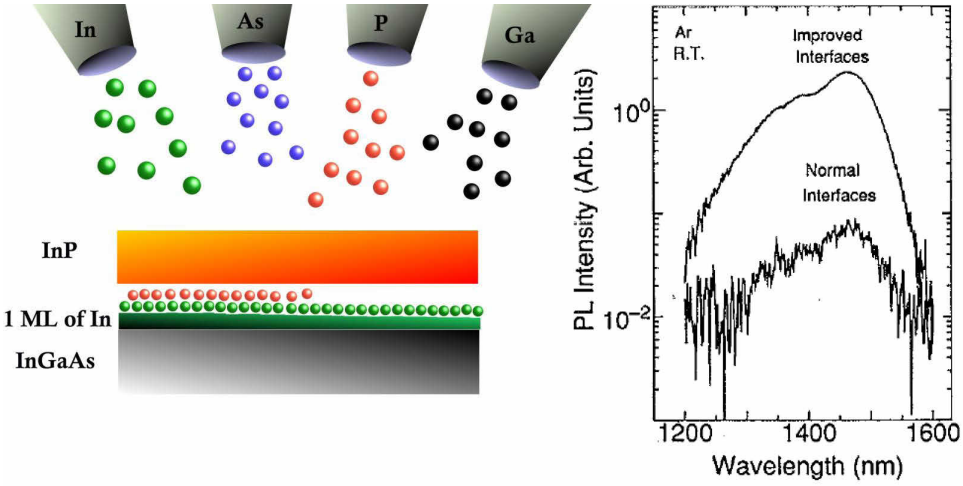

Figure 8. *Left: Scheme of the surface engineering experiment of Anan et al.*[76] *Right: PL intensity change due to the engineering of III-V surface during the growth (the right figure is taken from Ref. 76.).*

1.3.3 Formation of insulator interfaces

III-V devices based on heteroepitaxy (e.g. lasers and solar cells) usually have their active regions buried under the topmost barrier layer(s). However, at some point the device material must “meet the outside world”, in terms of laser chip’s exterior surfaces for example. As the bare III-V surfaces are easily oxidized uncontrollably, the III-V components are usually protected (passivated) by controllably fabricated insulator layers which prevent the air oxidation and contamination of the device. Besides structural protection, the insulation layers can have multiple functions depending on the type of application. For example insulating anti-reflection (AR) coatings are highly important for the operation of

high efficiency solar cells, as they guarantee that the most of the radiation preserves in the semiconductor material and is transferred into electricity. Furthermore, for the logic transistor applications, the insulator layer is as important as the semiconductor material itself because the insulator makes it possible to control the conductivity of the semiconductor channel by modulating the electric field through the gate-insulator. For transistors, the insulator/semiconductor interface quality is highly important because the "active region" of MOSFET (i.e., the channel) is just below the interface. Therefore the understanding of the properties of these insulator interfaces is of strong interest for researchers worldwide and also for this work.

Insulators used in the semiconductor industry are usually metal oxides which have the desired properties (e.g., large band gap and relative permittivity) for the given application.[7,80] The state-of-the-art silicon MOSFET transistors nowadays have high-κ HfO_2 dielectric as a gate-oxide material.[81] High-κ means that the permittivity of the insulator material is higher than that of the traditional SiO_2 (κ=3.9) gate dielectric. The usage of a high-κ insulator is motivated by the aggressive transistor scaling.[80,81] As the channel length of the MOSFET decreases, the constant field scaling requires that the oxide thickness should also decrease. Thus, the gate oxide thickness in Intel's 65 nm process was only 1.2 nm, for instance.[80] This thickness is so small that the quantum mechanical tunneling produces considerable amount of leakage current. The usage of high-κ material allows one to use physically thicker oxides, suppressing the tunneling effect, with the same electrical properties as with using the thin SiO_2 gate insulators (i.e. the equivalent oxide thickness remains the same). The high permittivity insulators are also needed for the long sought III-V MOSFETs. Even though the introduction of new gate-oxide material that replaced SiO_2 in Si-transistors was not a trivial task at all, the fabrication of a good quality insulator-III-V interface has proven to be even a harder task.

The major problem with the III-V-insulator interfaces has been the pinning of the Fermi-level (FL) at the interface which has hindered the III-V FET

development.[7,82-89] The MOSFET operation is based on the modulation of the surface FL position, around the band gap, by the gate voltage as mentioned above. In many studies, it has been found that such movement of the Fermi-level is limited and the Fermi-level is pinned (locked) to some specific energy point at the III-V surface. That is, the position of the Fermi-level on the III-V side of the interface does not change as a function of the gate-metal work function, but pins to some energy position (e.g., in the middle of the band gap) of the host semiconductor. It is noted that the FL-pinning also takes place at the metal-semiconductor interface.[86] The comprehensive understanding of the physical mechanisms behind this harmful FL-pinning phenomenon has not been achieved so far.

In general, the pinning has been associated to interface states generated at the III-V insulator interface.[7,82,83,90-103] Bardeen first suggested that the surface states at the metal-semiconductor interface become charged and uncharged depending on the metal work function[90] and this idea was put forward to metal-insulator-semiconductor (MIS) interface by Cowley and Sze.[91] When these surface/interface states become occupied by electrons for instance (i.e. charged), the formed dipole screens the original electric field preventing the free movement of the Fermi-level. Furthermore, Heine proposed that the evanescent tails of the metal wave function can act as states in the semiconductor band gap that pin the Fermi-level.[92] This model, known as the metal-induced-gap-states (MIGS) can be regarded as an intrinsic property of the system. Extrinsic pinning mechanisms have also been proposed. So called unified defect model (UDM) states that the semiconductor processing induces defects, namely atomic vacancies, antisites etc., at the surface.[93-95] Such defects can generate highly localized states/bands with a peaked density of states distribution in the band gap of the semiconductor. On the other hand, Hasegawa and Ohno proposed that the interface states are due to bond disorder at the semiconductor-insulator interface and the associated model is called disorder induced gap states (DIGS).[96] Disorder reduces the separation between the bonding and antibonding sp^3 states and produces DIGS continuum

in the band gap. The density of state distribution of such continuum is U-shaped with its minimum at so-called charge-neutrality-level (CNL) E_{CNL} of the semiconductor-insulator interface. It is defined as the energy where the density of state continuum in the band gap changes from a donor type to acceptor type with increasing energy and the Fermi-level tends to pin near the E_{CNL} according to Hasegawa *et al.*.[96, 82,83] Figure 9 clarifies this situation.

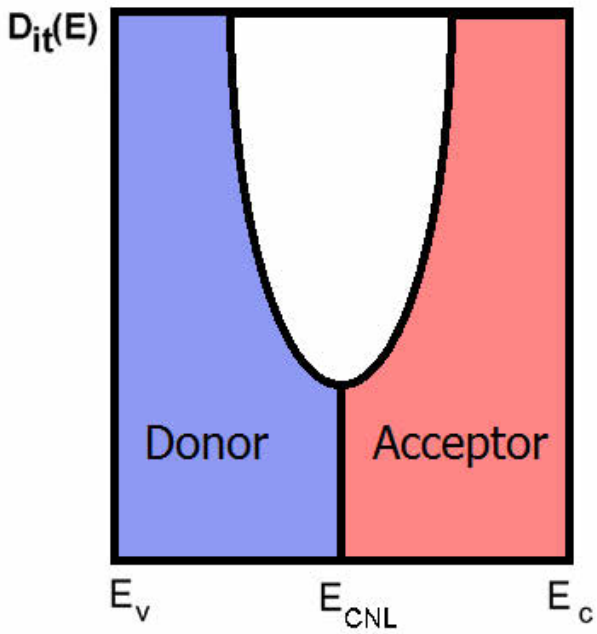

Figure 9. *Interface state density distribution according to disorder induced gap states model.*

The surface/interface state density distributions of the III-V-insulator interfaces are usually measured by capacitance-voltage (CV) method, conductance method, scanning tunneling spectroscopy (STS) or photoluminescence technique. According to numerous studies, the observed shape of the distribution is usually U-shaped supporting the picture of the DIGS model as can be seen from Fig. 10 for GaAs metal-insulator systems.[104] Although some

studies also indicate discrete energy peaks as predicted by UDM and most likely, the real situation is more or less a combination of the both above mentioned models.[93-95,105] From the technological and basic research perspective it is important to understand which kind of defects and bonding configurations, formed during the preparation of the insulator/III-V interface, produce extrinsic gap states at the III-V insulator interface. Because it is clear that at least the reaction between the III-V surface and oxygen causes defects, much work has been done to elucidate what kind of oxidation-induced defects are formed.

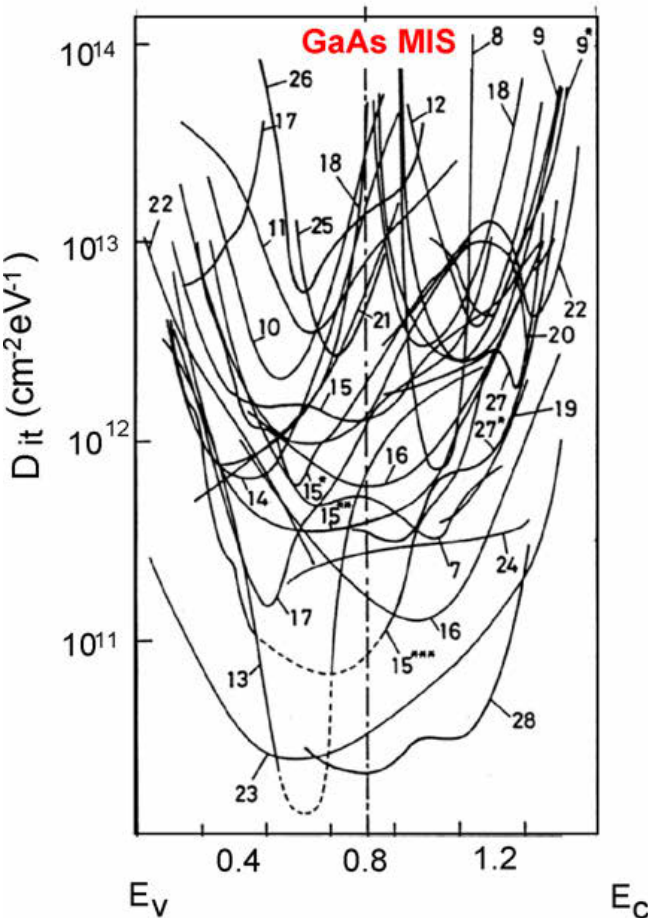

Figure 10. *Measured interface state densities for GaAs MIS structures. The figure is taken from Ref. 104.*

Defects are always formed at the surfaces and interfaces (even oxide free) and their concentration depends on their formation energies. Walukiewicz has studied the formation energies of various charged defects, e.g. As/Ga vacancies or antisites, on GaAs. The stability of these intrinsic native defects depends on the position of the Fermi-level. Thus, Ga antisites for instance are more likely to occur for n-type GaAs rather than p-type GaAs.[106-108] At the oxidized III-V surfaces, these defects are also likely to occur. However, the deviation of bonding at the disordered insulator-semiconductor interface, as implemented in the DIGS model,[104] produces also states at the band gap. The disordered or amorphous interface/surface is rather hard to characterize both experimentally and computationally and therefore, the detailed structure of the defects has been under scientific debate for many years. Obvious candidates include III-O and V-O bonds and the unsaturated group III and V dangling bonds and dimer bonds. According to Robertson,[101,102] Ga dangling bonds produce the density distribution of the interface states which tails down from the inside of the conduction band to the bulk band gap. The situation is analogous to As antibonding state distribution. Furthermore, the formation energy of Ga dangling bond decreases when the position of the Fermi-level falls close to the valence band maximum.[101,106-108] Therefore, for n-type MOS capacitor/FET with p-type substrate, the Fermi-level is pinned as the high density of Ga dangling bond or As antibonding states are produced within the band gap due to their low formation energy. The results of this thesis elucidate the defect issues and especially the role of the group III dangling bond.

To improve the problematic insulator-III-V interfaces, various techniques have been proposed. The common target has been the development of suitable surface passivation techniques in order to suppress the FL-pinning and enhance the structural and electronic properties of these interfaces by protecting the III-V surface channel from the direct oxidation. These approaches include for example the use of silicon interface control layer,[109-114] sulfur or sulphide treatment prior to gate insulator deposition,[115-120] MBE grown $(Gd_{1-x}Ga_x)_2O_3/Ga_2O_3$ layer[121-128] and the deposition of high-κ dielectric by atomic

layer deposition (ALD) technique.[129-145] Also, indium containing binary/ternary III-V materials have shown encouraging device characteristics and reduced FL-pinning.[146-148] Even though these methods have given promising results and relatively low interface state density values and improved the device characteristics, they are still behind the defect densities of Si interfaces used in the commercial MOSFETs. While the minimum of the interface state continuum may yield low values in the middle of the band gap, the interface state density still exponentially increases towards the band edges as shown in Fig. 10. Later in this thesis it is shown that the extrinsic defect state formation can be substantially reduced at least at the semiconductor-oxide surface/interface by producing crystalline oxide structures on III-V surfaces. These surfaces lack of disorder as they are highly ordered and they are electronically good quality as well as chemically stable.

2 Methods

As mentioned in the Introduction, one of the key-issues in the state-of-the-art nano-scale III-V device development is the atomic-scale understanding of the phenomena taking place at the interfaces and surfaces. In general, it is not straightforward to obtain such knowledge from any system, and in particular, from not so well defined amorphous interfaces. For the latter, the interpretation of the results may be very controversial. The combination of various complementary surface/interface-sensitive measurements and calculations are required in order to obtain a well-justified determination of the atomic and electronic structures. This was also set as a target in the research of this thesis. The rapid development of computational resources and algorithms have made possible to perform state-of-the-art theoretical calculations and simulations for solid surfaces and interfaces. In addition to experiments, *ab initio* density functional theory calculations were also implemented in this work. From the

fruitful combination of experiments and calculations, many physical properties of the III-V compound semiconductor surfaces can be elucidated. This Chapter gives a brief overview from the different experimental and computational methods used through the making of this research.

2.1 Experimental methods

The experimental methods implemented in this work cover relatively wide portion of surface sensitive experimental measurement techniques, which were already available in the University of Turku system. In addition, a big portion of the experiments were carried out at the synchrotron radiation facility. Also, the interface studies were performed through collaboration by exploiting interface sensitive measurement techniques.

2.1.1 Experimental setup

The majority of the experiments made in this work were carried out in the University of Turku utilizing the surface science system shown in Fig. 11. This ultra-high-vacuum multi-chamber consists of commercial analysis chamber, made by Omicron, and separate sample preparation chamber. These chambers were interconnected allowing the sample transfer without breaking of the vacuum. The analysis chamber was equipped with scanning tunneling microscope (STM), low energy electron diffraction (LEED) and X-ray photoelectron spectroscopy (XPS) facilities. XPS was equipped with dual anode (Al and Mg) X-ray source and hemispherical electron analyzer. The preparation chamber included various evaporators for adsorbate deposition as well as leak valves for gas exposures in the vacuum chamber. In addition, quartz-crystal microbalance (QCM) facilities were installed in the preparation chamber for the flux estimation of different evaporants. The dielectric depositions were done

using electron-beam evaporator (e-beam) and home-made ALD, installed into the preparation chamber allowing the sample transfer without breaking the vacuum. The analysis and preparation chambers included turbomolecular-, ion- and titanium sublimation pumps for high vacuum generation. Rotary vane pumps were used for fore-vacuum generation. The base pressure in the analysis chamber was usually below 1×10^{-10} mbar and in the preparation chamber below 1×10^{-9} mbar.

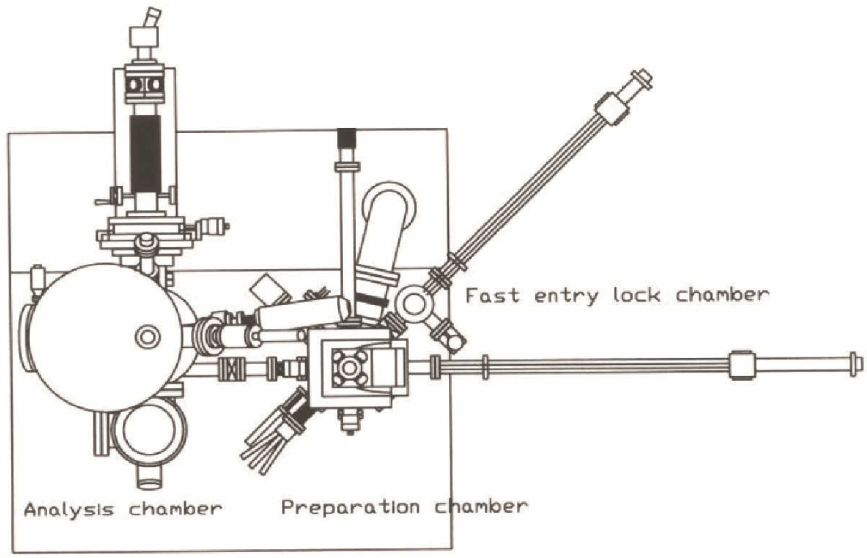

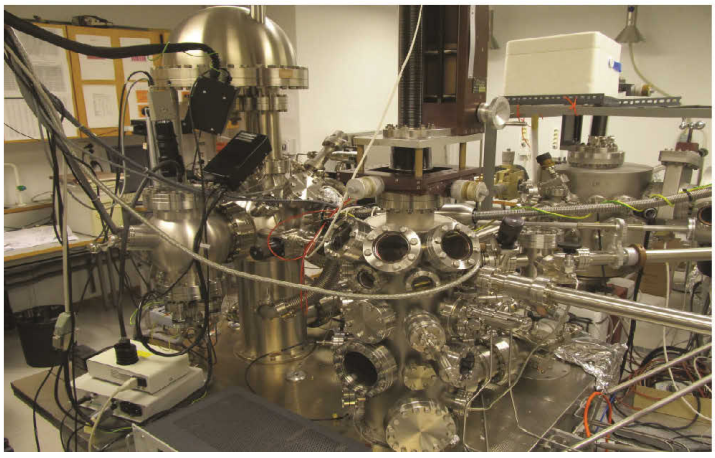

Figure 11. *University of Turku measurement setup.*

The synchrotron radiation photoemission (SRPES) experiments were carried out at the MAX-lab synchrotron-radiation research center, Lund University, Sweden.[149] Two different storage rings and beamlines were used for the experiments in this thesis: The MAX-I storage ring, which had the capability of operation energies of 550 MeV and the MAX-II storage ring, with operation energies of 1500 MeV. Beamline-41 (BL-41) of MAX-I storage ring had one end-station dedicated to angle-resolve-photoelectron-spectroscopy (ARPES) measurement. The synchrotron radiation was produced by the bending magnets of the MAX-I storage ring and the obtainable photon energy range of the radiation was about 17-170 eV. The analysis chamber of BL-41 served also as the sample preparation chamber. In addition, MBE chamber was connected to the BL-41 end-station which allowed the fabrication of good quality III-V surfaces for the PES studies. The analysis chamber of the BL-41 was equipped with Ar-sputtering facilities for sample cleaning and LEED. Beamline I311 of MAX-II storage ring was an undulator beamline, dedicated to high resolution XPS and X-ray absorption spectroscopy with the photon energies of 43-1500 eV. The end-station consists of separate sample preparation chamber with sputtering gun and LEED optics and analysis chamber with hemispherical electron energy analyzer (SCIENTA SES200) which was used for the PES measurements. The photon flux on the sample was 10^{11}-10^{13} photons/s and the overall energy resolution achieved in this end-station was E/dE = 5×10^{3}-2×10^{4}.

2.1.2 Low energy electron diffraction

Diffraction based experimental techniques, especially X-ray diffraction, have been the cornerstones for understanding the atomic structures of crystals. However, as being a bulk sensitive method, the traditional X-ray diffraction is not suitable for surface studies. Perhaps the most widely established diffraction technique applicable to surfaces is low energy electron diffraction. The

diffraction of electrons was first discovered by Davidson and Germer in 1927. LEED exploits the wave particle duality and the wave character of electrons.[12, 150-154] According to de Broglie relation, the wavelength λ of an arbitrary particle can be expressed as:

$$\lambda = \frac{h}{\sqrt{2mE}} \tag{8}$$

where *h* is the Planck constant, *m* is the mass of the particle and *E* is the kinetic energy. The energies of the electrons used in traditional LEED experiments ranges from 10-500 eV and the corresponding electron wave lengths are 0.55 Å to 3.89 Å. These values are in order of subatomic bond lengths and therefore, the electrons can experience diffraction.[150,152,154] Traditional LEED apparatus, schematically shown in Fig. 12, consists of an electron gun and a fluorescent screen for the backscattered electron detection.[153] In the LEED experiment, the low energy electron beam, generated at the electron gun filament (e.g. LaB), is accelerated to desired energy and focused on the sample. As the electrons interact very strongly in solid material due to strong electron-electron interactions and phonon and plasmon excitations, the mean free path of the propagating electron wave is short. According to so called “universal curve”,[12] which is shown in Fig. 13, the mean free path of the electrons typically used in LEED experiments, corresponds to the curve minimum. Thus, the LEED is a highly surface sensitive technique.

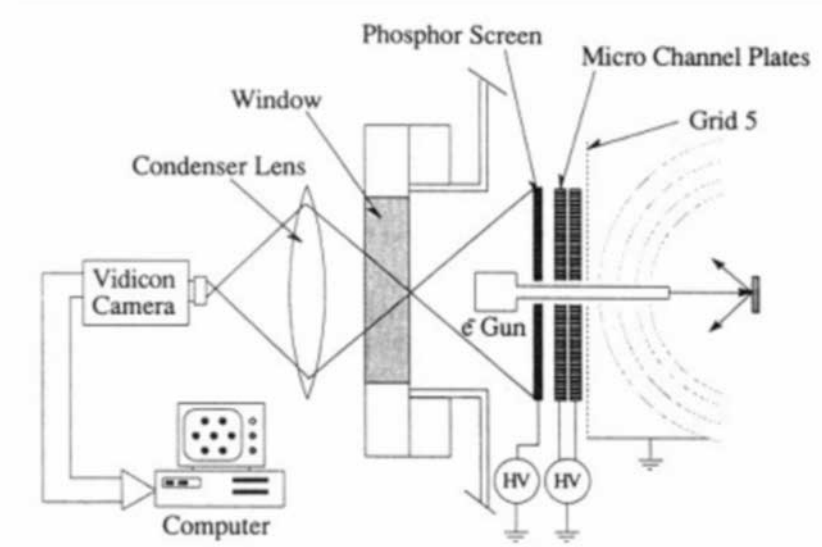

Figure 12. *Schematic illustration of LEED apparatus. The figure is taken from Ref. 153.*

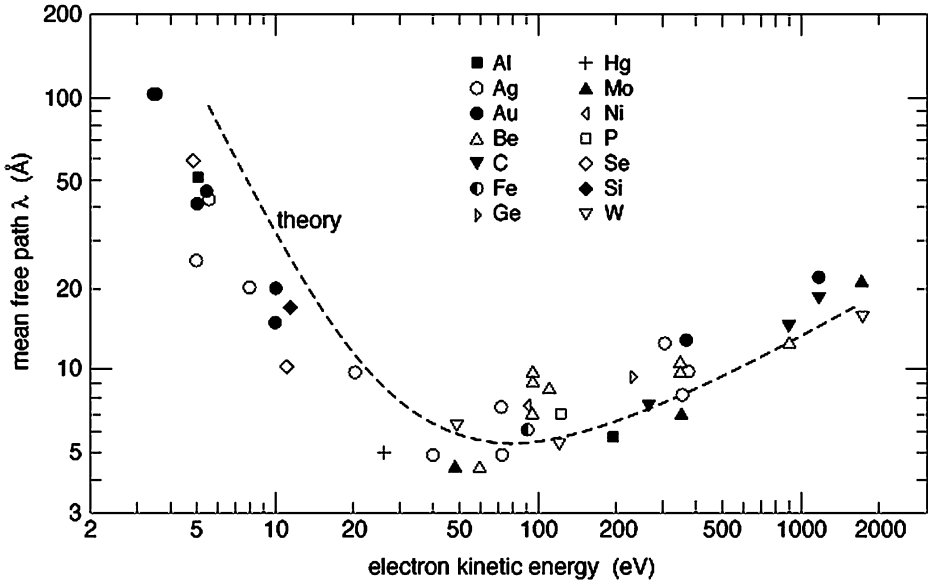

Figure 13. *The universal curve showing electron mean free paths in solid as a function of the electron kinetic energy. The figure is taken from Ref. 12.*

LEED can be described with two-dimensional Laue's diffraction conditions: the constructive interference of outgoing waves scattered from the Bravais periodic lattice occurs when the planar component difference between scattered ($\mathbf{k}_s$) and incoming ($\mathbf{k}_i$) wave vectors is one of the surface reciprocal lattice vectors **K** in the Fourier-space.[12,150,151] More generally, the linear momentum parallel to the surface is conserved in diffraction. The electrons can be considered as plane waves and the diffraction with the initial wave vector $\mathbf{k}_i$ from two-dimensional Bravais is described by relation:

$$\mathbf{k}_{s\|} = \mathbf{k}_i + \mathbf{K} = h\mathbf{b}_1 + k\mathbf{b}_2 \tag{9}$$

where the vector $\mathbf{k}_{s\|}$ is the planar component of the wave vector of the diffracted plane wave, vector $\mathbf{K}$ is the reciprocal lattice vector, vectors $\mathbf{b}_j$ are the primitive translation vectors of the reciprocal lattice and *h* and *k* are integers (Miller indices). The primitive translation vectors of the reciprocal lattice holds the orthogonality relation for the real space lattice translation vectors $\mathbf{a}_i$:

$$\mathbf{a}_i \cdot \mathbf{b}_j = 2\pi\delta_{ij} \tag{10}$$

where δ_{ij} is the delta-function. As there is no translation symmetry perpendicular to the surface, there is no relation between the corresponding components of initial and scattered wave vectors $\mathbf{k}_i$ and $\mathbf{k}_s$ respectively. However, as the elastic scattering of the plane waves is assumed, the magnitudes of these wave vectors must be equal:

$$\left|\mathbf{k}_i\right| = \left|\mathbf{k}_s\right| \tag{11}$$

The set of solutions for the equations (9) and (11) can be graphically constructed by using Ewald sphere concept shown in Fig 14.[12] In this construction, the Ewald sphere radius is determined by the magnitudes of $\mathbf{k}_i$ and $\mathbf{k}_s$. The point where the reciprocal lattice vector $\mathbf{K}$ intersects with the rods determined by the reciprocal lattice points, defines the diffraction maxima. The diffraction pattern determined by the LEED experiment therefore describes the reciprocal lattice of the surface. By changing the magnitude of the incident wave vector, i.e. by changing the electron energy, the radius of the Ewald sphere changes.

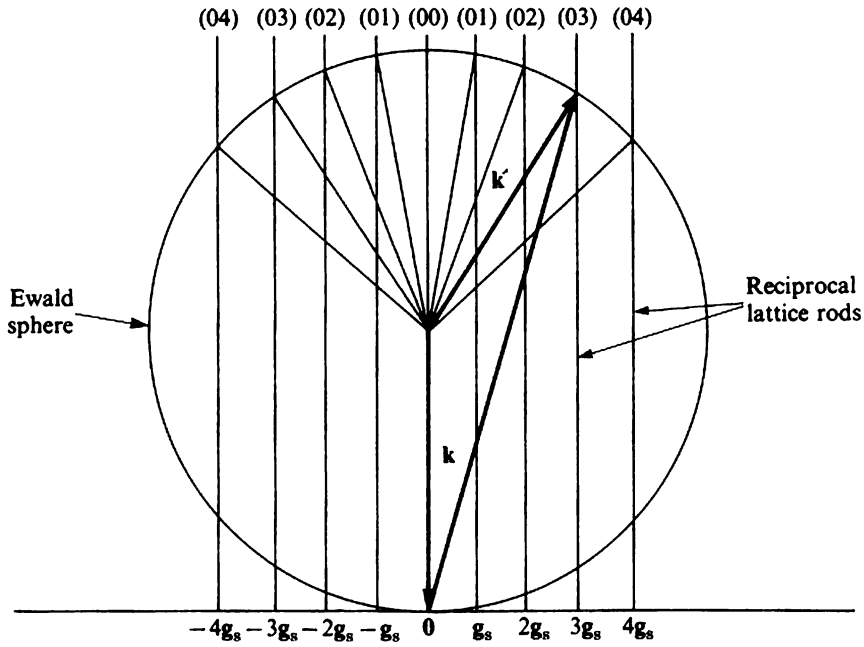

Figure 14. *Ewald sphere construction of Low Energy Electron Diffraction. The figure is taken from Ref. 12.*

LEED is a very powerful technique for determining the surface lattice in relation to the bulk-plane lattice. An example of a LEED pattern, which is obtained from clean InAs(100) substrate, is shown in Fig. 15. The InAs(100) bulk-plane lattice cell is known to be square. Usually, the most intensive spots observed in the LEED pattern are also contributed by the bulk-like planes below the surface because the minimum mean free path for electrons is about 5 Å (i.e. about 15 Å / 2 signal depth), as discussed above. It means that the (1×1) spots are often the most intense ones. In Fig. 15, the length of the square (1×1) cell can be easily determined by analyzing the distance of the bright spots along the [011] direction. The white square marks the (1×1) cell in Fig. 15. There are also clear additional spots between the (1×1) spots, which correspond to lower symmetry of the reciprocal lattice of the reconstructed surface layer. In this case, the additional spots from the surface indicate that the reconstructed surface has (4×2) symmetry.

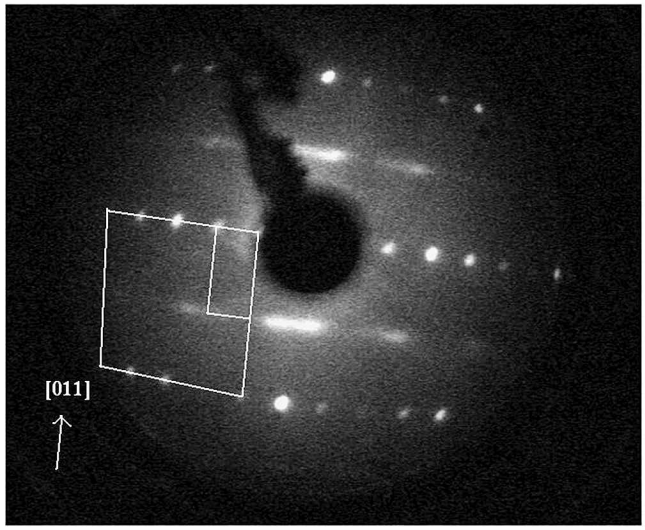

Figure 15. *Measured LEED image from clean InAs(100)c(8×2)/(4×2) reconstruction. White square indicates the bulk (1×1) unit-cell and white rectangle illustrates the surface unit cell with (4×2) symmetry relative to bulk.*

The sharpness and the intensity of the observed LEED spots can be linked to the quality of the prepared surface. However, LEED only gives area-averaged information from the surface; the local environment, e.g. surface defects and local disorder, are hard to detect purely by the LEED pattern.[150-154] Some information about such defects can be however obtained by studying the intensity profiles of the spots. In addition, the diffraction of the electrons is not from the ideal two dimensional arrays of atoms as the electrons have certain penetration depth to solid. This, in addition to the large cross-section of electron-atom collisions prevalent at typical LEED energies (which also makes the LEED so surface sensitive), raises the probability of electrons to experience multiple scatterings. Multiple scatterings occur within the individual atoms and between the atoms and crystal surfaces. In addition, some electrons can be inelastically scattered. The description of such mechanisms is very complicated and therefore the information of atomic positions for instance is very difficult to be acquired from the measurements (compared with X-ray and neutron diffraction techniques). However, by using dynamic LEED theory and theoretical calculations, it is possible to simulate LEED *I/V* spectra; i.e. the LEED spot intensity as a function of electron energy. The measured *I/V* spectra accompanied by the calculated ones (for the set of different atomic structures) can be used for the atomic structure determination.

To recapitulate, the surface unit cell as well as some information about the surface quality can be rather easily obtained from the LEED experiment. Obviously other measurements and analyses are needed for more accurate surface structure analysis. Within the framework of this thesis, LEED was mainly used for a quick surface structure and quality measurements and no comprehensive *I/V* analyses were performed.

2.1.3 Scanning tunneling microscopy

One of the major breakthroughs of the surface- and nanoscience took place by the invention of scanning tunneling microscope in the early 1980s by Gerd Binnig and Heinrich Rohrer.[155,156] They were later awarded a Nobel price of physics due to their significant invention. STM is rooted in the quantum mechanical tunneling effect that has been theoretically predicted over 80 years ago, but was experimentally confirmed in 1957 by Esaki by the observation of anomaly in the current-voltage behavior in thin germanium p-n-junctions.[157]

If we consider a finite potential barrier and a particle propagating against it, the classical interpretation tells that the particle can overcome the barrier only if its kinetic energy is greater than the height of the barrier. However, according to quantum mechanics, the particle has a non-zero probability density inside and other side of the barrier, even though the kinetic energy is lower than the height of the barrier. Thus, the particle may experience a quantum mechanical tunneling through the potential barriers. The inherent reason behind this classically non-intuitive result lies in the wave-particle duality and Heisenberg uncertainty relation of quantum mechanics.

STM takes an advantage of the tunneling phenomenon of electrons for real-space surface analysis.[155,156,158] In the bulk solid state material, the electron wave functions are more or less periodic but at the surface this periodicity is not preserved and the wave function tails exponentially into the surrounding medium (e.g. vacuum). In the STM experiment, a finely sharpened metal tip is brought close to the sample surface. When the distance between the sample and the tip is sufficiently small (about 1 nm or less), the tails of electron wave functions of the sample and the tip will overlap. When the bias is applied between the sample and the tip, the electron tunneling will occur. According to Bardeen,[159] the resultant tunneling current can be described with the first order time dependent perturbation theory:

$$I = \frac{2\pi e}{\hbar}\sum_{\mu,v}\left\{f(E_\mu)[1-f(E_v+eU)]-f(E_v+eU)[1-f(E_\mu)]\right\}\cdot\left|M_{\mu v}\right|^2\delta(E_v-E_\mu) \quad (12)$$

where the $f(E)$ is the Fermi function, $M_{\mu v}$ is the electron wave function dependent tunneling matrix, E_μ and E_v are the energies of the unperturbed electronic states $\psi_{\mu\upsilon}$ of the sample and the tip in the absence of tunneling (usually around the Fermi-energy) and U is the applied voltage between the sample and tip.[158, 160] The matrix element can be described by the following equation:

$$M_{\mu v} = -\frac{\hbar}{2m}\int d\bar{\mathbf{S}}\cdot\left(\psi_\mu^*\nabla\psi_v - \psi_\mu\nabla\psi_v^*\right) \quad (13)$$

The nature of the wave functions $\psi_{\mu v}$ in equation (13) depends on the atomic structure of the sample and the tip. By approximating the STM tip geometry as spherical and the tip wave functions as s-type in character, the equation (12) reduces to the following approximation:[160]

$$I \propto U\cdot n_t(E_F)\cdot e^{2\chi R}\cdot\sum_v\left|\psi_v(r_0)\right|^2\delta(E_v-E_F) \quad (14)$$

where the $\chi = \frac{2m\phi}{\hbar}$ depends on the work function ϕ, R is the effective radius of the spherically symmetric STM tip and $n_t(E_F)$ is the density of states at the Fermi-level for the tip. As the electron wave functions decay exponentially into the vacuum, the tunneling current is exponentially proportional to the distance between the sample and the tip. Thus, a small change in this separation can yield large changes in the tunneling current, making the STM highly surface sensitive measurement technique.

STM can be utilized in several ways for surface analysis.[158] Using a feedback loop circuit to keep the tunneling current constant by varying the tip's height with respect to the sample and simultaneously scanning the sample in the x-y direction, the resulting recorded height changes of the tip reflects the variation of the local density of surface electronic states (LDOS) at atomic resolution. This is so called constant-current-imaging (CCI) technique of the STM which is illustrated in Fig. 16a. The polarity of the applied voltage determines whether the tunneling current is from the filled states of the sample to the empty states of the tip or *vice versa*. At highly ordered and well-defined surfaces, the LDOS contour map obtained with CCI reflects the atomic arrangement of the surface (i.e. the atomic structure of the surface). For example, the STM image shown in Fig. 16b, is obtained by the CCI imaging of Sn-adsorbate covered InAs(100) surface. The image dimensions are 60 nm $\times$ 60 nm. This figure reveals the presence of at least two different surface reconstructions on the surface. Large-scale STM images (e.g., 1 μm x 1 μm) are very useful to evaluate the quality and the amount of surface defects at the surfaces, the latter of which is difficult to be concluded by LEED measurements. Significant information about the atomic structure can be also obtained. An example of such high-resolution image is shown in Fig. 17, where the formation of bismuth nanolines at InAs(100) is demonstrated.[161]

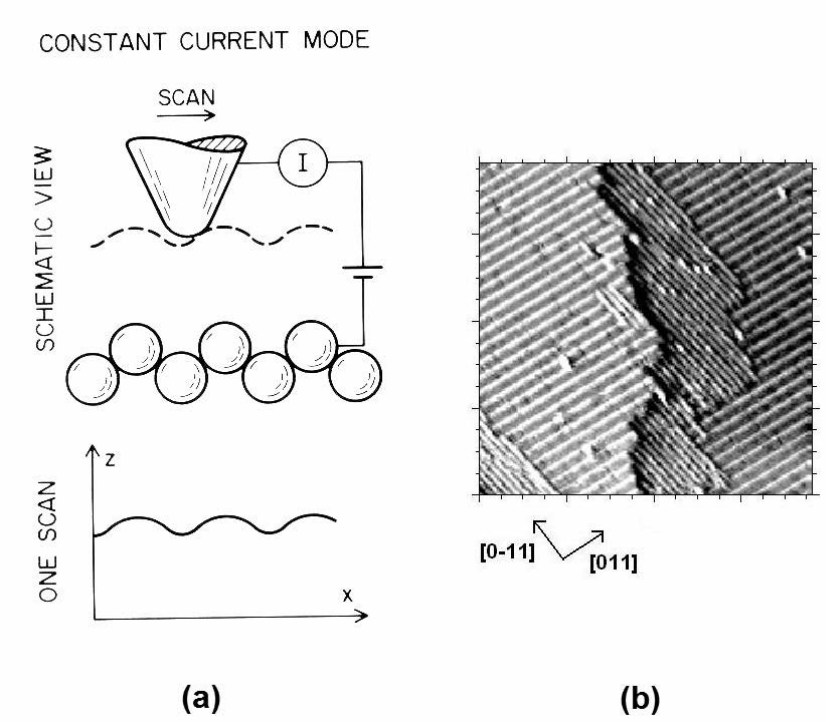

Figure 16. *(a) Schematic illustration of constant-current-imaging technique of STM. The figure is taken from Ref. 158. (b) Measured filled state (2.885 V) STM image from Sn-covered InAs(100) surface.*

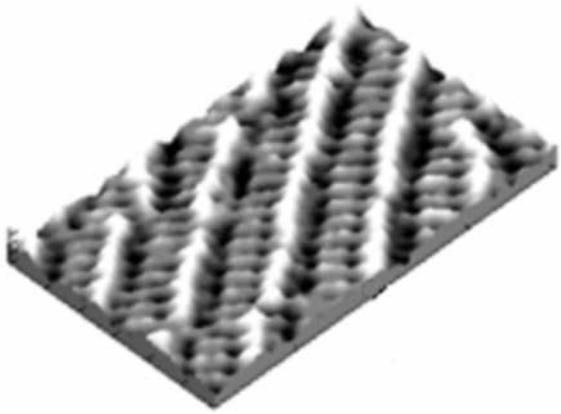

Figure 17. *High-resolution STM image from Bi-induced nanoline structure on InAs(100) surface.*

The quantitative analysis and the interpretation of CCI-STM images are not straightforward since many features contribute to the obtained image. First, the geometry of the tip apex is unknown in real situations and the tip induced effects are difficult to be taken into account.[158] High quality STM tips are fabricated by etching and ion milling procedure and the tip's radius of curvatures of approximately 10 nm can be obtained but the tip geometry beyond that is unknown. Furthermore, the electronic feedback loop is not infinitely fast and therefore the movement of the tip does not necessarily correspond to the situation where the tunneling current is constant. Eventually, the STM is not a chemically sensitive measurement and measures only the LDOS which does not necessarily correspond to exact atomic positions. Therefore, complementary methods are helpful for the atomic structure determination.

Apart from the traditional topographic imaging, STM can be utilized for scanning tunneling spectroscopy measurements.[158] According to equation (14), the dependence of the LDOS on the applied voltage can be extracted by measuring the *I/V* curves, i.e. the bias dependency of the tunneling current. By approximating the tunneling matrix $M_{\mu\nu}$ as constant in the Bardeen equation (13), the equation reduces within the low temperature limit to:

$$I \propto \int_0^{eU} n_t(E_F - eU + \varepsilon) n_s(E_F + \varepsilon) d\varepsilon \tag{15}$$

where the tunneling current is a convolution of density of states at the surface (n_s) and the tip (n_t). Assuming the constant LDOS at the tip, the first derivative of equation (15) gives information about the LDOS of the surface near the Fermi-level:

$$\frac{dI}{dU} \propto n_s(E_F - eU) \tag{16}$$

STS can be powerfully utilized for studying surface electronic structures and modern STM instruments can record topographic and spectroscopy information simultaneously. Taking the technologically crucial oxide-III-V surface as an example, the STS measurement provides valuable information about the initial defect formation and the associated defect state formation. Figure 18 shows an example of the STS curve, measured from an oxidized InSb(100)(1×2)-O reconstruction. The figure shows a semiconducting electronic structure with no defect state density within the band gap. In the STS experiments, it is crucial to test how the topographic parameters like voltage and set-point tunneling current affect the I-V curves and the extracted DOS curves. It is also helpful to measure a known reference sample with the same parameters.

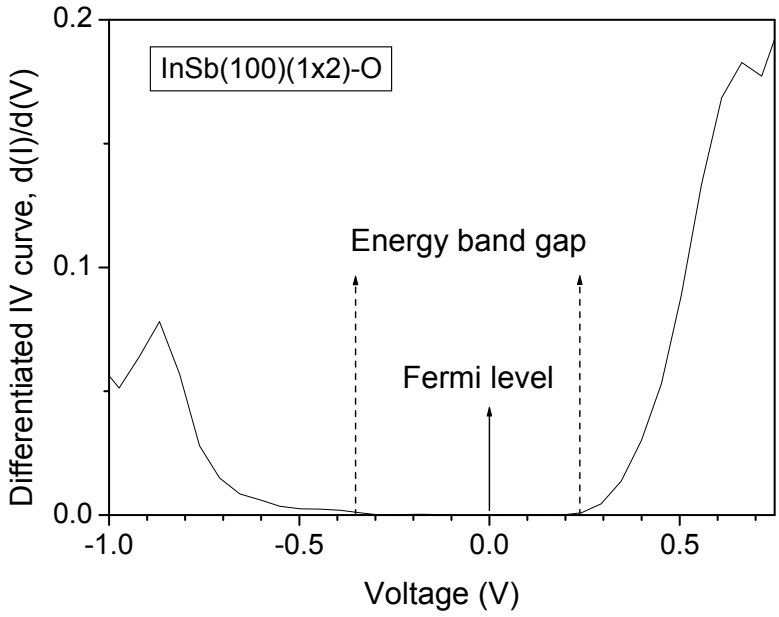

Figure 18. *Scanning tunneling spectroscopy image from an oxidized InSb(100) surface.*

2.1.4 Photoelectron spectroscopy

The photoelectric effect was first discovered by Heinrich Hertz[162] in 1887 and later explained by Albert Einstein.[163] According to Einstein, when a solid material is illuminated by electromagnetic radiation, the excited electrons gain kinetic energies proportional to the frequency of the incident light rather than the intensity. This can be explained by the assumption that the light is composed of discrete quanta. This was highly controversial suggestion at that time as the general idea was that the light was composed of continuous waves. According to Einstein, the kinetic energy E_K obtained by a photoelectron in a single photoemission process can be written as:

$$E_K = h\nu - E_B - \Phi \tag{17}$$

where the h is the Planck constant, ν is the frequency of the photon, E_B is the binding energy of an electron and Φ is the work function.[164] Equation (17) reveals that by measuring the kinetic energy of the photoelectrons, the initial binding energy of the electron can be determined. The photoelectric effect is a basis for photoelectron spectroscopy and can be utilized for various different measurements. As the kinetic energy is proportional to binding energy of an electron, which in turn is proportional to the atomistic orbital energies, characteristic for the different elements in the periodic table, the photoelectron spectroscopy is a chemically sensitive measurement. Furthermore, the bonding (atomic) environment of an atom influences the valence charge distribution (i.e. electronic potential) and eventually to the core state energy.[165] Thus, the photoelectron spectroscopy gives information about the chemical environment of different atoms at the surfaces for example.[164,166] As discussed in Chapter 2.1.2, the mean free path of electrons propagating in a solid is very limited. Therefore, the PES measurement is surface sensitive even though the incident

radiation (e.g. X-ray) can easily penetrate the whole sample under investigation.

In general, the photoemission process in a solid-state material is very complicated process to be comprehensively described. This is because the solid material is essentially a multi-body system which is involved as a whole in the photoemission. The widely used quantum mechanical description of photoemission relies on Fermi's golden rule and perturbation theory. Namely, the ground state of solid can be described by Hamiltonian H_0 and the photo-ionization can be treated by time-dependent perturbation method where the incident photon beam is described by a small perturbation H'. The perturbed Hamiltonian is characterized by momentum operator $\mathbf{P}$ and vector potential $\mathbf{A}$ with the plane wave representation of the radiation:

$$H' = \frac{e}{2mc}(\mathbf{AP} + \mathbf{PA}) \tag{18}$$

$$\mathbf{A}(r,t) = \mathbf{A}_0\left(e^{i(\mathbf{k}\cdot\mathbf{r})-\omega t} + e^{-i(\mathbf{k}\cdot r)-\omega t}\right) \tag{19}$$

The transition probability per unit time between the initial and final eigenstates is given by the Fermi's golden rule:

$$T_{i\to f} = \frac{2\pi}{\hbar}\left|\left\langle \psi_f \middle| H' \middle| \psi_i \right\rangle\right|^2 \delta(E_f - E_i - h\omega) \tag{20}$$

where E_f and E_i are the final and initial state energies respectively. According to Berglund and Spicer,[167,168] the photoemission process in solids can be divided into three steps: i) the excitation of photoelectron, ii) electron transport to the surface, and iii) electron escape through the surface into vacuum. By

taking a deeper insight into these steps, the excitation process follows the Fermi's golden rule (20) and the excitation occurs from the initial occupied Bloch state into the final unoccupied Bloch state. Because the photon carries a negligible amount of momentum [at the ultra-violet photoemission (UPS) regime, for example], these states need to have the same reduced Bloch wave vector, i.e. the inter-band transition is direct. Second, the photoelectron needs to propagate to surface. The exited photoelectrons travelling in solid, experience very strong electron-electron interactions as described earlier. This causes the electrons to experience a multitude of scatterings and the initial number of photoelectrons is therefore reduced. After the photo-excited electron has reached the surface, the perpendicular component of momentum (or kinetic energy) has to be greater than the energy barrier generated by a surface potential (known as the work-function), in order the photoelectrons to enter into the vacuum for subsequent detection. The electron lacking of sufficient energy is reflected back to the bulk crystal. Due to the breakage of periodic potential of the crystal at the surface, the momentum component perpendicular to the surface is not conserved for the ejected photoelectrons. However, the momentum component parallel to the surface is conserved. There exists a strict relation between the parallel component of crystal momentum and the measured electron kinetic energy and measurement angle. This enables the experimental band structure determination by employing angle-resolved photoemission spectroscopy (ARPES). In this work, ARPES was only used for core-level-spectroscopy and no band-structure characterization was done. The reader is directed to the vast literature available for the ARPES technique for the band-structure determination of solids (e.g. Refs. 166, 169-174 and the Refs. therein).

The aforementioned three-state model for photoemission assumes an infinitely fast transition between the initial and final eigenstates. However, in a real situation, when the atom is ionized into the final excited state in the photoemission process, it is left with a core-hole which has a finite lifetime

τ .[170,171,175] Due to Heisenberg's uncertainty relation, the finite lifetime of the core-hole imposes an uncertainty on the measured photoelectron energy and therefore the measured spectra always include an intrinsic line width. The resulted energy distribution is similar to Cauchy distribution and can be viewed by Lorentzian distribution function. Furthermore, the experimental instrumentation and conditions, including the energy resolution of the analyzer, incident photon energy broadening and the sample temperature, produce a broadening to the measured spectra which can be viewed by Gaussian distribution. The overall spectral line shape is therefore a convolution of Lorentzian and Gaussian functions, i.e. the Voigt function.[164,176] In addition, the inelastic scattering induces a background intensity signal in measured spectra and photoelectrons lose some of their kinetic energy. In this thesis, the fitting procedure of the measured spectra included Shirley[177] background removal and the deconvolution of the measured peaks was performed by imposing Voigt functions.

At the surface, the number of the nearest neighbors, i.e. the coordination number of atoms may differ, relative to bulk. Thus, the chemical environment of surface atoms is different compared to bulk, which is a result of modified valence charge distribution of the surface atoms.[165] The valence charge distribution affects also the core-electron binding energy because the valence charge screens the electrostatic potential generated by the positive nuclei. In a multi-electron system, the binding energy ε of a core electron is defined as an energy difference between the final ionized state with (N-1) electrons and the ground state energy with N electrons:[179,180]

$$\varepsilon = E(N-1) - E(N) \tag{21}$$

Thus, the core-electron binding energies for bulk and surface atoms are:

$$\varepsilon_B = E_B(N-1) - E(N) \tag{22}$$

$$\varepsilon_S = E_S(N-1) - E(N) \tag{23}$$

The binding energy difference between the bulk and surface core-electrons is therefore the energy difference between the respective final states:

$$\Delta\varepsilon = E_S(N-1) - E_B(N-1) \tag{24}$$

The energy differences between the final states of surface and core electrons are called surface-core-level shifts (SCLS)[165,179] and they appear in the measured spectra as extra components. Therefore, at the well-prepared crystalline surface, the SCLS reflects the different bonding environment of the surface atoms, and thus the different atomic sites. The identification of bulk and surface components in the measurements can be achieved by changing the photon energy or by changing the emission angle. By changing the photon energy, the kinetic energies of the photoelectrons are also changed and the electron mean free path in solid is thus different, as it was seen in Fig. 13. Figure 19 shows an example of measured As3d photoemission spectra from GaAs(100)(1×2)-Sn surface with different photoelectron emission angles. The spectra are fitted using two spin-orbit split components with the Voigt line-profile. The most intense component in Fig. 19 represents the bulk-emission and the less intense component arises from the surface As atom. In this surface, the arsenic has at least one bonding environment different from the bulk zincblende structure.

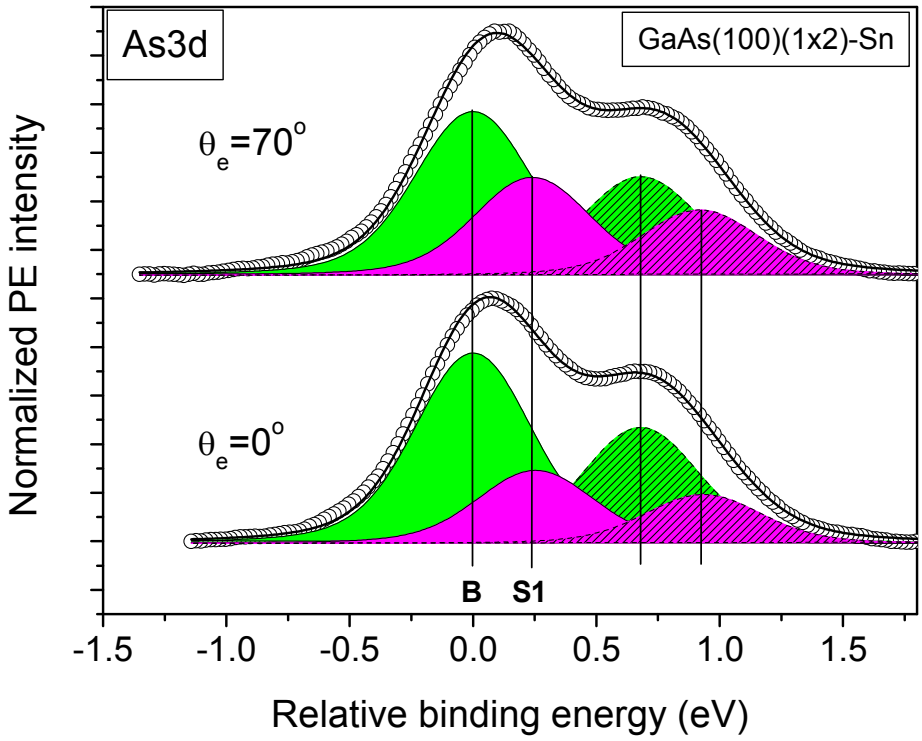

Figure 19. *Measured (open circles) and deconvoluted (lines) SRPES spectra from GaAs(100)(1×2)-Sn surface taken at two different emission angles. Bulk component (B) is shown as green peak while surface related component (S1) is shown as violet peak. The intensity of surface-related component S1 increases as a function of the photoelectron emission angle.*

The photoelectron spectroscopy naturally requires a source of photons. Traditional choices include Al and Mg anode X-ray tubes, where the electrons are accelerated towards the anode and characteristic X-ray emission occurs. Al and Mg Kα characteristic peaks have sufficient energies and intrinsic line widths for the PES studies. Furthermore, a helium UV-discharge lamp can be used for UPS studies. These facilities were also available and utilized in the University of Turku system during this research. However, traditional X-ray tubes are not sufficient for high-resolution core-level spectroscopy, when detailed core-level shifts should be determined. Superior light-source compared

to any other method for generating X-rays and/or UV light is synchrotron.[166,169,173,174] The synchrotron takes an advantage of the electromagnetic radiation emitted by charged particles experiencing acceleration. Traditionally, when a charged particle, e.g. an electron, experiences acceleration it emits dipole radiation, with radiation pattern shaped as a toroid. However, when the electron is relativistic, i.e. the velocity of the electron is close to the speed of light, the radiation pattern of the emitted electromagnetic radiation is drastically different in the observer's (e.g. post-graduate student) frame of reference. According to relativistic electrodynamics, the electron frame of reference and the observer's frame of reference are connected via Lorentz transformation and the original toroidal shape of the radiation pattern is changed to a narrow radiation-cone in the laboratory frame of reference as is schematically illustrated in Fig. 20. This intense radiation generated by the relativistic charged particles under acceleration is called synchrotron radiation. Traditional synchrotron usually includes linear particle accelerator, where e.g. electrons are accelerated to relativistic velocity and a storage ring where the relativistic electrons circulate. The acceleration and the synchrotron radiation generation is achieved by bending magnets, wigglers and/or undulators.

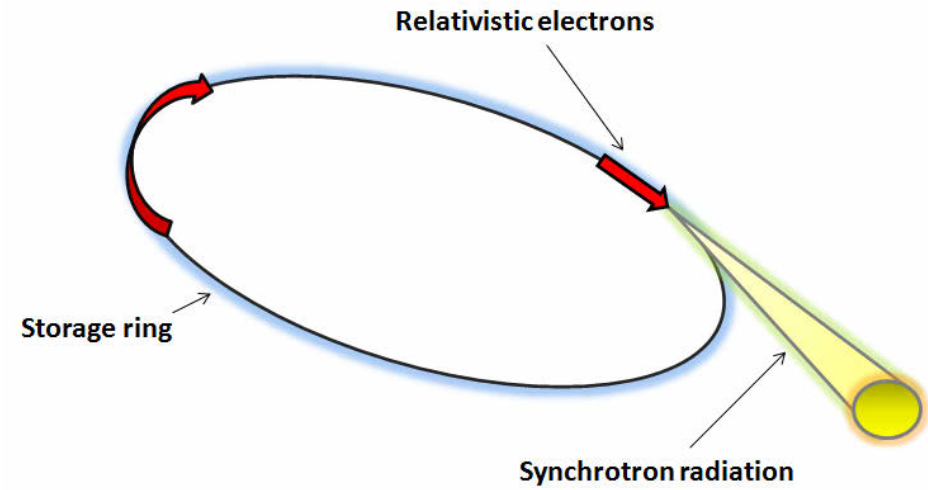

Figure 20. *Schematic illustration of synchrotron light-source*

The superior properties of the synchrotron light-source include: wide spectral range from VUV to hard X-rays, tunable photon energy and even 10^{10} times higher photon flux compared with traditional laboratory sources.[166] Furthermore, the synchrotron radiation is emitted to a very narrow solid angle and it is linearly polarized with respect to the plane of the trajectory and elliptically polarized elsewhere. Due to the high photon-flux, the amount of emitted photoelectrons is large and in turn, the measurement time is short.

2.1.5 Other methods

The experimental methods described in the earlier Chapters are dedicated to the surface characterization. In order to study the crucial device (e.g. semiconductor-semiconductor and semiconductor-insulator) interfaces, other methods are needed. This Chapter gives a brief introduction to two widely used semiconductor interface characterization techniques: the photoluminescence spectroscopy and the capacitance-voltage profiling. These methods were employed in this work, through collaboration, for the semiconductor-insulator interface characterization.

The photoluminescence is a non-destructive technique for investigating the properties of bulk semiconductors and their interfaces, e.g, the density of impurities, by utilizing a luminescence process.[154, 181] In the photoluminescence process, the studied system is first excited by photons from its low energy state (ground state) to some excited high energy state, which is subsequently decayed by emitting a photon. The energy and the intensity of the emitted photons are recorded.

The photoluminescence can be described by a three-step process in a defect-free semiconductor sample:[154,181]

I *Absorption* of photon with energy $\hbar\upsilon$ and the generation of electron-hole pair

II *Relaxation* of newly generated electron and hole towards the CBM and VBM

III *Radiative recombination* of the electron-hole pair and the emission of a photon with energy of $\hbar\upsilon'$

Because the time-scale of the relaxation process is orders of magnitudes faster compared with the radiative recombination process, the associated electron-hole recombination occurs from the CB and VB extremas, even though the energy of the exited photon is greater than the energy band gap of the material. However, in a real situation, the bulk semiconductor material, interface and/or surface contain defects and the associated energy levels which usually reside inside the semiconductor band gap. These extra levels give rise to additional PL-signals, making this technique very powerful tool for studying the crystal and interface qualities. Namely, the recorded peak intensity and emission energy reflects the variety and concentration of energy states present in the semiconductor material.[181]

Another important and widely used interface characterization method is CV-profiling.[10,182] The CV-measurements are especially powerful for the characterization of the important MOS-structures. Figure 21 shows a cross-section of a simple MOS capacitor, which consists of a semiconductor crystal, a metal-oxide insulator layer and metal contacts. As described in Chapter 1.1, depending on the polarity of the applied voltage between the metal contacts and the doping type of the semiconductor material, accumulation or depletion of the majority/minority charge carriers may occur. For a p-type semiconductor for example, a negative bias results in an exponential increase in the number of majority charge carriers (holes) at the semiconductor insulator interface (i.e., accumulation). The total capacitance of the MOSCAP in this situation is just the capacitance of the insulator. When the bias is changed to positive, holes are

depleted from the interface and the depletion layer is formed. The depletion layer makes an extra capacitance component and the total capacitance is thus reduced (because now there are two capacitors in series). Furthermore, at the large positive bias voltage, an inversion layer of electrons is produced at the surface and the total capacitance approaches to the oxide capacitance.[10,182] Traditionally, the CV measurements are performed by applying a DC bias across the metal contacts, and the measurements are made with AC-signal. The previously described situation corresponds to low-frequency (<1 kHz) CV measurements. At high-frequency the minority charge carriers cannot respond to the imposed ac-signal and the capacitance remains at the depletion capacitance value. Figure 22 shows an ideal low- and high-frequency as well as deep-depletion CV-curves from ideal MOS-capacitor.

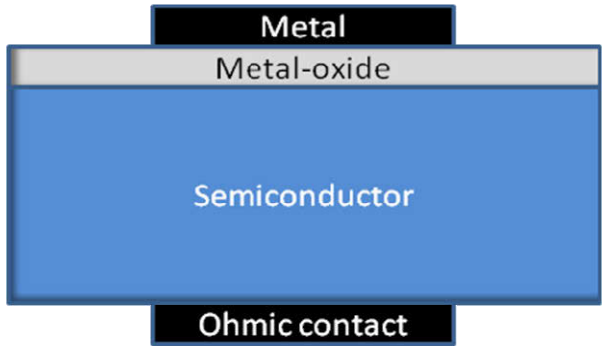

Figure 21. *Cross-section of MOS-capacitor.*

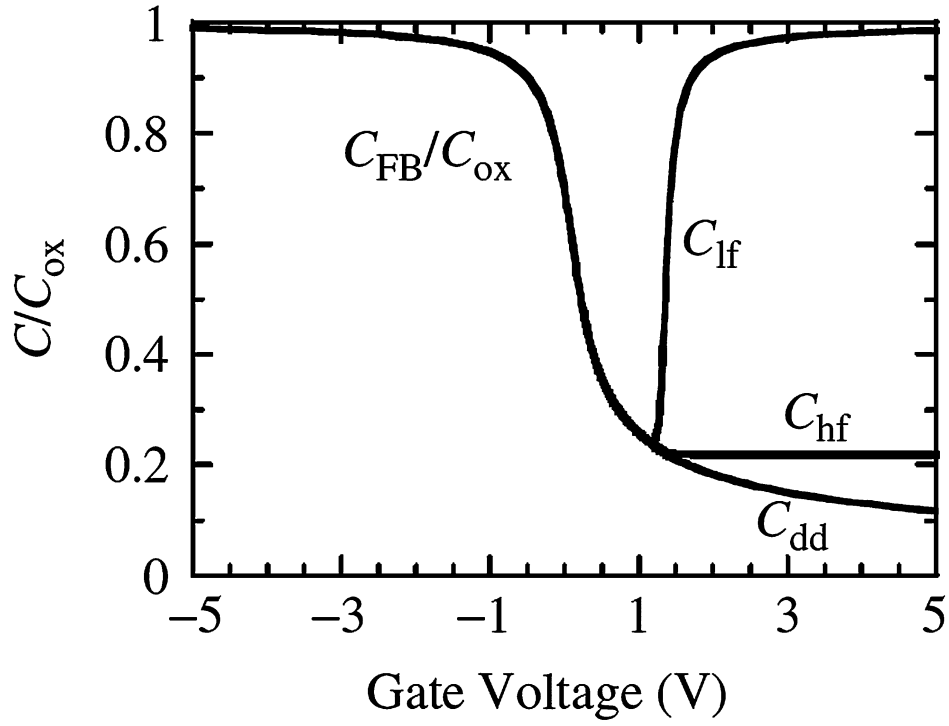

Figure 22. *Low-, high-frequency and deep-depletion capacitance-voltage curves from ideal MOS-capacitor in which semiconductor substrate is p-type. The figure is taken from Ref. 182.*

The real MOS-structure is usually far from ideal and especially the semiconductor-oxide interface contains defects and the associated energy levels distributed both in space and energy, as described earlier. When the gate-voltage is modulated, the interface defect states can be charged or discharged depending on the polarity of applied bias and the energy-level position of the defect relative to the Fermi-level. Therefore, the interface traps produce an extra capacitance component and the measured CV-curve may drastically differ from the ideal curve of Fig. 22, especially in the low-grade III-V MOSCAPs. As a result of the interface defects, the measured CV-curve usually "stretches" along the voltage axis, making shallower dip compared with the ideal case at low-frequency measurement.[10,182] Also, if the interface contains fixed charges, the whole CV-curve can be shifted. Furthermore, a commonly

observed defect related CV-behavior in the III-V MOSCAPs is the frequency dispersion of the accumulation capacitance[7] as can be seen in Fig. 23. This behavior can be reasonably described by the DIGS model[96] (Chapter 1.3.3) and assuming quantum mechanical tunneling of the charge carriers into the interface defects, induced by a thin disordered region.

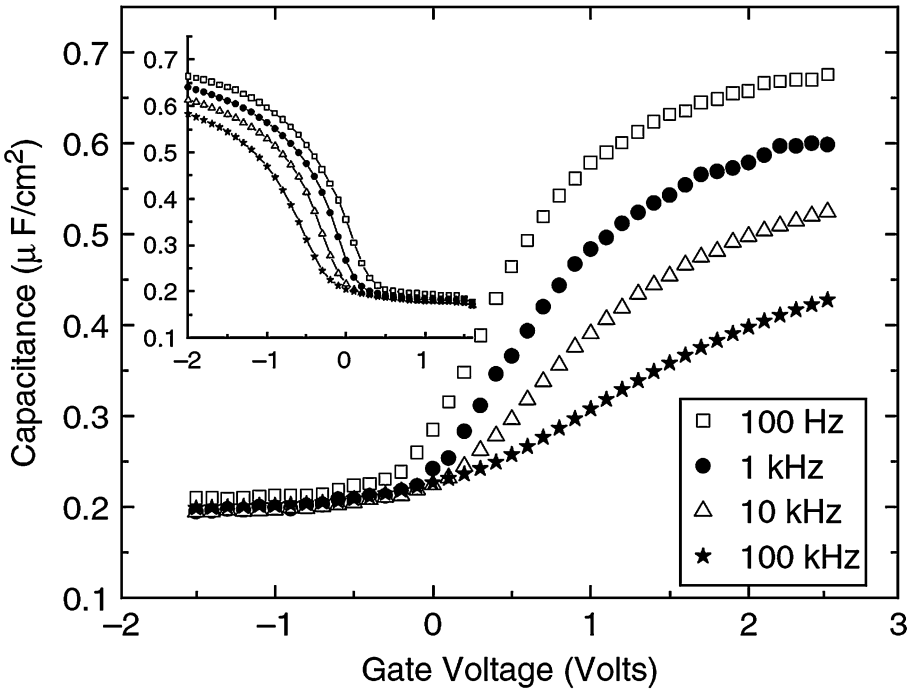

Figure 23. *Capacitance-voltage frequency dispersion of n- and p-type (inset) Al_2O_3/GaAs MOS-capacitor. The figure is taken from Ref. 7.*

2.1.6 Sample preparation

The delicate nature of the III-V substrates studied in this thesis requires an ultrahigh vacuum environment for producing the well-defined surfaces for the experiments. In general, the samples (about 5 mm × 10 mm rectangles) were cut from commercial III-V(100) 2'' wafers and introduced into the vacuum

system via a loading chamber. Within this work, the most common cleaning procedure involved Ar-ion sputtering and annealing cycles for the removal of amorphous oxide layer prevailing at the air-exposured wafer surfaces. The annealing temperature depends on the choice of the III-V substrate and for example the GaAs(100) substrate can sustain higher temperatures (up to 600 °C) than for example the InAs(100) and InSb(100) substrates (up to 500 °C) without decomposing the crystal. Usually, after 3-4 cleaning cycles, a well-defined group III-rich reconstruction can be seen by LEED and STM measurements. XPS was also used to check the removal of impurity atoms (e.g. carbon and oxygen) in the cleaned samples. In addition, MBE was used to produce good quality III-V surfaces in two distinct ways. At the beamline 41 of MAXLAB, it was possible to grow various III-V materials by interconnected MBE chamber and subsequently transfer the clean sample under UHV to the measurement chamber for further sample preparations and characterization. Furthermore, MBE was used through collaboration for growing good quality III-V samples, which were capped by a thick arsenic layer. This capping layer can be easily removed at the University of Turku UHV-chamber by thermal annealing, providing a clean surface.

Metal-adsorbate induced surface structures were produced using different evaporators and quartz-crystal microbalance facilities for flux calibration. For depositing tin atoms (Sn), a home-made tungsten-coil evaporator was used and for the In deposition, a tantalum-pocket (or envelope) with a pinhole was used. When the electrical current is passed through the filament of the evaporator, the metal is heated and evaporated from the liquid or solid phase into the vacuum. The resulted adsorbate flux can be measured by the QCM. When the flux is saturated and calibrated, a desired amount of metal atoms can be deposited to the sample. After subsequent sample annealing, the adsorbate-covered surface is usually reconstructed. However, the parameter space, i.e. the annealing temperature and the time as well as the ad-atom concentration, can strongly affect the resulting surface reconstruction and the surface quality. The oxidation experiments were done under UHV-conditions for the cleaned III-V(100)

surfaces by introducing molecular oxygen into the vacuum chamber. Oxygen partial pressure was controlled by a leak-valve and for the thermal oxidations, the sample temperature was raised by a resistive heating element.

In order to study the effects of particular surface structure on device characteristics, metal-insulator layers were fabricated in the University of Turku UHV system for later MOSCAP processing. The insulator layers were fabricated by using home-made atomic-layer-deposition and e-beam evaporator. ALD insulator growth mechanisms are not covered here, but the reader is encouraged to familiarize oneself with excellent review-article of Puurunen.[183] E-beam evaporation was performed by concentrating a high flux of electrons into a crucible containing the desired dielectric crystal. The e-beam evaporation was performed under O_2 rich environment. The instrumentation and insulator growth process of home-made ALD-reactor is concerned more profoundly in Chapter 3.7.

2.2 Computational methods

The complexity of the quantum mechanical many-body problem of the solid state physics, described below, requires considerable amount of computing power. Therefore, the calculations performed within this work were computed with supercomputers. Through the making of this research five different supercomputers were used: a local super-cluster of the University of Turku (Pleione) with 3 TFlops of capacity, Murska (11.3 TFlops), Vuori (33.9 TFlops) and Sisu (245 TFlops) of CSC – IT Center for Science, Finland.

The basis for the description of atomic scale phenomena including the solid state matter is the quantum mechanics. More generally, in order to study the stationary properties of a quantum mechanical system one has to solve the time independent Schrödinger eigenvalue equation:

$$H\Psi(\mathbf{r},\mathbf{R}) = (H_{el} + H_{nucl})\Psi(\mathbf{r},\mathbf{R}) = E\Psi(\mathbf{r},\mathbf{R}) \quad (25)$$

where H is the Hamiltonian of the system, which is composed of electronic and nuclei-Hamiltonians H_{el} and H_{nucl} respectively and E is the energy of the system. [8,151,184,185] The state of the system is completely described by its wave-function Ψ. The Hamiltonian embodies the operators corresponding to kinetic and Coulomb potential energies of electrons and nuclei. It is evident that solving equation (25) explicitly for systems of more than two particles is very difficult and therefore approximations are needed. The first approximation one can safely presume is the Born-Oppenheimer approximation[186] in which the movement of the electrons and the atomic nucleus can be separated from each other. This stems from the fact that the nucleus is much more massive than electrons and the electrons can be considered to relax instantaneously to their ground state in any ionic configuration. Furthermore, the nuclei can be presumed to form a static lattice, i.e. the $\mathbf{R}$ vector remains constant for all ions. Thus, the original wave-function Ψ in equation (25), which included the terms of both nuclei and electrons, can be separated to a wave-function which is a product of nuclei and electron wave-functions. The movement of electrons can be therefore described by considering fixed nuclei and their corresponding electrostatic fields. Furthermore, the dimensions of the eigenvalue equation (25) can be reduced by assuming the one-electron-approximation wherein the N electron Schrödinger equation is separated into N one-electron Schrödinger equations and the N-particle state of the N electrons in the material under consideration can be obtained:[184,185]

$$H\Psi = \sum_{i=1}^{N}\left[-\frac{\hbar^2}{2m_i}\nabla_{\mathbf{r}_i}^2 - \sum_R \frac{2Ze^2}{4\pi\varepsilon_0|\mathbf{r}_i - \mathbf{R}|} + \sum_{i\neq j}\frac{e^2}{4\pi\varepsilon_0|\mathbf{r}_i - \mathbf{r}_j|}\right]\Psi = E\Psi \quad (26)$$

Unfortunately, the many-body problem is still far from simple to be explicitly solved as a macroscopic piece (one mole) of crystal contains around 10^{23} electrons. However, the atoms in a solid state material are usually crystallized into periodic array following some symmetry operators (e.g. translational, rotational and/or mirror symmetry operators) and the physical crystal can be therefore described by a mathematical Bravais lattice with a basis. The crystalline nature of the solid makes the theoretical workload far easier and straightforward. Because the atoms are arranged in a periodic fashion, also the potential produced by the nuclei and experienced by the electrons is periodic. The implementation of periodic potential into Schrödinger equation leads to famous Bloch's theorem, which states that in any system with Bravais symmetry and with potential $U(\mathbf{r}+\mathbf{R})=U(\mathbf{R})$ the eigenstates of the Hamiltonian can be expressed as a product of a plane-wave and a periodic function with the same periodicity as the potential.[151] The significance of Bloch's theorem is the drastic reduction of the dimension of the Schrödinger eigenvalue equation. It turns out that it is only necessary to solve the solution of Schrödinger equation within the primitive cell of the reciprocal lattice, i.e. within the first Brillouin zone.

Even though the eigenvalue problem is simplified by taking into account the approximations and Bloch's theorem, the problem is still not possible to be solved analytically (hydrogen being an exception). An approximate solution is however possible to obtain numerically and using the variational principle. The notable case among such methods is the Hartree-Fock (HF) method.[151,185] In the Hartree-Fock method the many-body potential energy term in Hamiltonian is simplified by dividing it into an exchange potential term and the electron density dependent Hartree potential term. The antisymmetric electron wave-function is described by Slater determinant. The HF equations are nonlinear and solved self-consistently; first, the initial electron density distribution is guessed, second, the wave-functions are obtained by solving the Schrödinger equation with the guessed electron density, and third, new electron density distribution is

calculated from the previously solved wave-functions. The procedure is repeated until the electron density distribution is converged. The drawback of the Hartree-Fock method is the high computational demand which makes it suitable only for relatively small systems. On the other hand, HF-method does not take into account electron correlation effects.

2.2.1 Density functional theory

The density functional theory has perhaps been the most important cornerstone for the development of *ab initio* calculations and simulations of solid materials. In 1964, Hohenberg and Kohn showed the special role of the density of the particles in the ground state of quantum mechanical many-body system.[187] Later in 1965 Kohn and Sham formulated the Kohn-Sham approach to replace the many-body problem with an auxiliary independent particle problem, now known as the density functional theory.[188]

According to Hohenberg and Kohn Theorem I (so called existence theorem), for the system of interacting particles in an external potential $V_{ext}(\mathbf{r})$, the external potential is unambiguously determined, except for a constant, by the ground state particle density $\rho(\mathbf{r})$. Thus, the Hamiltonian is fully determined except for a constant and the ground state particle density completely determines all the properties of the system. Theorem II of Hohenberg and Kohn states that the electron density of the ground state minimizes the total energy functional $E = E[\rho(\mathbf{r})]$ for any particular external potential $V_{ext}(\mathbf{r})$. The significance of these theorems is the gradual elimination of variables from the “traditional” 3N-dimensional Schrödinger equation into just three, as the particle density is a function of only three spatial coordinates. However, the exact form of the functional is unknown within these theorems as well as the explicit way to predict the electron density.

In general, the total energy of interacting electron gas, according to Hohenberg and Kohn can be expressed as follows:[187]

$$E[\rho(\mathbf{r})] = T(\rho) + V_{ext}(\rho) + V_{ee}(\rho) = T(\rho) + \int V_{ext}\rho(\mathbf{r})d^3\mathbf{r} + V_{ee}(\rho) \qquad (27)$$

where the $T(\rho)$ and $V_{ee}(\rho)$ are universal but unknown kinetic energy and electron-electron interaction energy functionals respectively of the interacting electron gas. The external potential $V_{ext}(\rho)$ is not universal as it depends on the system under study.

Kohn and Sham suggested an auxiliary system and postulated that the ground state electron density of the original system with interacting particles is equal to some chosen, i.e. auxiliary, non-interacting system.[188] The problem is therefore simplified to independent electron equations of non-interacting particles and the solution can be obtained numerically. The difficult many-body terms are included in the exchange-correlation functional $E_{XC}(\rho)$ and therefore the Kohn-Sham approach, although it involves the independent electrons, it now includes effectively interacting electron density. The total energy functional according to Kohn-Sham approach is:[188]

$$E[\rho(\mathbf{r})] = T^{NI}(\rho) + V_{ext}(\rho) + V_H(\rho) + E_{XC}(\rho) \qquad (28)$$

where $T^{NI}(\rho)$ is kinetic energy functional of non-interacting electrons and $V_H(\rho)$ is classical (Hartree) Coulomb interaction energy. The error that is made by including the kinetic energy term of non-interacting electrons as well as the classical electron-electron interaction defines the exchange-correlation functional:

$$E_{XC}(\rho) = \left[T(\rho) - T^{NI}(\rho)\right] + \left[V_{ee}(\rho) - V_H(\rho)\right] \tag{29}$$

Furthermore, the electron density of interacting electron gas in external potential $V_{ext}(\rho)$ can be obtained from the electron density of non-interacting electron gas in effective potential $V_{eff}(\rho)$ and thus the Kohn-Sham eigenvalue equation of the auxiliary system with Hamiltonian H^{NI} of non-interacting electrons in effective potential now has the form:

$$H^{NI}\psi_i(\mathbf{r}) = \left[-\frac{\hbar^2}{2m}\nabla^2 + V_{eff}(\mathbf{r})\right]\psi_i(\mathbf{r}) = \varepsilon_i\psi_i \tag{30}$$

which should be solved self-consistently with electron density:

$$\rho(\mathbf{r}) = \sum_{i=1}^{N}\left|\psi_i(\mathbf{r})\right|^2 \tag{31}$$

The self-consistent solution is required due to the non-linear dependence between the effective potential and the electron density. In general, the Kohn-Sham approach provides an exact method for finding the ground state energy for the many-body problem imposed by the theory of solid state physics, albeit it requires the knowledge of the exchange-correlation functional.

The first and the most widely exploited exchange-correlation functional for the DFT calculations is the local-density approximation (LDA). It was first proposed by Kohn and Sham and later parameterized by Perdew and Zunger.[189] In the LDA formalism, the electron density is assumed to be homogenous within the differential piece of material and the exchange-correlation energy is obtained by adding all the differential pieces together:

$$E_{XC}(\rho) = \int \rho(\mathbf{r}) \varepsilon_{XC}(\rho(\mathbf{r})) d^3\mathbf{r} \quad (32)$$

where ε_{XC} is the exchange-correlation energy of homogenous electron gas, which can be calculated e.g. by Monte-Carlo simulations as suggested by Ceperley and Alder.[190] Furthermore, a more accurate implementation of the exchange-correlation is achieved by including also gradients of the electron density in addition to the pure electron density of homogeneous electron gas. This approach is known as the generalized-gradient-approximation (GGA)[191,192] of which perhaps the most widely used implementation is the functional derived by Perdew, Burke and Ernzerhof, known as the PBE functional.[193]

The abovementioned exchange-correlation functionals suffer from several drawbacks in predicting some of the properties of materials. For example, the semiconductor band gaps are considerably underestimated when using LDA, GGA or PBE functionals for electronic structure calculations.[194,195] Furthermore, the binding energies of many systems may be overestimated while the diffusion energy barriers can be severely underestimated for example. The main reason is the fact that in many systems, the exchange part of the exchange-correlation energy dominates over the correlation energy. Therefore, for example in accurate electronic structure calculations, it is reasonable to include a portion of the exact exchange from the Hartree-Fock theory with the exchange and correlation acquired from the DFT. These functionals are called hybrid functionals and albeit they require significantly more computational resources, in turn they provide accurate results for electronic structures for example.[196,197]

2.2.2 Surface calculations

Within the context of this work, DFT calculations were used for the III-V compound semiconductor surface structure determination. Calculations were done using Vienna *ab initio* simulation package (VASP).[198-201] VASP computes an approximate solution to many-body Schrödinger equation by solving the Kohn-Sham equations within the DFT formalism. Additionally, approximate solution for Schrödinger equation can be obtained by the pure Hartree-Fock method or by utilizing the hybrid functionals. VASP expresses one-electron orbitals, electronic charge density, and the local potential in a plane-wave basis set. Electron-ion interactions are described by using norm-conserving ultrasoft pseudopotentials[202] or by projector-augmented-wave (PAW) method.[203,204] Moreover, VASP uses efficient iterative minimization algorithms for the electronic ground state determination.[205]

Considering surface calculations, there are different approaches that can be utilized, most notably the cluster model and the supercell model. In the cluster model, the surface is modeled by a small isolated cluster of atoms, of which one facet has the same symmetry as of the studied lattice. The supercell method, which was used in this work, includes a slab which is infinite and periodic in the directions parallel to the surface and a vacuum region which separates the slabs perpendicular to the surface. The supercell method is more suitable for the semiconductor surface calculations as it enables the formation of dispersive electronic band structures for the detailed electronic structure analysis. An example of a typical slab for reconstructed III-V surface calculation is shown in Fig. 24. The sub-surface III-V material is modeled by tetrahedral coordinated group III and group V atoms. The bottom facet of the slab is passivated by fractionally charged pseudohydrogen atoms (orange balls) so that the number of electrons in each bottom-surface group III/V-hydrogen bonds is two. Hence, the pseudohydrogens have a fractional charge of 1.25 or 0.75 depending on how the bottom surface is terminated. This kind of

pseudohydrogenation is very useful in the calculations, because in this way the bottom slab resembles the bulk semiconductor material very well. The top facet of the slab in Fig. 24 resembles the atomic structure of the III-V surface, which is this time reconstructed so that the initial bulk symmetry is lowered so that the translation periodicity is ×4 along the [011] direction. The top-surface is separated from the pseudohydrogenated bottom-surface by a vacuum region which should be chosen wide enough in order to minimize the interactions between these two surfaces. However, the top and bottom surfaces may still interact because the charge-density distribution can be (and usually are) very different from each other, resulting in a net dipole moment within the slab. This extra dipole moment strongly affects the calculated total energy of the slab and yet hinders the convergence of the calculation. Therefore, it is necessary to use dipole-corrections in calculations. The corrections to the total energy are calculated as the energy difference between a dipole in the studied supercell and the same dipole placed in a supercell with the corresponding lattice vector approaching infinity.[205]

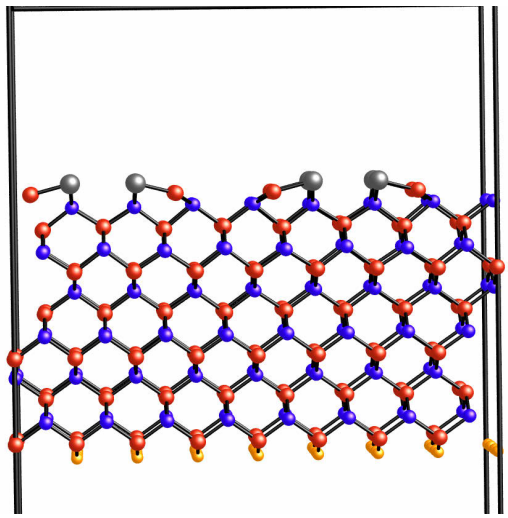

Figure 24. *An example of slab used in super-cell calculations. Top of the slab resembles the surface atomic structure of Sn-stabilized InAs(100)(1×4) reconstruction. The bottom of the slab is passivated by pseudohydrogens*.

In general, the determination of surface structure usually requires additional information from the studied system which can be acquired for example by complementary experimental methods. Considering the reconstructed III-V surfaces, the surface symmetry (which determines the unit-cell used in calculations) can be determined by LEED for example, and additional hints about the surface structure can be obtained by STM and photoemission measurements. Thereafter, for the computational surface structure determination, it is required to calculate several possible atomic configurations that can be generated for example by the pure trial-and-error procedure or by more sophisticated genetic algorithms and/or Monte-Carlo and molecular dynamics (MD) simulation methods. Within the frame of this work, the calculated atomic configurations were mainly generated by trial and error due to the extensive former knowledge of the studied structures (Papers 1 and 3). However, MD simulations and related techniques were employed in the structure determination of the atomic structures found and described in the Papers (4-6) due to the novelty of these structures and large configuration space. Monte-Carlo and genetic algorithm based structure generation techniques are beyond the scope of this work.

The stable surface structure has the lowest surface free energy density γ_S as described in Chapter 1.2 and the surface energy comparison between the calculated atomic configurations can be done in respect of the chemical potentials. Therefore, in order to construct a surface phase diagram for the energetically favorable atomic configurations of the system of interest, it is also necessary to perform bulk calculations for the atomic constituents making the studied system in order to determine the range of chemical potentials in the surface phase diagram. Because the DFT is a ground state theory, the calculated phase diagram gives the relative stability between the different atomic models at 0 K temperatures. The finite temperature effects for the atomic configurations can be included by configurational entropy considerations as described in Ref. 206 for example.

The total energy minimum is a very important justification for the proposed atomic model. In addition, it is useful to simulate all possible measurements for the energetically favored atomic models in order to find out the structures appearing in the real experiments. In principle, if the atomic model does not provide (or reproduce) all the measured properties, the model is not exactly correct. Surface core-level shifts give useful information about the different bonding environment of particular atoms at the surface as described earlier. SCLS can be calculated by calculating an average electrostatic potential at the core for the surface and more bulk-like atoms of the slab and comparing the obtained energies with each other.[207,208] Theoretical SCLS were also calculated in this work, in order to compare the SCLS of energetically most favorable atomic models to the experimentally measured and fitted SCLS spectra. In the comparison between the measured and calculated shifts, it is useful to consider the agreement between the most negative and the most positive shifts found in the measurements and calculations. For example, if the atomic model provides a calculated shift (component) which energy is larger than the largest shift seen in experiments, the model can be reasonably excluded. Furthermore, STM images can be simulated also by calculating partial charge density for the electrons with eigenvalues in the desired range from the Fermi-level, within the framework of Tersoff and Hamann scheme.[160] However, this kind of calculation does not take into account the accurate influence of the STM tip and thus, the comparison between the experimental and computational STM images should be taken with care.

3 Summary of results and discussion

The experimental and computational research carried out in this work focused on solving the atomic structures on two technologically important adsorbate induced III-V surface structures, namely the Sn-induced and In-induced surface reconstructions (Papers 1 and 3). In addition, novel and beneficial properties of

these structures were discovered (Papers 2, 4 and 5). Namely, it is demonstrated that the detrimental amorphous III-V-oxide formation can be suppressed by using an ultrathin Sn-layer (Paper 2) or by the atomic scale engineering of the III-V surface by producing crystalline oxide layers (Papers 4 and 5). The discovery of highly ordered crystalline oxide layers was further exploited for studying the atomic and electronic properties of oxidized InSb(100) surface in Paper 6. Furthermore, preliminary device tests were also performed within this work as described in Chapter 3.7. The device tests required substantial instrumentation of the University of Turku UHV-chamber, namely the atomic-layer-deposition reactor designing and fabrication, which is also briefly summarized in Chapter 3.7. This Chapter gives a brief overview about the main results of this thesis, described more profoundly in the actual Papers.

3.1 Tin-induced structures on InAs(100) and GaAs(100) surfaces (Paper 1)

The quality of the epitaxially grown III-V film stacks can be improved by using surfactant mediated growth as described in Chapter 1.3.1. Previous experiments have demonstrated that a group IV atom, Sn can act as a surfactant in the GaAs epitaxial growth, improving the quality of the surfaces and interfaces especially at low temperature growth conditions.[209-211] This beneficial property has been related to the enhancement of surface cation mobilities due the Sn-modified surface structure.[210] Furthermore, the Sn pre-layer deposited on III-V surfaces has been found to eliminate interfacial defects efficiently.[209] However, the atomic structures of these beneficial Sn-induced III-V surfaces have remained unresolved so far. Paper 1 elucidates this issue.

By comparing the previous sample preparation conditions of the benefial Sn-covered III-V surfaces, their structures can be linked to the III-V(100)(1×2)-Sn reconstruction.[209-212] In Paper 1, the most probable atomic structures of the Sn-induced (1×2) reconstructions on GaAs(100) and InAs(100) are discovered by

combining experimental LEED, STM and PES measurements and DFT calculations. The main building blocks of the III-V(100)(1×2)-Sn surfaces are presented in Fig. 25. They are Sn − group-III dimers. It is interesting that depending on the relative orientation of the Sn-III dimers, the surface unit cell is (1×2) or (1×4) as shown in Fig. 25.

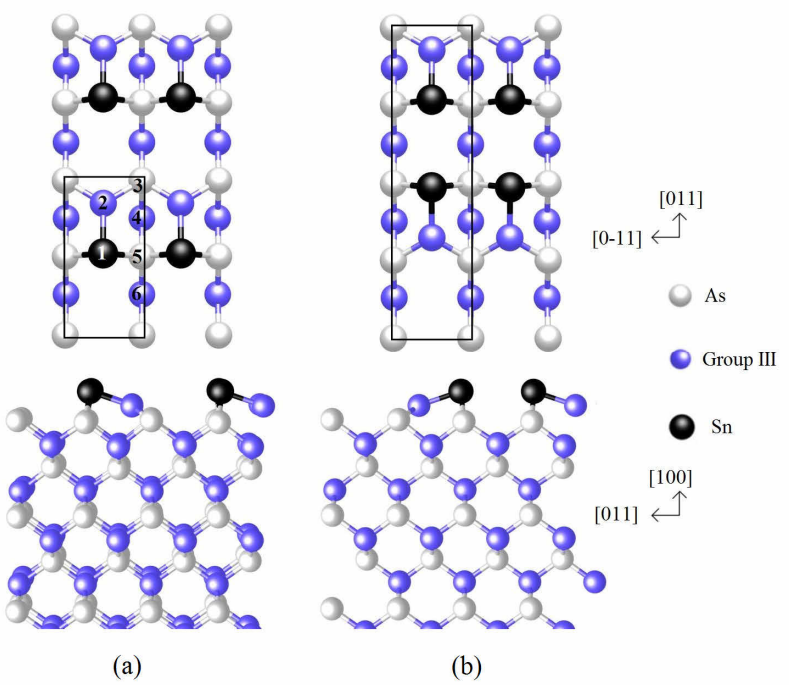

Figure 25. *Atomic model for IIIAs(100)(1×2)-Sn surface (a) and for IIIAs(100)(1×4)-Sn surface (b). The surface unit cells are highlighted by black rectangles.*

The calculated surface phase diagrams for the Sn-covered GaAs(100) and InAs(100) surfaces, shown in Fig. 26 demonstrate the energetically most favorable atomic models relative to clean substrate surface structures. In addition to Sn-III dimers, the formation of Sn-As dimers is favorable in the As-rich conditions on the GaAs(100). In this model, the top surface dimer composition is Sn-As (Sn atom occupies atomic site 1 and As atom occupies

atomic site 2 in Fig. 25a). Moreover, the (1×4)-SnGa atomic model is energetically the most favorable structure in the Ga-rich conditions. The corresponding (1×2)-SnGa model was found to be only 7 meV / (1×1) higher in energy compared to (1×4) model. Therefore, it is expected that both symmetries and corresponding atomic structure can exist at room temperature conditions. As compared with the other group-IV adsorbates (i.e., Ge and Si),[213-215] it seems that the tin atoms tend to occupy the topmost dimer sites, while the Ge and Si atoms reside subsurface at the atomic site 5 in Fig. 25a. Thus the top-surface dimer composition is Ga-As for the GaAs(100)(1×2)-Ge reconstruction for example.

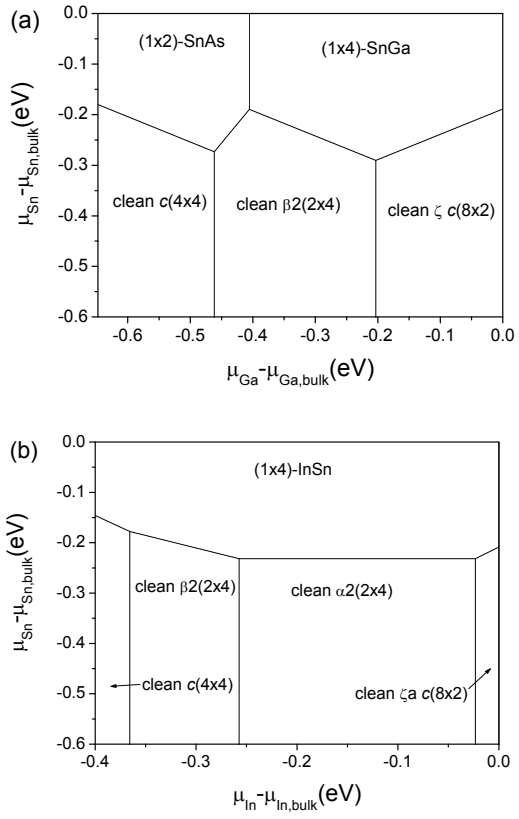

Figure 26. *Calculated surface energy phase diagrams for GaAs(100)-Sn surface (a) and for InAs(100)-Sn surface (b).*

For the Sn-stabilized InAs(100) surface, the only stable structure was found to be (1×4)-SnIn model, which is energetically the most favorable structure through the whole Sn-rich area of the phase diagram. The found (1×4) structure (Fig. 25b) is rather peculiar because the distance between the occupied dangling bonds is decreased compared with atomic structure with the (1×2) symmetry. Traditionally, it is believed that the surface dangling bonds tend to arrange themselves so that the electrostatic repulsion between dimers is minimized at the stable surface structures. In Paper 1, it was found that the stabilization of (1×4) structure depends on the size of the group IV adsorbate atomic constituent and the stabilization is most pronounced for the Pb-induced (1×4) reconstruction. It was also found that only atomic models with 0.5 ML of Sn concentration are energetically stable. Higher Sn concentrations lead to highly unstable structures even at the very Sn-rich conditions of the surface phase diagram. This finding is however in accordance with the experiments, where it was observed that high Sn deposition flux readily leads to the formation of Sn clusters which can be observed by STM measurements. Thus, the Sn starts to grow 3-dimensionally in the post 0.5 ML of Sn concentration and no 2-dimensional reconstruction occurs.

The measured STM images from InAs(100)(1×2)/(1×4)-Sn support the coexistence of both (1×2) and (1×4) structures as can be seen from the high resolution filled-state STM image shown in Fig. 27a. Moreover, the correspondence between the measured and the simulated STM image for (1×4)-SnIn (Fig. 27b) was found to be very good. Surface core-level shifts were also calculated in Paper 1 for the energetically favorable atomic models of GaAs(100)(1×2)/(1×4)-Sn and InAs(1×2)/(1×4)-Sn systems. By comparing the calculated SCLS with measured ones (Fig. 28), made by angle resolved PES, it is evident that only III-Sn dimer model reproduce the shifts reasonably well, supporting all the other results. To conclude the results of Paper 1, both the calculations and the measurements made by STM and PES suggest that the

surface is composed of (1×2) and (1×4) building blocks which include III-Sn dimers rather than III-V dimers.

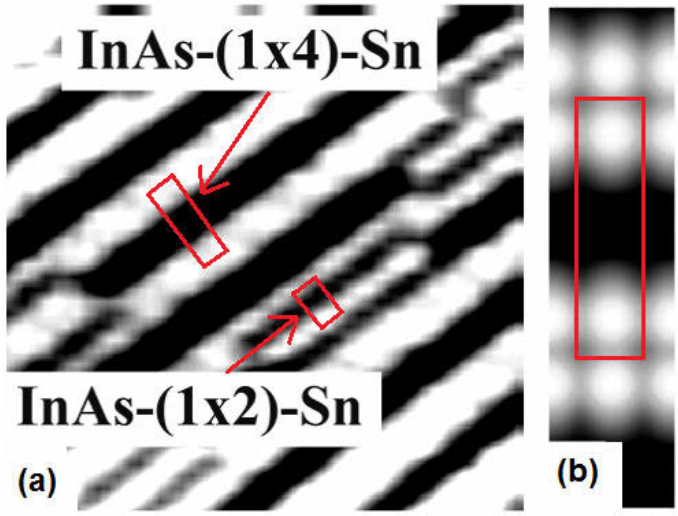

Figure 27. *(a) Measured filled-state (2.89 V) STM image from InAs(100)(1×2)/(1×4)-Sn surface. The image's dimensions are approximately 6.5 nm × 6.5 nm. The (1×4) and (1×2) surface unit cells are highlighted by red rectangles. (b) Calculated filled state STM images (2.89 V) for SnIn(1×4) atomic model.*

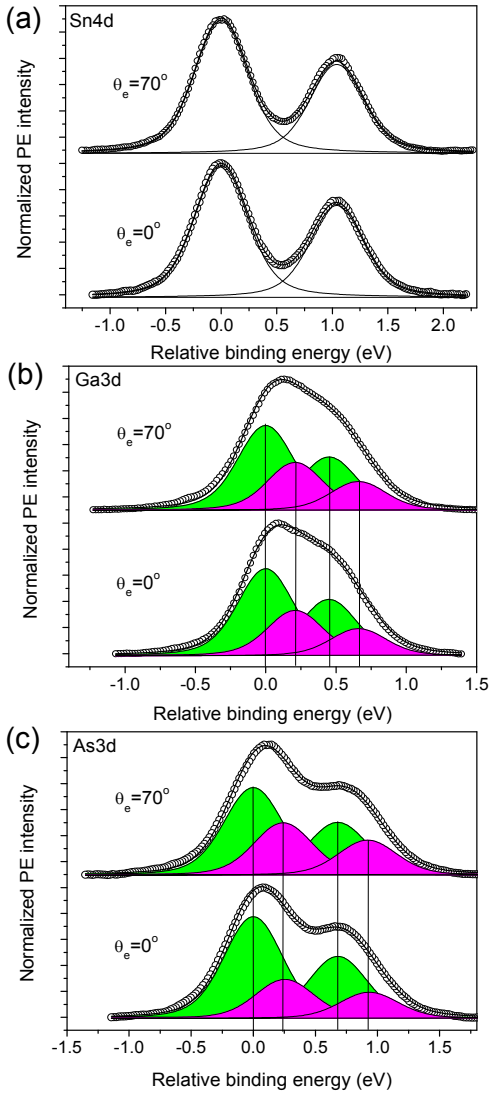

Figure 28. *Fitted Sn4d (a), Ga3d (b) and As3d (c) core-level spectra of GaAs(100)(1×2)/(1×4)-Sn surface. The spectra were measured with different emission angles (0° and 70°). Photon energy was 60 eV for Sn4d and Ga3d and 74 eV for As3d. All the spectra are normalized to their maxima. Bulk components are shown as green peaks while surface components are shown as violet peaks.*

3.2 A new method to remove harmful oxides of III-V semiconductor surfaces (Paper 2)

As described in Chapter 1.3.3, the formation of amorphous oxide layers on the III-V surfaces and interfaces can lead to detrimental effects regarding the semiconductor device applications. The oxide layers are easily formed for example during the manufacturing of the MOS device stacks because it is very difficult or impossible to avoid an oxygen exposure of III-V surfaces in the process. Therefore, the removal of disordered III-V layers is highly desired in the processes of state-of-the-art semiconductor devices, notably in MOSFET applications. In Paper 2, a new method for decreasing or removing the III-V oxides is demonstrated. It is based on the Sn-covered (1×2)-reconstructed InAs(100) and GaAs(100) surfaces characterized in Paper 1. It was found that the oxidized III-V surface layers containing Sn have an interesting property to remove the oxygen out from the oxidized III-V layer, i.e. to catalyze the oxygen removal during post heating. This procedure is summarized next.

First, the (1×2) reconstructed GaAs(100) and InAs(100) surfaces were prepared by depositing tin on GaAs(100) and InAs(100) surfaces and post heating these Sn-covered samples. The recorded SRPES spectra of As3d, Ga3d and Sn4d from GaAs(100)(1×2)-Sn surface at this stage are shown in Fig. 29a. The samples were then air-oxidized by taking them out from the UHV-chamber. The resulted spectra from the oxidized GaAs(100)-Sn, in Fig. 29b, shows a clear difference for the As3d, Ga3d and Sn3d emissions. Namely, a clear As-oxide emission can be seen, as expected, with at least three new surface related components. Also Ga3d and Sn4d emissions show a clear evidence of surface related shifts into the higher binding energy, suggesting the formation of Ga- and Sn-oxides. It is noted that the sample surfaces were completely disordered as the LEED pattern did not show any diffraction peaks.

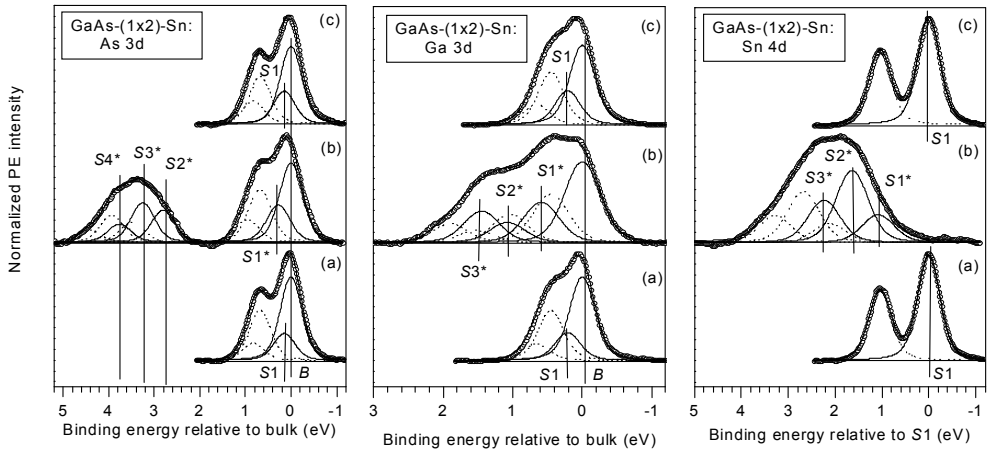

Figure 29. *As3d, Ga3d, and Sn4d photoemissions from GaAs(100)(1×2)-Sn (a) before air-exposure, (b) after air-exposure, and (c) after heating the oxidized sample.*

Surprisingly, the post-annealing of the air-oxidized and Sn-containing GaAs (InAs) under UHV environment at 550 °C (350 °C) produced again the well defined (1×2) reconstruction according to LEED measurement. Also, the SRPES spectra (Fig. 29c) were almost identical in comparison with the non-oxidized starting (1×2) structure (Fig. 29a), suggesting that the Sn-containing interface layer somehow catalyzes the removal of amorphous oxide layer formed by air-oxidation. Such effect is not observed for the reference sample without the Sn-layer. It is worth noting that the Sn-containing III-V layers, oxidized in air as long as one week, recovered as described above.

In Paper 2, the effects of (1×2)-Sn layer for oxide removal were also investigated by *ab initio* calculations. The Sn induced (1×2) structure, as well as *c*(8×2) and β(2×4) structures with different amount of Sn-coverage were adopted in the calculations in order to study the adsorption/desorption energies for oxygen. The total energy results show consistently that when the Ga/In (As) atom is replaced by Sn in the *c*(8×2) or β(2×4) structure, the

adsorption/desorption energy is decreased (increased) by 0.1 eV – 0.8 eV regardless of the surface Sn coverage. That is, the oxygen is more easily desorpted when Ga/In is replaced by Sn atom. The Sn induced (1×2) structure for GaAs(100) and InAs(100) has fewer group III atoms at the surface compared to clean *c*(8×2)-ζ or *c*(8×2)-ζa atomic structures. Therefore, as the oxidation process is mainly limited to surface layers, it is expected that in the Sn induced reconstruction the number of strong group III-O bonds is suppressed upon the oxidation process.

The novel finding of the Sn-induced catalysis of amorphous surface oxide can have several benefits regarding the III-V semiconductor device fabrication. The results suggest that it is helpful to deposit thin Sn-layer on top of the III-V material before the MOS-stack growth, for example. A post heating of the stack in a proper stage of the growth might result in the useful re-arrangement of the oxide/III-V interface. Furthermore, in a common device (e.g. QW-laser and solar-cell) fabrication process, albeit the device stack is perhaps fabricated in UHV environment, the metal contacts for example are grown in other chamber, exposing the freshly prepared device stack to atmosphere conditions and the surfaces of the semiconductor chip are therefore thoroughly oxidized and contaminated. Such oxidized surface usually leads to barrier formation in metal-semiconductor junctions, and therefore the removal of amorphous oxides is desirable in these re-growth processes.

3.3 Effects of indium deposition on GaAs(100) surface (Paper 3)

One of the first examples of surface engineering was given in Chapter 1.3.2 by referring to the study of Anan *et al.*[76] where the beneficial effects of indium deposition were demonstrated for the technologically important III-P/III-As heterostructures. In particular, it was found that the deposition of 1 ML indium changed the symmetry of the growth-front from (2×4) to *c*(8×2) and substantial

improvement of the interface quality is observed as deduced by the 100-fold improvement of the PL-intensity. A similar improvement of the interface has been also observed in III-V insulator interfaces, where the In-rich surface was found to suit better for starting surface for insulator growth for example in InGaAs MOS structures.[146-148] From the basic-research's perspective, the atomic structure of the In-rich III-V surface, notably the structure of *c*(8×2) reconstruction, is of importance for elucidating the reasons behind these beneficial effects of this surface structure. The computational and experimental research performed in Paper 3 concentrates on solving the detailed structure of the In-rich GaAs surface. For the first time, the substantial stability of the ζa structure is demonstrated and supported by *ab initio* calculations and STM measurements.

The most-likely atomic structures for the *c*(8×2) symmetry are the ζa and ζ models, shown in Fig. 30a and b respectively, with different amount of indium ad-atoms. Various other models, including the (2×4) symmetry, were also included in the extensive calculations performed in Paper 3. The calculated surface phase diagram shown in Fig. 31a demonstrates the stability of ζa structures relative to the clean substrate reconstructions. The stability of the ζa model is significant, as the cross-section of the surface phase diagram in Fig. 31b shows. This cross-section was taken at the very In-rich limit (μ_{In}-$\mu_{In,bulk}$=0 eV). Notably, the previously proposed ζ model[55] is 122 meV / (1×1) higher in energy compared with the ζa model. This was the first theoretical evidence of the stable ζa structure on any III-V surface. Even the modified ζ structure, where the top surface In-In dimer (atomic sites 4 and 4') is intentionally broken is more stable than the pure ζ model, even though the "breakage" of the dimer leads to a metallic surface.

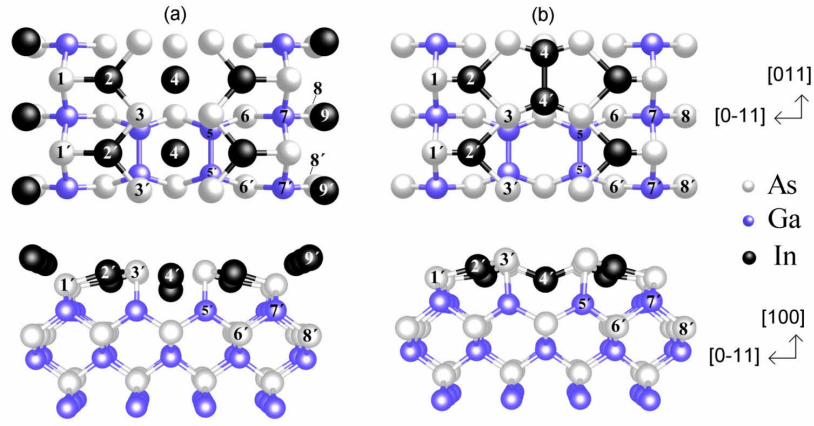

Figure 30. *(a) ζa and (b) ζ reconstruction of the In/GaAs(100)c(8×2) surface.*

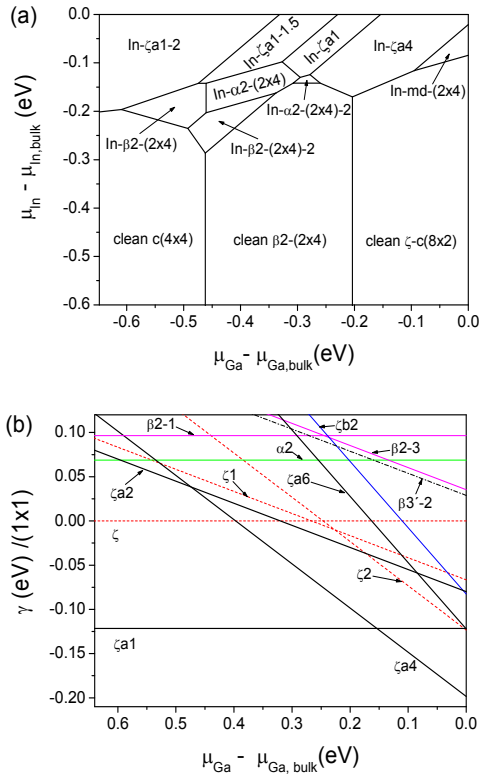

Figure 31. *(a) Surface phase diagrams for the GaAs(100)-In surface. (b) Energy diagram of the In/GaAs(100) surface in the In-rich limit* $\mu_{In} = \mu_{In,bulk}$. *Figure is taken from Paper 3.*

The relative stability of the ζa atomic model was found to depend on the surface cation size and the substrate volume. Namely, the stability of ζa is increased, when the cation size is increased or the substrate volume is decreased. For small group III adsorbate atoms, such as B, Al and Ga on GaAs substrate, the ζ is more stable but for In and Tl atoms the situation is opposite. Also the In concentration affects the relative stability; when the indium concentration is increased in the ζa structure, the surface energy is reduced relatively to ζ. These results are covered more profoundly in Paper 3, (Fig. 4 of Paper 3, for example). Compared with the ζ model, the ζa is rather peculiar, because some cation atoms seem not to form strong covalent bonds. Rather, the 4, 4', 9 and 9' atoms in Fig. 30a seem to "float" at the surface. As the density of state curves did not reveal anything drastic upon the In adsorption, it was assumed that the strong stabilization of ζa might have an electrostatic origin. Therefore, in order to elucidate the mechanisms behind the stability of the ζa, the atomic structure was studied in more detail by the means of Madelung energy calculations by exploiting the equation (7). It was further found that the metallic-nature of the bonds increases ionicity, which in turn decreases the Madelung energy and partly explains the found drastic stability.

Even though many previous experiments suggest the presence of the ζa structure on group III-rich III-V(100) surfaces and on GaAs(100)*c*(8×2)(4×2)-In,[53,54,60] careful STM measurements were performed also in Paper 3 to justifiably support the calculated results. By comparing the calculated and measured filled-state STM images, several considered In-induced (4×2) atomic structures can be ruled out, notably the previously proposed β-like and ζ structures. The measured filled state image shown in Fig. 32a is characterized by white rows with 4× of separation. According to calculations, these rows originate from the indium monomer rows (atomic sites 9 and 9' in Fig. 30a). Moreover, the three-fold coordinated arsenic atoms at the atomic sites 3 and 3' generate the faint gray protrusions that are visible especially in the measured filled state images of Ref. 216. According to calculations, the separation

between the ζa and ζb, which is a mixture of ζ and ζa, is not possible by filled state STM-measurements (Fig. 32 d and e). However, a clear difference is obviously seen in the empty state image (Fig. 32 g and h) where the calculated image of ζa is characterized by gray protrusions with ×2 separation between the bright white rows. These corrugations are clearly seen in the experimental empty state STM image in Fig. 32b and are explained by the top surface In atom at atomic site 4' in Fig. 30a.

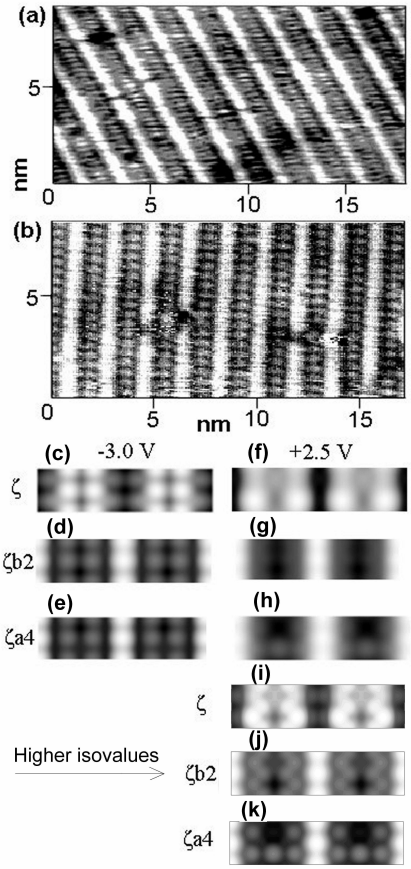

Figure 32. *(a) Measured filled-state (V=3.05 V) STM image of the GaAs(100)c(8×2)-In surface. (b) Measured empty-state (V=2.54 V) image the GaAs(100)c(8×2)-In surface. (c) - (e) Calculated filled-state STM images (3.00 V) for the ζ, ζb2, and ζa4 models. Charge density isovalue is $4.5 \cdot 10^{-5}$ electrons per $Å^3$. (f) - (h) Calculated empty-state STM images (2.50 V) for the ζ, ζb2, and ζa4 models. Charge density isovalue is $4.5 \cdot 10^{-5}$ electrons per $Å^3$. (i) – (k) Calculated empty-state STM images (2.50 V) for the ζ, ζb2, and ζa4 models. Charge density isovalue is $2.5 \cdot 10^{-3}$ electrons per $Å^3$*

3.4 Discovery of new structures: Crystalline oxidized III-V surfaces (Paper 4)

In Paper 4, totally new structures were discovered: crystalline oxidized III-V surface layers. These thin films are novel, because earlier the oxidized III-V surfaces have been found to be amorphous. These oxide layers can have a significant fundamental and practical impact on the understanding of III-V oxide formation as well as the engineering of III-V substrate surface prior to the dielectric deposition in high quality device applications. In particular, the well-defined crystalline oxidized surfaces provide a new platform for studying the challenging properties of oxidized III-V compound semiconductor materials and offer a novel pathway for producing insulator interfaces with superior quality for the next-generation devices.

The III-V materials considered in Paper 4 were InAs(100), GaAs(100)-In, InSb(100) and InP(100). All substrates were cleaned by Ar-ion sputtering and UHV-annealing cycles, which resulted in a well-defined group III-rich *c*(8×2)/(4×2) reconstruction for InAs, InSb and GaAs substrate and (2×4) for InP. The GaAs(100)-In surface was prepared by depositing approximately 1-2 ML of indium (Paper 3). Next, the freshly prepared surfaces were thermally oxidized at the material dependent temperature ranges of 350 °C – 520 °C and by introducing molecular oxygen into the UHV chamber with O_2 partial pressure of 3-4×10^{-6} mbar. The oxidation times were varied from 5 min to 30 min.

The discovered family of crystalline oxidized surfaces includes InAs(100)*c*(4×2)-O, InAs(100)(3×1)-O, GaAs(100)(4×3)-InO, GaAs(100)*c*(4×2)-InO, InSb(100)(1×2)-O, InSb(100)(3×1)-O and InP(100)(2×3)-O. An example of the obtained LEED image from the well the defined InAs(100)*c*(4×2)-O surface is given in Fig. 33a together with measured empty-state (2.4 V) STM image (Fig. 33b).

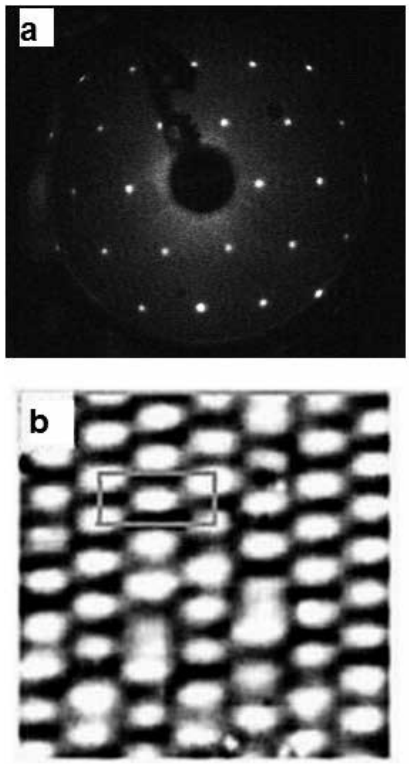

Figure 33. *(a) LEED image from reconstructed InAs(100)c(4×2)-O surface. (b) Measured empty-state (2.40 eV) STM-image from the same surface.*

The STS and SRPES analysis conducted for these surfaces revealed that the structures are semiconducting without defect states in the semiconductor band gap. Rather, the surface band gap appears to be widened in comparison with the clean III-V surface and bulk according to STS. In general, the defect-rich surface is usually associated with band bending and finite density of states at the Fermi-level, which are strong indications of FL-pinning phenomena. Indeed, such indicators are clearly seen in the VB-spectra from the amorphous air-oxidized InAs(100)*c*(8×2) reference sample in Fig. 34a which shows finite PES intensity around the FL. By comparison, the reconstructed InAs(100)-O surface lacks of such emission and the surface showed no band bending either, as conducted by comparing the As3d and In4d core-level binding energies. In addition, the valence band edge was found to lie 1.0 – 1.4 eV higher for

example in the case of InAs(100)(3×1)-O, compared to clean InAs(100)*c*(8×2) reconstruction as deduced by SRPES valence band difference spectrum. This result is illustrated in Fig. 34b.

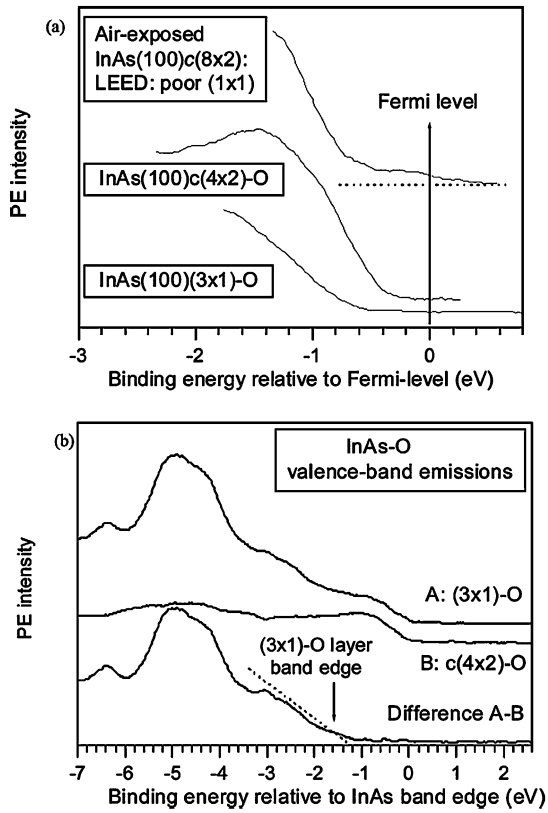

Figure 34. *(a) Photoemission from the InAs(100)(3×1)-O and c(4×2)-O layers as well as from the amorphous oxidized InAs(100) surface. (b) Difference spectrum between the (3×1)-O and c(4×2)-O.*

Extensive *ab initio* calculations were also employed in Paper 4 for elucidating the reconstruction mechanisms in the oxidized III-Vs. The initial clean III-V surface in most of the substrates has the *c*(8×2) symmetry with ζ and/or ζa atomic structure. Therefore, the one O adsorption was studied utilizing these atomic structures by determining the most favorable O atomic sites for the oxygen to occupy. The calculated results indicate that the stable O adsorption site locates in the second layer where electronegative oxygen bonds to

electropositive indium atom. The relaxed atomic structure of one O adsorption is illustrated in Fig. 35a. Furthermore, when the oxygen occupies two most stable adsorption sites and two second stable sites in InAs(100), the relaxed structure starts to show radical changes in the unit cell symmetry (Fig. 35b). Simulated STM images from the atomic model in Fig. 35b are quite consistent with the measured empty and filled STM images taken from InAs(100)*c*(4×2) as can be seen in Fig. 1 of Paper 4. For the GaAs(100)-In surface, the calculated STM image from the atomic model where oxygen occupies the most stable equivalent adsorption sites in the (4×2) unit cell (Fig. 35d) reproduce the measured STM images well. Within this model, it is energetically favorable for the surface to keep the one adsorption sites empty along the [011] direction due to the structural strain induced by the O-adsorption. Thus, the (4×3) symmetry is formed with the lowest oxygen coverage. Figure 35c shows a tentative atomic model for the InAs(100)(3×1)-O reconstruction, which is characterized by a zincblende –type bonding between the oxygen and the substrate In atoms.

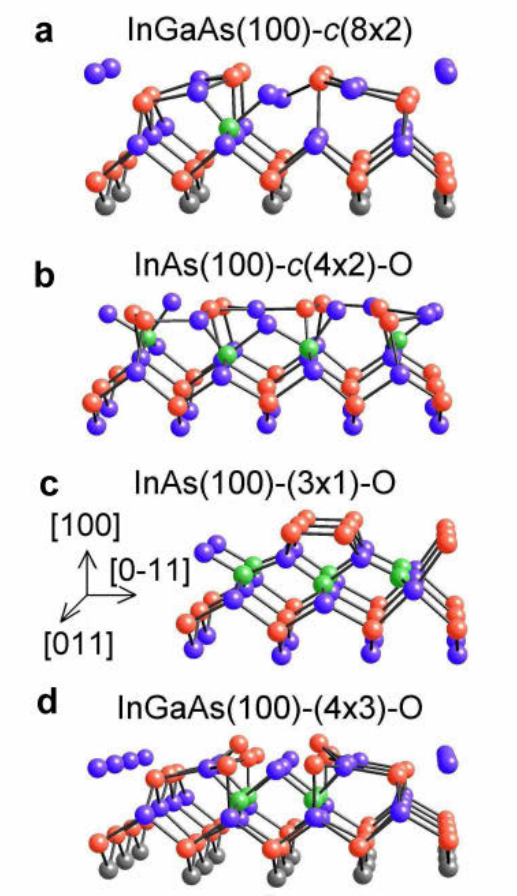

Figure 35. *(a) ζa structure of InGaAs(100) surface [(4 × 2) unit cell] with an oxygen atom in a remarkably stable adsorption position (2 MLs of In). (b) Most stable c(8×2) model (InAs; 0.5 MLs of O). (c) Model candidate for (3×1) InAs(100) structure (1ML of O). (d) InGaAs(100)(4×3)-O structure (0.33 MLs of O). The O, In, Ga, and As atoms are shown by green, blue, gray, and red atoms, respectively.*

It is noted that the above mentioned atomic models are tentative. There is still much research to be done in order to obtain the most probable atomic structures for the oxygen induced reconstructions. The main difficulty in calculations for example is the vast configurational space and the increasing energy differences as a function of oxygen coverage. In other words, when the O concentration is increased in the slab calculations, the surface energy is

gradually decreased. This is however very reasonable since the III-V materials are easily oxidized. According to XPS measurements, the (3×1) reconstruction contains approximately 1.5 times the amount of oxygen than the *c*(4×2) counterpart. Moreover, the (3×1) reconstruction seems to contain As-oxides, which generate a large binding energy core-level shift as seen in high resolution As3d SRPES spectra. Thus, the atomic model proposed in Paper 4 for (3×1) reconstruction needs revision in the future.

3.5 Synthesis and characterization of new monocrystalline oxide/III-V system: Layered SnO thin film on InAs(100) surface (Paper 5)

The work presented in Paper 5 is related to the investigations of the Sn-covered III-V surfaces. In Paper 2, it was found that the presence of Sn significantly changes the oxygen reaction of the III-V surfaces. During various oxidation cycles of the Sn-covered III-V surfaces, a surprising observation was made: a proper oxidation of the Sn-covered InAs(100) substrate led to the synthesis of a crystalline SnO_x thin film. In fact, this result was an impulse for starting the systematic oxidation tests of pure InAs surfaces, which led to the results presented in Paper 4.

Paper 5 deals with the synthesis and characterization of a new oxide/semiconductor junction: the crystalline SnO_x thin film on the III-V(100) substrate. The characterization of the SnO_x/InAs junction by LEED, STM/STS, and SRPES reveals that the film has an interesting layered (or two-dimensional) SnO crystal structure which consists of $Sn_{1/2}$−O−$Sn_{1/2}$ sheets with van der Waals gaps along the [001] direction. SnO and SnO_x ($1< x \leq 2$) films and nanostructures are potential materials for various nanotechnology components such as chemical sensor, thin-film-transistor, and optical coating applications.[217-221] However, the challenging preparation of smooth and well-defined SnO films and SnO_x surfaces has hindered the atomic scale research

and development of the SnO properties and the SnO_x surface characteristics relevant to the chemical sensor operation for example. The STM and STS results, presented in Paper 5 for the SnO thin film, elucidate these issues.

The sample preparation procedure included the fabrication of Sn-induced (1×2)/(1×4) starting surface (Paper 1) followed by a delicate thermal oxidation (Paper 4). The resulted LEED and large-scale STM images demonstrated the formation of crystalline SnO_x islands as seen in Fig. 36a-c. Furthermore, the similar surface was possible to produce by a careful annealing of the air-oxidized InAs(100)(1×2)/(1×4)-Sn surface. The SnO_x film surface partially exhibited the (3×3) reconstruction and the SnO_x layer thickness was found to be even 2.5 nm, according to STM line-profiles. The SnO_x island height or step was systematically 0.49±0.02 nm, which agrees well with the SnO sheet thickness. It is anticipated that the extra tin at the (1×2)/(1×4) structure may have a special role for the formation of thick SnO_x islands. As described in Paper 1, the Sn adsorbate stabilizes the (1×2)/(1×4) reconstruction only up to 0.5 MLs, and the extra Sn forms 3-dimensional clusters. 0.5 MLs of Sn is insufficient amount to produce such thick islands seen in Fig. 36 and therefore the only sources of extra Sn are the Sn-clusters.

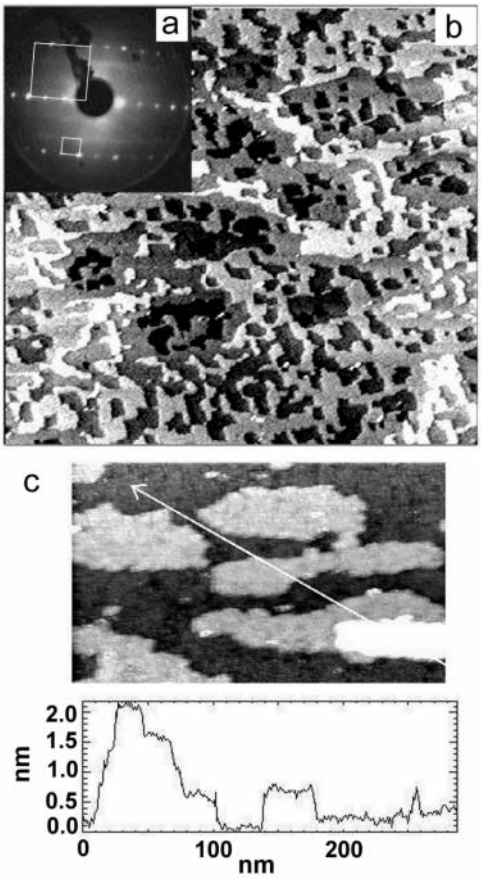

Figure 36. *(a) LEED pattern from the SnO_x/InAs surface showing (3×3) symmetry. (b) Filled-state (2.40V) large-scale STM image (650 nm×600 nm) from the SnO_x film. (c) Contour-line along the white arrow showing the two-dimensional SnO_x island height.*

The SRPES measurements of Paper 5 support the formation of SnO showing large positive binding energy shifts for the Sn4d core-level compared with the (1×2) surface as seen in Fig. 37. Furthermore, extra components for In4d spectrum are also produced upon the oxidation, while As3d showing relatively small changes (As-oxides are not present at the surface). It is therefore suggested that the SnO/InAs(100) interface contains an epitaxial $SnIn_yO_z$ layer below the SnO structure. The measured O1s bulk- and surface-sensitive spectra and the related core-level shifts also support the presence of SnO and buried $SnIn_yO_z$.

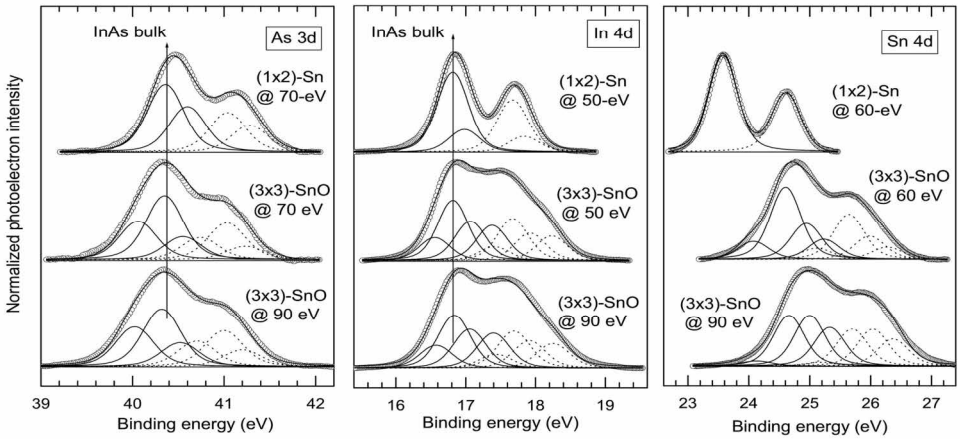

Figure 37. *As 3d, In 4d, and Sn 4d core-level spectra, measured from the SnO_x/InAs surface and the starting InAs(100)(1×2)-Sn surface, and the corresponding fittings. Emissions from SnO_x/InAs were measured with two different photon energies: the bottom spectra are more surface sensitive than the middle spectra.*

Atomic scale STM images in Fig. 38a and b from the InAs(100)(3×3)SnO_x surface indicates that the surface is composed of linear rows along the [011] direction separated by 3 times the lattice constant of InAs. A preliminary atomic model for such feature is presented in the Paper and in Fig. 38c. This model is based on the former knowledge of the SnO structure and our experimental results.

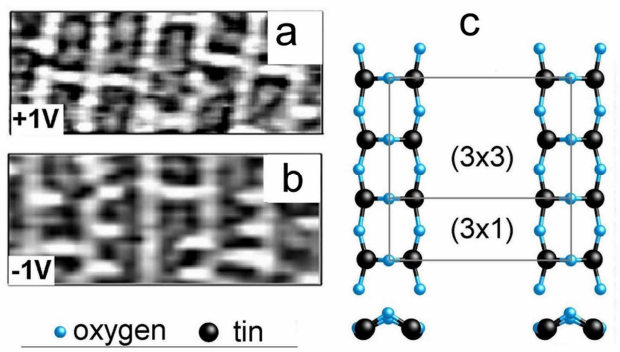

Figure 38. *(a) High-resolution empty-state (1.00 V) STM image (8 nm×3 nm) from the SnO_x film. (b) High-resolution filled-state (1.00 V) STM image (about 7 nm × 3 nm) SnO_x/InAs. (c) Tentative atomic model for the topmost surface of SnO_x.*

In Paper 5, the effects of Sn adsorbate (≤1ML) on the SnO properties was also investigated. In particular, it was found that the small amount of Sn significantly modifies the SnO surface making it metallic. Concomitantly, vacancy-type defects are formed, which agrees with the previous calculations which show that the oxygen vacancies are possible.[222] It is important to note that all these changes occur without any post heating (Sn was deposited on SnO kept at room temperature). The observations of Paper 5 support the previous macroscopic results indicating that adsorbate-induced defects play a key role in chemical sensors.[222]

3.6 Atomic and electronic structure of oxidized InSb(100)(1×2)-O surface (Paper 6)

The previous results from the well-defined oxide layers on III-V substrates (Paper 4) indicate that the oxidation of III-V is not necessarily harmful and the defect formation can be suppressed by the controlled oxidation of the surface. In Paper 6, this important discovery is utilized for elucidating the atomic and

electronic properties of the oxidized III-V surface and to shed light on the origin of the previously found beneficial and detrimental effects of the III-V oxidation considering the device performance. Complementary experimental techniques and *ab initio* calculations were exploited in order to propose a justified atomic structure of the crystalline InSb(100)(1×2)-O surface for further detailed electronic structure analysis. Notably, it was found that the determined atomic and electronic structures of oxidized InSb(100) unveil some peculiar properties that are unusual for the III-V reconstructions in general and which have been previously ignored when considering the oxidization of the III-V surfaces.

As mentioned above, the thermal oxidation of InSb(100)*c*(8×2) can produce two different oxygen induced reconstructions; namely the (3×1) and the (1×2) reconstructions. The LEED pattern from (1×2) surface, shown in Fig. 39a demonstrates the crystalline character of the oxidized surface, which is further supported by the large-scale STM image (Fig. 39b) showing a smooth two-dimensional terrace/step structure. The zoomed STM image (inset of Fig. 39b) shows a row structure causing the ×2 periodicity along the [011] direction. It was found by STS (Fig. 39c) and valence-band PES measurements (Fig. 39d) that the well-ordered InSb(100)(1×2)-O layers are semiconducting. The derivative STS spectrum, calibrated by measuring the known InSb(100)*c*(8×2) surface, shows (Fig. 39c) that the energy-band gap of the InSb(100)(1×2)-O layer is at least 0.55 eV.

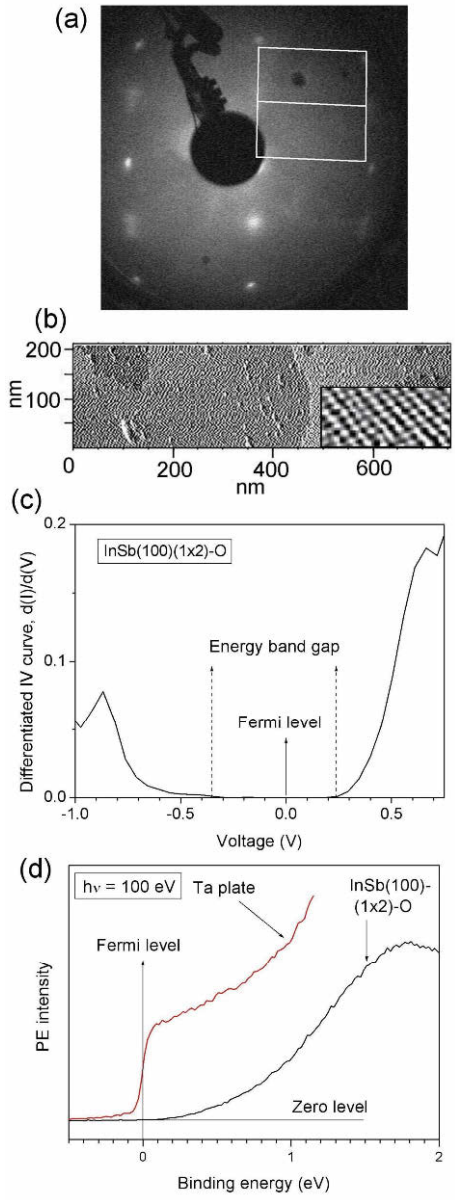

Figure 39. *(a) LEED pattern from the InSb(100)(1×2)-O surface: white square marks the lattice of the (1×1) bulk plane, and white rectangle is the surface lattice. (b) Large-scale STM image from the InSb(100)(1×2)-O taken with 1.67 V and 0.05 nA; the inset: zoomed STM showing a characteristic row structure of the InSb(100)(1×2)-O surface. (c) Differentiated STS curve showing a band gap for the InSb(100)(1×2)-O. (d) Measured valence-band photoemission from the InSb(100)(1×2)-O and a Ta plate with electric connection to the substrate.*

The extensive *ab initio* calculations, done in Paper 6 relied on pure trial and error procedure, for the atomic structure determination, as well as *ab initio* molecular dynamics simulations (simulated annealing). The basic assumption in the calculations was that the (1×2) periodicity is characterized by surface dimers. It was found that at the 0.5 ML of oxygen concentration, the oxygen tends to occupy the Sb substitutional atomic site in the second layer and the dimer composition is In-Sb. This structure revealed the lowest surface free energy compared with any other model, albeit the found structure was metallic. Next, when more oxygen (1 ML) was added, an overwhelming stability of the surface dimer interstitial site was discovered for O occupation. This structure is illustrated in Fig. 40. The characteristic feature for this model is that the interstitial oxygen protrudes downwards making bonds with the third layer In-atoms in addition to the dimer Sb and In atoms. Furthermore, this atomic model was found to be also semiconducting, in accordance with STS and VB-PES measurements.

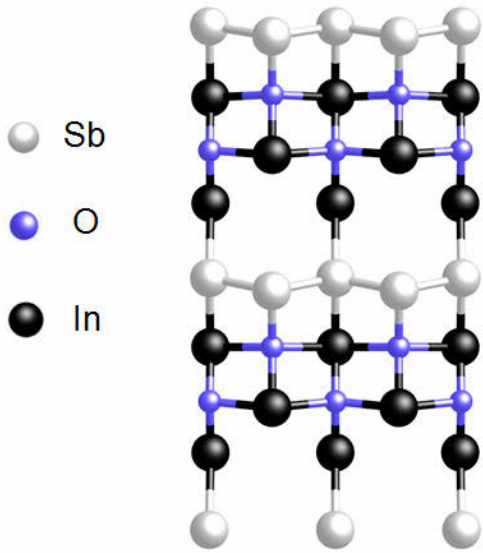

Figure 40. *Most stable InSb(100)(1×2)-O model with 1 ML of oxygen concentration.*

At first sight, the semiconducting nature of the found atomic model in Fig. 40 is rather confusing and not so easily understood. By applying the GEC heuristics, described in Chapter 1.2 [equation (6)], and assuming that the oxygen atom behaves as an acceptor for the electrons at the surface (due to high electronegativity compared with In and Sb), it was calculated that there are two or four extra electrons in the slab, depending whether or not the Sb dangling bond is occupied. However, the electron localization function (ELF) analysis conducted for this structure surprisingly suggests that the In dangling bond becomes occupied upon the oxidation as it is evident from Fig. 41b. This interesting finding is further supported by the relative ELF plot along the dimer plane where the -2 electron ELF data was subtracted from the original ELF data. According to the subtraction-figure (Paper 6), the major changes in ELF probability density by removing two electrons from the slab occur only in the vicinity of the dimer indium atom.

The interesting finding of group III DB occupation was further investigated by band structure calculations employing both local-density approximation and Heyd-Scuseria-Ernzerhof (HSE06) hybrid exchange-correlation functionals.[196] The calculated LDA band structure along the high symmetry directions of the surface Brillouin zone (denoted J and J' and K) is shown in Fig. 41a. The top surface indium –related weight for the band structure is illustrated by red circles and the highest weight is found at the band below the valence band maximum (VBM) near the J' high symmetry point. The band decomposed charge density of this indium related band also shows a substantial charge density around the top-surface indium atom. According to this finding, the oxidation of InSb(100) can lower the In dangling bond energy below the VBM and the dangling bond become occupied contradicting the generalized ECM heuristics of the adsorbate-induced III-V surface reconstructions as well as the general idea of the group III dangling bond state as the potential "near CBM" defect state in the oxidized III-V surfaces.

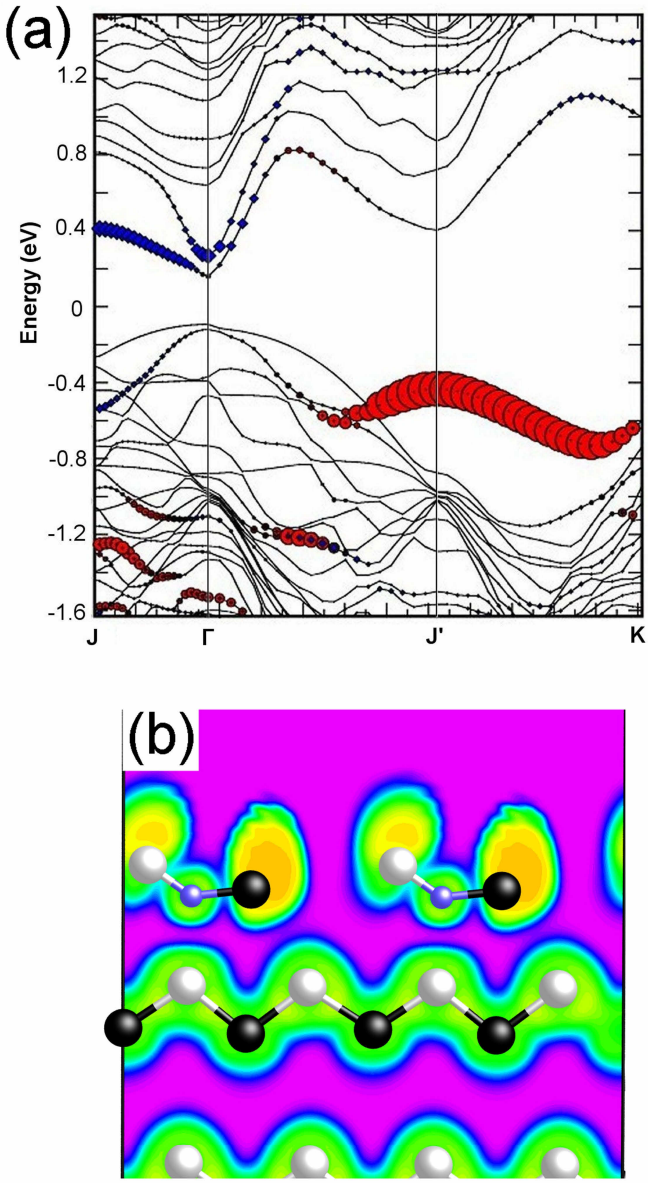

Figure 41. *(a) Calculated LDA band structure plot along the high symmetry directions of the surface Brillouin zone for the structure in Fig. 40. The top surface In-related weight for the band structure is illustrated by red circles and the top surface Sb-related by blue rectangles (b) Electron-localization-function image from the same structure.*

As the exact O-concentration was unknown for the InSb(100)(1×2)-O structure, more calculations were done where the most stable atomic sites for further O-occupation were investigated. Oxygen concentration was raised even up to 4.5 MLs. However, the uncertainty of the atomic structure is gradually increased as more oxygen is added due to the very large configurational space, even though the unit cell is relatively small. Therefore, simulated annealing calculations were done in order to find the global minimum for the previously calculated structures. Calculations were done by using a larger (4×2) slab. The annealing procedure was done by raising the temperature from 300 K to 1000 K in 3 ps, keeping the 1000 K temperature for another 3 ps and eventually lowering the temperature back to 300 K in 3 ps. The subsequent DFT calculations done for the annealed structures revealed that up to 2 MLs, the simulated annealing procedure produced almost the same atomic structure as the initial guessed geometry, suggesting that the found structures are indeed the low energy structures. The SRPES core-level shifts as well as high-resolution STM measurements also support the presence of the found stable structures as it is shown in Paper 6.

The simulated annealing structure optimization calculations, performed for the models with 2.5 ML to 4.5 ML of O concentration, produced structures with lower symmetry, i.e. more disordered type atomic configuration in comparison with the models with lower oxygen concentration. These “disordered” models were substantially more stable than the ordered counterparts with the same O concentration. Indeed, the symmetry is also lowered in experiments when more oxygen is added. This is seen in the STM images taken from the samples with higher oxidation time (Fig. 42a). At these samples, small clusters are produced on the surface, with not so well defined symmetry. Moreover, the STS curves taken from these clusters indicate that the band gap is drastically smaller compared with the reconstructed case and STS characteristic is even metallic for larger clusters (Fig. 42b). Thus, both the calculations and the STM/STS measurements suggest that there is a very narrow parameter window in which the good quality ordered oxide layer with no defect states in the band gap is

possible to produce. Namely, the O-concentration at the surface is crucial, which is solely controlled by the O_2 partial pressure and by the sample temperature. This assumption was put into a test by fabricating MOSCAPs (Fig. 42c) with different amount of oxygen in the intermediate layer prior the actual gate dielectric deposition. Qualitative CV-curve analysis shown in Fig. 42d and e, demonstrate that the quality of the interface including the pre-oxidized InSb(100)(1×2)-O (Fig. 42d) is better than that of the over-oxidized InSb interface (Fig. 42e) because the capacitance modulation is clearly stronger (i.e., deeper C dip) for the former MOSCAP.

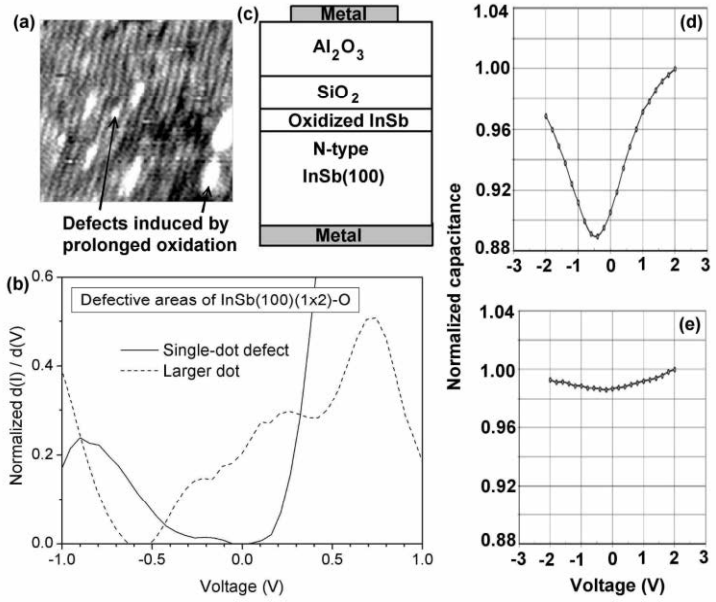

Figure 42. *(a) STM image of the InSb(100)(1×2)-O surface containing defects induced by prolonged oxidation. (b) STS curves from different defective areas. (c) Schematic MOSCAP structure of the samples characterized by CV measurements. (d) 10-kHz CV curve from the MOSCAP of which interface included the pre-oxidized InSb(100)(1×2)-O surface. (e) 10-kHz CV curve from the MOSCAP of which interface included an over-oxidized InSb(100) surface*.

3.7 From surface reconstructions to device tests

In order to investigate the impact of the well-defined crystalline oxide layers on the device-applications, III-V MOSCAP and/or MOSFET structures should be fabricated. Because our group did not have any previous experience to perform a device test for the samples, prepared in our UHV system, there were many crucial issues to be solved in the beginning. The first major question was how to protect the synthesized films and interfaces against the strong air-exposure attack during the sample transfer from UHV to another instrument for further device processing and/or characterization. In other words, how to make sure that the interface layers, to be tested in a real component, preserve their properties in air. The films should be protected by sufficiently thick and good quality insulator layers which act as a gate-insulator for the MOS-structures. The best method for controllably fabricating uniform, conformal and good quality insulator layers is the ALD. For the found thin-films, it would be very desirable that the ALD growth starts without the breaking of the UHV-environment, thus protecting the sample towards the hostile ambient air environment.

Because the University of Turku system did not include the UHV-compatible ALD, the first solution tried in this Thesis was to deposit a thin (2−5 nm) Al_2O_3 cap layers on top of the discovered SnO and crystalline oxidized III-V layers using an electron-beam (e-beam) evaporator which was available in the laboratory. The e-beam evaporator included a small crucible, which was loaded with commercially available Al_2O_3 crystals. This crucible was heated by electron bombardment to the Al_2O_3 evaporation temperature and the resulted Al_2O_3 flux was monitored by QCM. The dielectric growth was performed under O_2 environment. After the Al_2O_3 insulator growth, the samples were transferred via air to a separate commercial ALD system (Beneq) where the top and better quality Al_2O_3 film was grown. The samples were then sent to the Optoelectronics Research Centre, Tampere University of Technology (ORC,

TUT) where the MOSCAP process was made by our collaborators. The schematic structure of these MOSCAP samples is shown in Figure 43a.

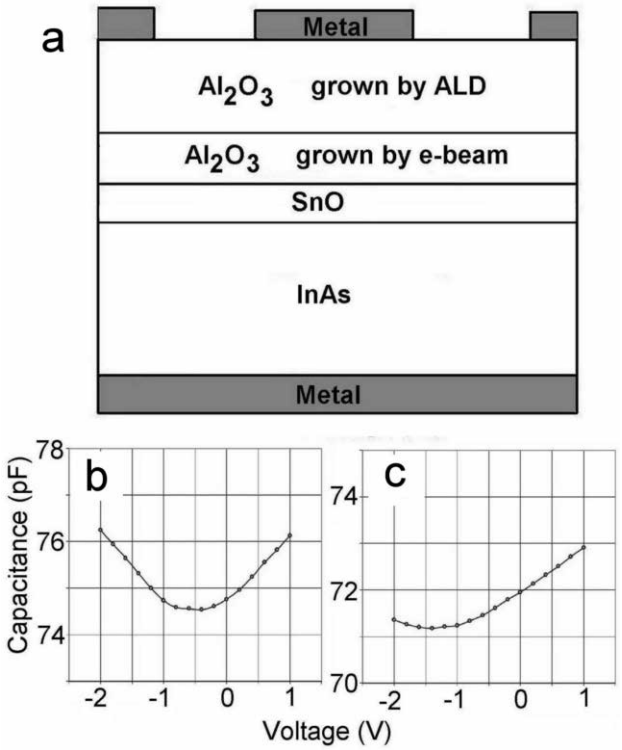

Figure 43. *(a) Scheme of MOS capacitors with the SnO interface layer; layer thicknesses are not relatively correct. (b) CV curve (10 kHz) from MOS capacitors with the SnO interface layer. (c) CV curve (10 kHz) from MOS capacitors without the SnO interface layer.*

Figures 43b and 43c summarize the characterization of these MOSCAP samples. The CV curves, measured at 10 kHz, indicate that the quality of the Al_2O_3/SnO/InAs (Fig. 43b) oxide-semiconductor interface is better than that of the Al_2O_3/InAs (Fig. 43c) sample because no clear inversion occurs at the latter. The CV modulation is clearly stronger for the capacitor including the SnO thin film. The capacitance dip is also shifted to negative voltages for the Al_2O_3/InAs sample, supporting the Fermi level pinning in the conduction band due to the

interface states. These results indicate that the crystalline nature of the SnO/InAs interface improved the interface at least to some extent. Similar conclusions were obtained also from the CV characterization of the samples containing the InAs(100)*c*(4×2)-O InAs(100)(3×1)-O interface layers instead of the SnO one. However, the dielectric growth of the first Al_2O_3 layer by e-beam was far from optimal. Silicon (Si) capping was also tested, instead of the e-beam Al_2O_3 layer. The idea was that an amorphous Si film (about 2 nm thick) is oxidized in air and the resulted surface is SiO_2. Then, the Al_2O_3 was grown by ALD on top of the oxidized Si. The obtained CV results from these Si-capped samples supported the above conclusion that the crystalline oxide intermediate layer can improve the oxide/III-V device interfaces. Also the first MOSCAP results revealed the importance of controlling the amount of oxygen or the extent of the pre-oxidation, as it was shown in Figure 42 and Paper 6 for the InSb(100) substrate.

After the first device tests, it was decided to build a home-made ALD chamber which is directly connected to the UHV chamber. This kind of arrangement allows the controlled growth of the good quality insulator layers without the breaking of the vacuum conditions. I was responsible for the design and the instrumentation. Rather simple design of the UHV-ALD was implemented for the ALD reactor. Figure 44 shows a schematic diagram of the instrumented ALD, which consists of two separate six-way-cross stainless-steel chambers. The other chamber (ALD-reactor) hosts the ALD manipulator with Omicron sample holder compatible manipulator head and a resistive heating filament. Moreover, the ALD-reactor was equipped with two manually controlled UHV leak-valves for metal precursor and water exposures. The other chamber was equipped with mass-spectrometer for the detection of the reaction gases and byproducts of the ALD growth. In addition, this chamber also hosted a cold-cathode-gauge for the pressure measurement and control. Whole system can be pumped down by turbo-molecular and rotary-vane pumps. Heating-tapes were also installed, and after the pumping and baking, the achieved pressure was usually in the 10^{-9} mbar range.

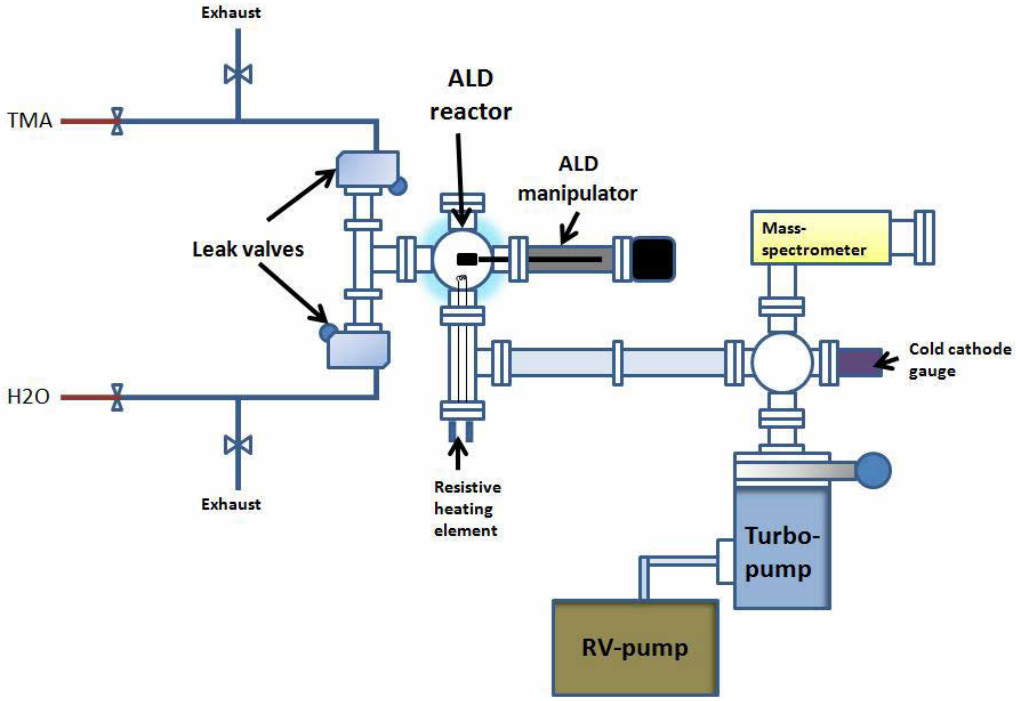

Figure 44. *Layout of the home-made in-situ ALD chamber connected to the UHV system.*

The atomic-layer-deposition of the dielectric material (Al_2O_3) was conducted by annealing the sample to desired temperature, monitored by pyrometer, and opening the trimethylaluminium (TMA) and H_2O leak-valves in cycles. The pressure ranges for the ALD-deposition was varied between 10^{-6} mbar and 10^{-4} mbar. The deposition time is dependent on the partial pressure of the reactant (smaller the pressure, longer the deposition time). Growth parameters were optimized by growing Al_2O_3 on top of the cleaned Si(100) surface with several different growth temperatures and varying the exposure time. Atomic-force-microscope (AFM) images from the grown Al_2O_3 layers in Fig. 45 demonstrate the observed difference between the samples with different growth parameters. Clearly, the surface in Fig. 45a is drastically smoother than the surface in Fig. 45b.

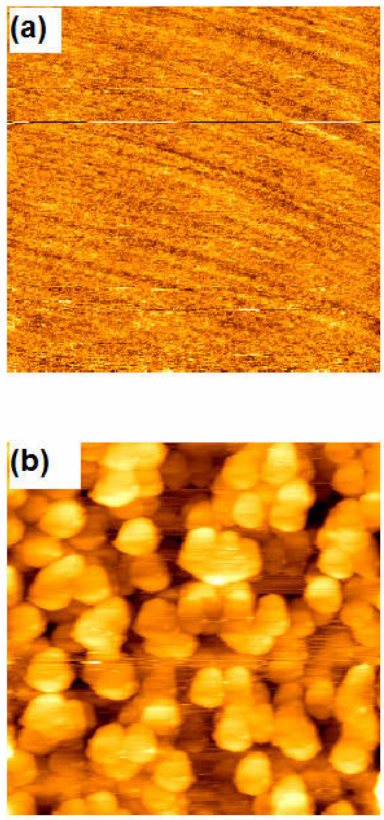

Figure 45. *Atomic-force-microscopy images from two different ALD grown Al_2O_3 layer: (a) The sample with proper growth parameters. Sample roughness was measured to be as low as 0.84 nm within the 50 μm scanned area. (b) The sample with not optimal growth parameters. Sample roughness was 18.88 nm within the 50 μm area.*

Moreover, the ALD growth was tested on MBE grown GaInAs(100) substrate. About 4-nm thick Al_2O_3 cap layers were grown on GaInAs substrates and the PL intensities were then characterized at ORC, TUT. The PL-measurements conducted for the samples with and without the ALD Al_2O_3 showed the superior quality of the interface for the ALD-grown sample, compared with the samples with no ALD, as seen in Fig. 46. The PL intensity of the ALD-capped sample is more than 10 times than of the reference sample without the ALD-cap, indicating that the GaInAs surface contains a tenth of interface defects than the

reference sample. Moreover, the recorded PL-intensity and FWHM maps from the ALD-grown sample indicate that the films are very uniform through the whole sample as it is shown in Fig. 47. The above results suggest that the instrumented ALD-reactor works as desired and good-quality smooth Al_2O_3 insulator layers can be grown.

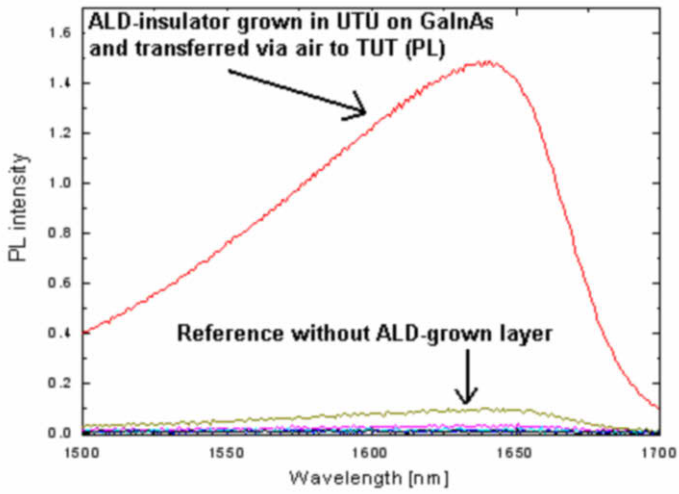

Figure 46. *PL test to clarify the effect of the in-situ ALD cap on the $Ga_{0.47}In_{0.53}As$ interface quality.*

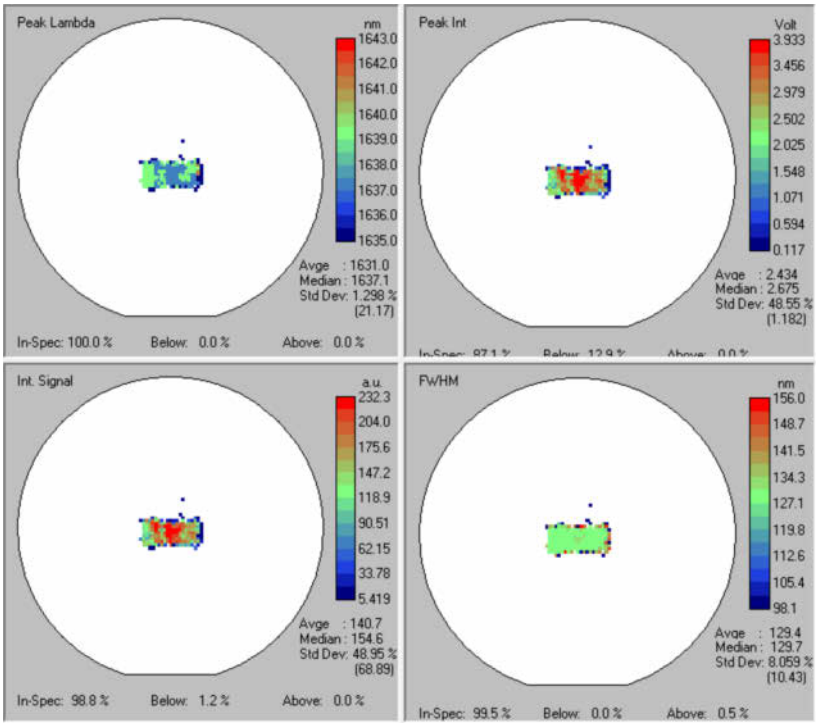

Figure 47. *Uniformity of the ALD-capped GaInAs sample. The PL emission wave-length (upper left figure), PL intensity (upper right figure) and FWHM maps shows that the grown ALD films are very uniform. The shorter edges are shadowed by the sample holder clips.*

The MOSCAPs were processed on the above described GaInAs samples by using the home-made ALD and the calibrated Al_2O_3 growth parameters. However, the MOSCAPs did not work properly because the grown Al_2O_3 layers were too thin. A new series of *in-situ* ALD-capped samples were fabricated on the GaAs(100) substrate. At the time of writing of this thesis, the MOSCAP process is under way, but the PL results are already presented in Fig. 48. The reference sample consists of the 3 nm thick Al_2O_3 cap deposited on the clean GaAs(100) surface with the combined (4×2)+(6×6) reconstruction. Two other samples were prepared as follows. The GaAs(100)(4×2)-In surfaces, described in Paper 3, were oxidized in the controlled way as described in Paper 4 to produce the crystalline oxidized surface layers and 3 nm thick Al_2O_3 caps were grown finally by the home-made ALD. One sample contained the *c*(4×2)-O

interface layer, while the other GaAs(100)(4×2)-In surface was oxidized so that the sharp (1×1) spots dominated the LEED pattern. The PL results in Fig. 48 demonstrate that the oxide/GaAs interface quality is best for the sample containing the *c*(4×2)-O structure and worst for the reference.

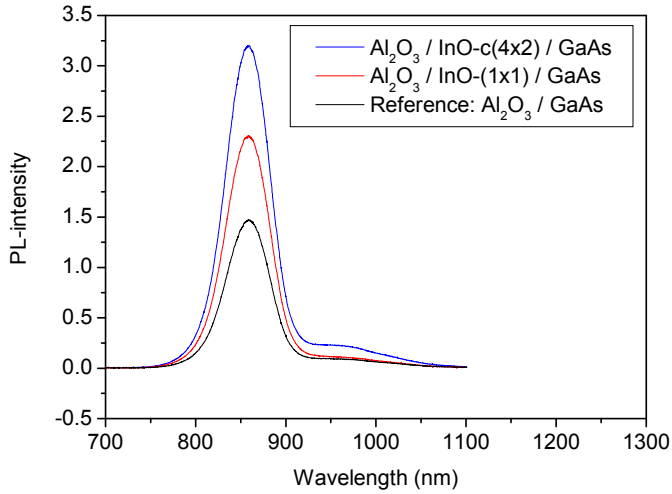

Figure 48. *PL intensities of surface engineered Al_2O_3/GaAs interfaces*.

The early device tests, described above, show clear evidence that the crystalline oxidized III-V surfaces can act as interface passivation layers and improve the crucial insulator-semiconductor interface in actual devices. Furthermore, these tests also support the basic research results (e.g. Paper 6) that too high oxidation starts to degrade the interface most likely due to the formation of amorphous oxide phases. It is thus anticipated that the commercially conceivable next-generation III-V MOSFET transistors will need a very delicate fabrication process, including the atomic-scale optimization of the interfaces. Such device fabrication methods will require the usage of UHV environment in certain steps of the IC-circuit production for instance. However, more research is needed in the near future for extracting the quantitative interface-state-density results from the MOSCAPs with crystalline oxide layers.

4 Concluding remarks

The main results of this thesis are summarized as follows:

(1) The atomic structures of the III-V(100)(1×2)-Sn surfaces, which have been previously found to improve the III-V device materials, are elucidated: The main building blocks of the surfaces was found to consists of Sn-III dimers, in contrast to Si and Ge induced structures on III-Vs, where the Si and Ge atoms tend to occupy the subsurface atomic sites. The results were obtained by combining *ab initio* calculations, STM and SRPES measurements.

(2) The GaAs- and InAs(100)(1×2)-Sn surfaces were found to catalyze the removal of III-V surfaces oxides that are formed in air exposure. This property might be very useful method to improve the device interfaces. Future device tests are needed to answer this question.

(3) The atomic structure of the GaAs(100)*c*(8×2)/(4×2)-In surface, which has been previously found to be a useful template for the improved device materials, was solved. For the first time, the so-called ζa atomic structure was found to be energetically the most favourable structure by *ab initio* calculations. The calculated results were supported by STM measurements.

(4) Totally new oxygen induced III-V surface structures were discovered. The produced crystalline oxidized III-V surface layers form a novel family of thin films because previously oxidized III-V surfaces have been found to be amorphous. The atomic and electronic structures of the discovered layers, namely the InAs(100)*c*(4×2)-O, InAs(100)(3×1)-O, and InSb(100)(1×2)-O and GaAs(100)(4×3)InO were elucidated. The

novel films were found to be semiconducting without the detrimental defect-states at the III-V semiconductor band gap.

(5) A new monocrystalline metal-oxide/III-V junction, namely the SnO_x/InAs, is synthesized and characterized. The SnO_x thin film was found to have an interesting two-dimensional SnO crystal structure. It was suggested that the formation of an epitaxial $SnIn_yO_z$ interface layer is the key for the synthesis of the SnO film. The properties of SnO, which have been previously remained unresolved largely due to the challenging synthesis of the SnO crystals, were elucidated.

(6) The well defined crystalline nature of the O-induced reconstructions was employed for elucidating the atomic and electronic properties of the InSb(100)(1×2)-O surface. It was found by *ab initio* calculations, that the oxygen incorporates Sb substitution sites and dimer interstitial sites which decrease the group III dangling bond energy below the valence band maximum. It was also demonstrated by calculations and experiments that very delicate surface oxidation is needed in order to avoid the detrimental amorphous oxide and the related defect state formation.

(7) The novel crystalline oxidized III-V layers and SnO films were transferred to the device tests in order to clarify the technological impact of the results from the basic research. To that end, the *in-situ* ALD reactor was build. The first MOSCAP and PL results show that the discovered crystalline oxidized III-V(100) structures are potential parts to solve the long-standing problem related to the manufacturing of commercial conceivable III-V MOSFETs.

References

[1] T. Ashley, L. Buckle, S. Datta, M. T. Emeny, D. G. Hayes, K. P. Hilton, R. Jefferies, T. Martin, T. J. Phillips, D. J. Wallis, P. J. Wilding, and R. Chau, Electronics Lett. **43**, 14 (2007).

[2] Compound Semiconductor: *InGaAs revolutionizes III-V MOSFETs*, April 2008, www.compoundsemiconductor.net

[3] Semiconductor Today: *Conference report on IEEE's International Electron Device Meeting 2009*. Vol. 5, Issue 1 (2010), www. semiconductor-today.com.

[4] Semiconductor Today: *Technical focus: Beyond silicon*. Vol. 5, Issue 1 (2010), www. semiconductor-today.com.

[5] Heike Riel (IBM Research): *Nanowire Tunnel FETs*, 2nd Berkeley Symposium on Energy Efficient Electronic Systems, November 3-4, 2011.

[6] J. A. del Alamo, R*eview: Nanometer-scale electronics with III-V compound semiconductors*, Nature **479**, 317 (2011).

[7] *Fundamentals of III-V Semiconductor MOSFETs*, edited by S. Oktyabrsky and P. D. Ye, Springer (2010).

[8] C. Kittel, *Introduction to Solid State Physics*, Wiley (1976).

[9] S.M. Sze, *Physics of Semiconductor Devices*, Wiley (2007).

[10] S. S. Li, *Semiconductor Physical Electronics*, Plenum Press, New York (1993).

[11] *Molecular Beam Epitaxy: Applications to Key Materials*, edited by Robin F. C. Farrow, Noyes Publications (1995).

[12] A. Zangwill, *Physics at Surfaces*, Cambridge University Press, 1988.

[13] *Handbook of Surface Science, Volume 1: Physical Structure*, edited by W. N. Unertl, Elsevier Science, 1996.

[14] H. Lüth, *Solid Surfaces, Interfaces and Thin Films*, Springer, 2001.

[15] F. Bechstedt, *Principles of Surface Physics*, Springer, 2003.

[16] N. Moll, A. Kley, E. Pehlke, and M. Scheffler, Phys. Rev. B **54**, 8844 (1996).

[17] N. Chetty, and R. M. Martin, Phys. Rev. B **44**, 5568 (1991).

[18] C. B. Duke, Chem. Rev. **96**, 1237 (1996).

[19] W. G. Schmidt, P. H. Hahn, F. Bechstedt, N. Esser, P. Vogt, A. Wange, and W. Richter, Phys. Rev. Lett. **90**, 126101 (2003).

[20] M. D. Pashley, Phys. Rev. B **40**, 10481 (1989).

[21] L. Zhang, E. G. Wang, Q. K. Xue, S. B. Zhang, and Z. Zhang, Phys. Rev. Lett. **97**, 126103 (2006).

[22] S. Yang, L. Zhang, H. Chen, E. Wang, and Z. Zhang, Phys. Rev. B **78**, 075305 (2008).

[23] W. A. Harrison, *Elecronic Structure and the Properties of Solids*, Freeman, San Francisco, 1980

[24] P.Laukkanen, M. P. J. Punkkinen, H.-P. Komsa, M. Ahola-Tuomi, K. Kokko, M. Kuzmin, J. Adell, J. Sadowski, R. E. Perälä, M. Ropo, T. T. Rantala, I. J. Väyrynen, M. Pessa, L. Vitos, J. Kollár, S. Mirbt, and B. Johansson, Phys. Rev. Lett. **100**, 086101 (2008).

[25] P. Laukkanen, M. P. J. Punkkinen, N. Räsänen, M. Ahola-Tuomi, J. Lång, J. Sadowski, J. Adell, J. Sadowski, R. E. Perälä, M. Ropo, K. Kokko, L. Vitos, B. Johansson, M. Pessa, and I. J. Väyrynen, Phys. Rev. B **81**, 035310 (2010).

[26] W. G. Schmidt, S. Mirbt, and F. Bechstedt, Phys. Rev. B **62**, 8087 (2000).

[27] J. E. Northrup, and S. Froyen, Phys. Rev. B **50**, 2015 (1994).

[28] W. G. Schmidt, Appl. Phys. A **75**, 88-99 (2002).

[29] M. D. Pashley, K. W. Haberern, W. Friday, J. M. Woodall, and P. D. Kirchner, Phys. Rev. Lett. **60**, 2176 (1988).

[30] D. K. Biegelsen, R. D. Bringans, J. E. Northrup, and L.-E. Swartz, Phys. Rev. B **41**, 5701 (1990).

[31] S. L. Skala, J. S. Hubacek, J. R. Tucker, J. W. Lyding, S. T. Chou, and K.-Y. Cheng, Phys. Rev. B **48**, 9138 (1993).

[32] C. W. Snyder, J. Sudijono, C.-H. Lam, M. D. Johnson, and B. G. Orr, Phys. Rev. B **50**, 18194 (1994).

[33] J. E. Northrup and S. Froyen, Phys. Rev. B **50**, R2015 (1994).

[34] T. Hashizume, Q.-K. Xue, J. Zhou, A. Ichimiya, and T. Sakurai, Phys. Rev. Lett. **73**, 2208 (1995).

[35] T. Hashizume, Q.-K. Xue, A. Ichimiya, and T. Sakurai, Phys. Rev. B **51**, 4200 (1995).

[36] H. Yamaguchi and Y. Horikoshi, Phys. Rev. B **51**, 9836 (1995).

[37] W. G. Schmidt and F. Bechstedt, Phys. Rev. B **54**, 16742 (1996).

[38] Y. Garreau, M. Sauvage-Simkin, N. Jedrecy, R. Pinchaux, and M. B. Veron, Phys. Rev. B **54**, 17638 (1996).

[39] A. Y. Cho, J. Appl. Phys. **42**, 2074 (1971).

[40] V. P. LaBella, H. Yang, D. W. Bullock, P. M. Thibado, P. Kratzer, and M. Scheffler, Phys. Rev. Lett. **83**, 2989 (1999).

[41] G. R. Bell, J. G. Belk, C. F. McConville, and T. S. Jones, Phys. Rev. B **59**, 2947 (1999).

[42] W. G. Schmidt, S. Mirbt, and F. Bechstedt, Phys. Rev. B **62**, 8087 (2000).

[43] A. Ohtake, J. Nakamura, S. Tsukamoto, N. Koguchi, and A. Natori, Phys. Rev. Lett. **89**, 206102 (2002).

[44] A. Ohtake and N. Koguchi, Appl. Phys. Lett. **83**, 5193 (2003).

[45] A. Ohtake, P. Kocán, K. Seino, W. G. Schmidt, and N. Koguchi, Phys. Rev. Lett. **93**, 266101 (2004).

[46] P. Laukkanen, M. Kuzmin, R. E. Perälä, M. Ahola, S. Mattila, I. J. Väyrynen, J. Sadowski, J. Konttinen, T. Jouhti, C. S. Peng, M. Saarinen, and M. Pessa, Phys. Rev. B **72**, 045321 (2005).

[47] A. Ohtake, Phys. Rev. B **74**, 165322 (2006).

[48] K. Seino, W. G. Schmidt, and A. Ohtake, Phys. Rev. B **73**, 035317 (2006).

[49] Q.-K. Xue, T. Hashizume, and T. Sakurai, Progr. Surf. Sci. **56**, 1 (1997).

[50] A. Ohtake, Surf. Sci. Rep. **63**, 295 (2008).

[51] S.-H. Lee, W. Moritz and M. Scheffler. Phys. Rev. Lett. **85**, 3890 (2000).

[52] H. Xu, Y. Y. Sun, Y. G. Li, Y. P. Feng, A. T. S. Wee, and A. C. H. Huan, Phys. Rev. B **70**, 081313 (2004).

[53] C. Kumpf, L. D. Marks, D. Ellis, D. Smilgies, E. Landemark, M. Nielsen, R. Feidenhans'l, J. Zegenhagen, O. Bunk, J. H. Zeysing, Y. Su, and R. L. Johnson, Phys. Rev. Lett. **86**, 3586 (2001).

[54] C. Kumpf, D. Smilgies, E. Landemark, M. Nielsen, R. Feidenhans'l, O. Bunk, J. H. Zeysing, Y. Su, R. L. Johnson, L. Cao, J. Zegenhagen, B. O. Fimland, L. D. Marks, and D. Ellis, Phys. Rev. B **64**, 075307 (2001).

[55] R. H. Miwa, R. Miotto and A. C. Ferraz, Surf. Sci. **542**, 101 (2003).

[56] D. Paget, Y. Garreau, M. Sauvage, P. Chiaradia, R. Pinchaux, and W. G. Schmidt, Phys. Rev. B **64**, 161305 (2001).

[57] P. De Padova, C. Quaresima, P. Perfetti, R. Larciprete, R. Brochier, C. Richter, V. Ilakovac, P. Bencok, C. Teodorescu, V. Y. Aristov, R. L. Johnson, and K. Hricovini, Surf. Sci. **482-485**, 587 (2001).

[58] A. Ohtake, S. Tsukamoto, M. Pristovsek, N. Koguchi, and M. Ozeki, Phys. Rev. B **65**, 233311 (2002).

[59] T.-L. Lee, C. Kumpf, A. Kazimirov, P. F. Lyman, G. Scherb, M. J. Bedzyk, M. Nielsen, R. Feidenhans'l, R. L. Johnson, B. O. Fimland, and J. Zegenhagen, Phys. Rev. B **66**, 235301 (2002).

[60] J. J. Kolodziej, B. Such, M. Szymonski, and F. Krok, Phys. Rev. Lett. **90**, 226101 (2003).

[61] P. Laukkanen, M.P.J. Punkkinen, M. Ahola-Tuomi, J. Lång, K. Schulte, A. Pietzsch, M. Kuzmin, J. Sadowski, J. Adell, R.E. Perälä, M. Ropo, K. Kokko, L. Vitos, B. Johansson, M. Pessa, and I.J. Väyrynen, J. Electr. Spectr. Rel. Phenom. **177**, 52 (2010).

[62] B. Z. Nosho, W. H. Weinberg, W. Barvosa-Carter, B. R. Bennett, B. V. Shanabrook, and L. J. Whitman, Appl. Phys. Lett. **74**, 1704 (1999).

[63] M. R. Pillai, S.-S. Kim, S. T. Ho, S. A. Barnett, J. Vac. Sci. Technol. B **18**(3), 1232 (1999).

[64] S. Tixier, M. Adamcyk, E. C. Young, J. H. Schmid, and T. Tiedje, J. Cryst. Growth **251**, 449 (2003).

[65] G. Feng, K. Oe, and M. Yoshimoto, J. Cryst. Growth, **301-302**, 121 (2007).

[66] T. Liu S. Chandril, A. J. Ptak, D. Korakakis, and T. H. Myers, J. Cryst. Growth **304**, 402 (2007).

[67] A. J. Ptak, R. France, C.-S. Jiang, and R. C. Reedy, J. Vac. Sci. Technol. B **26**, 1053 (2008).

[68] P. B. Joyce, T. J. Krzyzewski, G. R. Bell, B. A. Joyce, and T. S. Jones, Phys. Rev. B **58,** R15981 (1998).

[69] P. B. Joyce, T. J. Krzyzewski, G. R. Bell, T. S. Jones, S. Malik, D. Childs, and R. Murray, Phys. Rev. B **62,** 10891 (2000).

[70] Q. K. Xue, Y. Hasegawa, T. Ogino, H. Kiyma, and T. Sakurai, J. Vac. Sci. Technol. B **15**, 1270 (1997).

[71] E. C. Young, S. Tixier, and T. Tiedje, J. Cryst. Growth **279**, 316-320 (2005).

[72] S. Tixier, M. Adamcyk, E. C. Young, J. H. Schmid, and T. Tiedje, J. Cryst. Growth **251,** 449 (2003)

[73] X. Yang, M. J. Jurkovic, J. B. Heroux, and W. I. Wang, Appl. Phys. Lett. **75**, 178 (1999)

[74] M. Masnadi-Shirazi, D. A. Beaton, R. B. Lewis, X. Lu, and T. Tiedje, J. Cryst. Growth **338**, 80 (2012).

[75] M. P. J. Punkkinen, P. Laukkanen, H.-P. Komsa, M. Ahola-Tuomi, N. Räsänen, K. Kokko, M. Kuzmin, J. Adell, J. Sadowski, R. E. Perälä, M. Ropo, T. T. Rantala, I. J. Väyrynen, M. Pessa, L. Vitos, J. Kollár, S. Mirbt, and B. Johansson, Phys. Rev, B **78**, 195304 (2008).

[76] T. Anan, S. Sugou, and K. Nishi, Appl. Phys. Lett. **63**, 1047 (1993).

[77] J. Schmitz, J. Wagner, F. Fuchs, N. Herres, P. Koidl, and J. D. Ralston, J. Cryst. Growth **150**, 858 (1995).

[78] Q. Xue, T. Ogino, H. Kiyama, Y. Hasegawa, and T. Sakurai, J. Cryst. Growth **175/176**, 174 (1997).

[79] F. Maeda, M. Sugiyama, and Y. Watanabe, Phys. Rev. B **62**, 1615 (2000).

[80] J. Robertson, Eur. Phys. J. Appl. Phys. **28**, 256-291 (2004).

[81] K. Mistry, C. Allen, C. Auth, B. Beattie, D. Bergstrom, M. Bost, M. Brazier, M. Buehler, A. Cappellani, R. Chau, C.-H. Choi, G. Ding, K. Fischer, T. Ghani, R. Grover, W. Han, D. Hanken, M. Hattendorf, J. He, J. Hicks , R. Huessner, D. Ingerly, P. Jain, R. James, L. Jong, S. Joshi, C. Kenyon, K. Kuhn, K. Lee, H. Liu, J. Maiz, B. McIntyre, P. Moon, J. Neirynck, S. Pae, C. Parker, D. Parsons, C. Prasad, L. Pipes, M. Prince, P. Ranade, T. Reynolds, J. Sandford, L. Shifren, J. Sebastian, J. Seiple, D. Simon, S. Sivakumar, P. Smith, C. Thomas, T. Troeger, P. Vandervoorn, and S. Williams, K. Zawadzki, *A 45 nm Logic Technology with High-κ+Metal Gate Transistors, Strained Silicon, 9 Cu Interconnect Layers, 193 nm Dry Patterning, and 100 % Pb-free Packaging,* Electron Devices Meeting, 2007, IEDM 2007, 247-250 (2007).

[82] H. Hasegawa, Jpn. J. Appl. Phys. **38**, 1098 (1999).

[83] H. Hasegawa, L. He, H. Ohno, T. Sawada, T. Haga, Y. Abe, and H. Takahashi, J. Vac. Sci. Technol. B **5**, 1097 (1987).

[84] M. Hong, J. Kwo, A. R. Kortan, J. P.Mannaerts, and A. M. Sergent, Science **283**, 1897 (1999).

[85] M. J. Hale, S. I. Yi, J. Z. Sexton, A. C. Kummel, and M. Passlack, J. Chem. Phys. **119**, 6719 (2003).

[86] W. Schottky, Z. Phys. **118**, 539 (1942).

[87] J. L. Freeouf, and J. M. Woodall, Appl. Phys. Lett. **39**,727 (1981).

[88] L. J. Brillson, M. L. Slade, R. E. Vitturo, M. K. Kelly, N. Tache, G. Margaritondo, J. M. Woodall, P. D. Kirchner, G. D. Pettit, and S. L. Wright, Appl. Phys. Lett. **48**, 1458 (1986)

[89] S. D. Offsey, J. M. Woodall, A. C. Warren, P. D. Kirchner, T. I. Chappel, and G. D. Pettit, Appl. Phys. Lett. **48**, 475 (1986).

[90] J. Bardeen, Phys. Rev. **71**, 717 (1947).

[91] A. M. Cowley, and S. M. Sze, J. Appl. Phys. **36**, 3212 (1965).

[92] V. Heine, Phys. Rev. **138,** 1689 (1965).

[93] W. E. Spicer, I. Lindau, P. Skeath, C. Y. Su, and P. Chye, Phys. Rev. Lett. **44**, 420 (1980).

[94] W. E. Spicer, P. W. Chye, P. R. Skeath, C. Y. Su, and I. Lindau, J. Vac. Sci. Technol. **16**, 1422 (1979).

[95] W. E. Spicer, Z. Liliental-Weber, E. Weber, and N. Newman, J. Vac. Sci. Technol. B **6**, 1245 (1988).

[96] H. Hasegawa and H. Ohno, J. Vac. Sci. Technol. B **4**, 1130 (1986).

[97] W. Mönch, Phys. Rev. Lett. **58**, 1260 (1987).

[98] W. Mönch, Surf. Sci. **300**, 928 (1994).

[99] J. Tersoff and W. A. Harrison, Phys. Rev. Lett. **58**, 2367 (1987).

[100] J. Tersoff, Phys. Rev. Lett. **52**, 465 (1984).

[101] J. Robertson, Appl. Phys. Lett. **94**, 152104 (2009).

[102] L. Lin, and J. Robertson, J. Vac. Sci. Technol. B **30**, 04E101 (2012).

[103] P.D. Ye, J. Vac. Sci. Technol. A **26(4)**, 697 (2008).

[104] H. Hasegawa, and T. Sawada, Thin Solid Films, **103**, 119-140 (1983).

[105] H. Hasegawa, T. Sato, S. Kasai, B. Adamowicz, and T. Hashizume, Solar Energy **80**, 629-644 (2006).

[106] W. Walukiewicz, Appl. Phys. Lett. **54**, 2094 (1989).

[107] W. Walukiewicz, J. Vac. Sci. Technol. B **6**, 1257 (1988).

[108] W. Walukiewicz, Phys. Rev. B **30**, 4760 (1988).

[109] Y.G. Xie, S. Kasai, H. Takahashi, C. Jiang, H. Hasegawa, IEEE Electron Device Lett. **22,** 645 (2001).

[110] H.-S. Kim, I. Ok, M. Zhang, T. Lee, F. Zhu, L. Yu, J.C. Lee, Appl. Phys. Lett. **89** 222903 (2006).

[111] I. Ok, H.-S. Kim, M. Zhang, C.Y. Kang, S.J. Rhee, C. Choi, S.A. Krishnan, T. Lee, F. Zhu, G. Thareja, J.C. Lee, IEEE Electron Device Lett. **27**, 145 (2006).

[112] S. Koveshnikov, W. Tsai, I. Ok, J.C. Lee, V. Torkanov, M. Yakimov, S. Oktyabrsky, Appl. Phys. Lett. **88,** 022106 (2006).

[113] S.J. Koester, E.W. Kiewra, Y. Sun, D.A. Neumayer, J.A. Ott, M. Copel, D.K. Sadana, D.J. Webb, J. Fompeyrine, J.-P. Locquet, C. Marchiori, M. Sousa, R. Germann, Appl. Phys. Lett. **89,** 042104 (2006).

[114] S. Oktyabrsky, V. Tokranov, M. Yakimov, R. Moore, S. Koveshnikov, W. Tsai, F. Zhu, J.C. Lee, Mater. Sci. Eng. B**135,** 272 (2006).

[115] C. J. Sandroff, R. N. Nottenberg, J. C. Bischoff, and R. Bhat, Appl. Phys. Lett. 51, **33** (1987).

[116] C. J. Sandroff, M. S. Hegde, L. A. Farrow, C. C. Chang, and J. P. Harbison, Appl. Phys. Lett. **54**, 362 (1989).

[117] B. J. Skromme, C. J. Sandroff, E. Yablonovitch, and T. Gmitter, Appl. Phys. Lett. **51**, 2022 (1987).

[118] E. Yablonovitch, C. J. Sandroff, R. Bhat, and T. Gmitter, Appl. Phys. Lett. **51**, 439 (1987).

[119] G. Eftekhari, Vacuum **67**, 81-90 (2002).

[120] C. Merckling, Y.C. Chang, C.Y. Lu, J. Penaud, G. Brammertz, M. Scarrozza, G. Pourtois, J. Kwo, M. Hong, J. Dekoster, M. Meuris, M. Heyns, M. Caymax, Surf. Sci. **605,** 1778-1783 (2011).

[121] M. Passlack, M. Hong, and J. P. Mannaerts, Appl. Phys. Lett. **68**, 1099 (1996).

[122] M. Passlack, M. Hong, J. P. Mannaerts, R. L. Opila, S. N. G. Chu, N. Moriya, F. Ren, and J. R. Kwo, IEEE Trans. Electron Devices **44**, 214 (1997).
[123] M. Hong, J. Kwo, A. R. Kortan, J. P. Mannaerts, and A. M. Sergent, Science **283**, 1897 (1999).
[124] F. Ren, M. Hong, W.S. Hobson, J.M. Kuo, J.R. Lothian, J.P. Mannaerts, J. Kwo, S.N.G. Chu, Y.K. Chen, A.Y. Cho, Solid-State Electron. **41**, 1751 (1997).
[125] Y. C. Wang, M. Hong, J. M. Kuo, J. P. Mannaerts, J. Kwo, H. S. Tsai, J. J. Krajewski, Y. K. Chen, and A. Y. Cho, IEEE Electron Device Lett. **20**, 457 (1999).
[126] F. Ren, J. M. Kuo, M. Hong, W. S. Hobson, J. R. Lothian, J. Lin, H. S. Tsai, J. P. Mannaerts, J. Kwo, S. N. G. Chu, Y. K. Chem, and A. Y. Cho, IEEE Electron Device Lett. **19**, 309 (1998).
[127] Y. C. Wang, M. Hong, J. M. Kuo, J. P. Mannaerts, H. S. Tsai, J. Kwo, J. J. Krajewski, Y. K. Chen, and A. Y. Cho, Electron. Lett. **35**, 667 (1999).
[128] B. Yang, P.D. Ye, J. Kwo, M. R. Frei, H.-J. L. Gossmann, J. P. Mannaerts, M. Sergent, M. Hong, K. Ng, and J. Bude, J. Cryst. Growth **251**, 837 (2003).
[129] P. D. Ye, G. D. Wilk, J. Kwo, B. Yang, H.-J. L. Gossmann, M. Frei, S. N. G. Chu, J. P. Mannaerts, M. Sergent, M. Hong, K. Ng, and J. Bude,, IEEE Electron Device Lett. **24**, 209 (2003).
[130] P. D. Ye, G. D. Wilk, B. Yang, J. Kwo, S. N. G. Chu, S. Nakahara, H.-J. L. Gossmann, J. P. Mannaerts, M. Hong, K. K. Ng, and J. Bude, Appl. Phys. Lett. **83**, 180 (2003).
[131] P. D. Ye, G. D. Wilk, B. Yang, J. Kwo, H.-J. L. Gossmann, M. Hong, K. Ng, and J. Bude, Appl. Phys. Lett. **84**, 434 (2004).
[132] P. D. Ye, G. D. Wilk, B. Yang, S. N. G. Chu, K. K. Ng, and J. Bude, Solid-State Electron. **49**, 790 (2005).
[133] P. D. Ye, B. Yang, K. Ng, J. Bude, G. D. Wilk, S. Halder, and J. C. M. Hwang, Appl. Phys. Lett. **86**, 063501 (2005).
[134] Y. Xuan, H. C. Lin, P. D. Ye, and G. D. Wilk, Appl. Phys. Lett. **88**, 263518 (2006).
[135] Y. Xuan, H. C. Lin, and P. D. Ye, ECS Trans. **3**, 59 (2006).

[136] Y. Xuan, H. C. Lin, and P. D. Ye, IEEE Trans. Electron Devices **54**, 1811 (2007).

[137] Y. Q. Wu, T. Shen, P. D. Ye, and G. D. Wilk, Appl. Phys. Lett. **90**, 143504 (2007).

[138] T. Yang, Y. Xuan, D. Zemlyanov, T. Shen, Y. Q. Wu, J. M. Woodall, P. D. Ye, F. S. Aguirre-Tostado, M. Milojevic, S. McDonnell, and R. M. Wallace, Appl. Phys. Lett. **91**, 142122 (2007).

[139] M. M. Frank, G. D. Wilk, D. Starodub, T. Gustafsson, E. Garfunkel, Y. J. Chabal, J. Grazul, and D. A. Muller, Appl. Phys. Lett. **86**, 152904 (2005).

[140] M. L. Huang, Y. C. Chang, C. H. Chang, Y. J. Lee, P. Chang, J. Kwo, T. B. Wu, and M. Hong, Appl. Phys. Lett. **87**, 252104 (2005).

[141] C. H. Chang, Y. K. Chiou, Y. C. Chang, K. Y. Lee, T. D. Lin, T. B. Wu, M. Hong, and J. Kwo, Appl. Phys. Lett. **89**, 242911 (2006).

[142] M. Zhu, C. H. Tung, and Y. C. Yeo, Appl. Phys. Lett. **89**, 202903 (2006).

[143] H. L. Lu, L. Sun, S. J. Ding, M. Xu, D. W. Zhang, and L. K. Wang, Appl. Phys. Lett. **89**, 152910 (2006).

[144] G. K. Dalapati, Y. Tong, W. Y. Loh, H. K. Mun, and B. J. Cho, IEEE Trans. Electron Devices **54**, 1831 (2007).

[145] D. Shahrjerdi, E. Tutuc, and S. Banerjee, Appl. Phys. Lett. **91**, 063501 (2007).

[146] B. Shin, D. Choi, J. S. Harris, and P. C. McIntyre, Appl. Phys. Lett. **93**, 052911 (2008).

[147] P. C. McIntyre, Y. Oshima, E. Kim, and K. C. Saraswat, Microelectron. Eng. **86**, 1536 (2009).

[148] H. Ko, K. Takei, R. Kapadia, S. Chuang, H. Fang, P. W. Leu, K. Ganapathi, E. Plis, H. S. Kim, S.-Y. Chen, M. Madsen, A. C. Ford, Y.-L. Chueh, S. Krishna, S. Salahuddin, and A. Javey, Nature **468**, 286 (2010).

[149] https://www.maxlab.lu.se

[150] G. Ertl, J. Krüppers, *Low Energy Electrons and Surface Chemistry, 2nd edition*, VCH Verlagsgesellschaft, (1985).

[151] N. W. Ashcroft, N. D. Mermin, *Solid State Physics*, HRW International Edition, (1987).

[152] M. A. Van Hove, W. H. Weinberg, and C. -M. Chan, *Low Energy Electron Diffraction, Experiment, Theory, and Surface Structure Determination*, Springer-Verlag (1986).

[153] W.N. Unertl, *Handbook of Surface Science*, Physical Structure, Vol. 1, Elsevier (1996).

[154] *Semiconductor Research: Experimental Techniques*, edited by Amalia Patanè, and Naci Balkan, Springer (2012).

[155] G. Binnig, H. Rohrer, C. Gerber, E. Weibel, Appl. Phys. Lett. **40**, 178 (1982).

[156] G. Binnig, H. Rohrer, C. Gerber, E. Weibel, Phys. Rev. Lett. **49**, 57 (1982).

[157] L. Esaki, Phys. Rev. **109**, 603 (1958).

[158] R. Wiesendanger, *Scanning Probe Microscopy and Spectroscopy, Methods and Applications*, Cambridge University Press (1994).

[159] J. Bardeen, Phys. Rev. Lett. **6 (2)**, 57 - 59 (1961).

[160] J. Tersoff, and D. R. Hamann, Phys. Rev. B **31**, 805 (1985).

[161] M. Ahola-Tuomi, P. Laukkanen, M. P. J. Punkkinen, M. Kuzmin, R. E. Perälä, I. J. Väyrynen, K. Schulte and M. Pessa, Appl. Phys. Lett. **92,** 011926 (2008).

[162] H. Hertz, Ann. Phys. **17**, 983 (1887).

[163] A. Einstein, Ann. Physik **31**, 132 (1905).

[164] A. D. Baker, D. Betteridge, *Photoelectron Spectroscopy: Chemical and Analytical Aspects*, Pergamon Press (1972).

[165] A. R. Williams, N. D. Lang, Phys. Rev. Lett. **40**, 954 (1978).

[166] G. Margaritondo, *Introduction to Synchrotron Radiation,* Oxford University Press (1988).

[167] C. N. Berlung, W. E. Spicer, Phys. Rev. **136**, A 1030 (1964).

[168] C. N. Berlung, W. E. Spicer, Phys. Rev. **136**, A 1044 (1964).

[169] R. Z. Bachrach, *Synchrotron Radiation Research, Advances in Surface and Interface Science, Vol. 1*, Plenum Press, New York (1992).

[170] C. R. Brundle, and A. D. Baker, *Electron Spectroscopy: Theory, Techniques, and Applications, Vol. 1*, Academic Press, New York (1977).

[171] C. R. Brundle, and A. D. Baker, *Electron Spectroscopy: Theory, Techniques, and Applications, Vol. 2*, Academic Press, New York (1978).

[172] M. Cardona, and L. Ley, *Photoemission in Solids, Vol. 2,* Springer-Verlag, Berlin (1978).

[173] S. D. Kevan, *Angle Resolved Photoemission-Theory and Current Applications*, Elsevier Science, Amsterdam, (1992).

[174] I. Lindau, and W. E. Spicer, *Synchrotron Radiation Research*, edited by H. Winick and S. Doniach, Plenum Press, New York (1980).

[175] J. C. Fuggle and S. Alvarado, Physical Review A, **22,** 1615 (1980).

[176] J. J. Joyce, M. Del Giudice, J. H. Weaver, J. El. Spec. **49,** 3145 (1989).

[177] D. A. Shirley, Phys. Rev. B **5**, 4709 (1972).

[178] P. H. Citrin, G. K. Wertheim, Y. Baer, Phys. Rev. Lett. **41**, 1425 (1978).

[179] W. F. Egelhoff, Jr., Surf. Sci. Rep. **6**, 253 (1987).

[180] A. Flodström, R. Nyholm, and B. Johansson, *Advantages in Surface and Interface Science, Volume I: Techniques*, Plenum Press, New York (1992).

[181] G. D. Gilliland, Mat. Sci. and Eng., **R. 18,** 99-400 (1997).

[182] D. K. Schroder, *Semiconductor Material and Device Characterization, Third Edition,* John Wiley & Sons Inc. (2006).

[183] R. L. Puurunen, J. Appl. Phys. **97,** 121301 (2005).

[184] A. A. Katsnelson, V. S. Stepanyuk, A. I. Szász, O. V. Farberovich, *Computational Methods in Condensed Matter: Electronic Structure*, American Institute of Physics (1992).

[185] R. M. Martin, *Electronic Structure, Basic Theory and Practical Methods*, Cambridge University Press (2004).

[186] Born M, Oppenheimer J. R, Ann. Physik **48**, 457 (1927).

[187] P. Hohenberg, W. Kohn, Phys. Rev. **136**, B864 (1964).

[188] W. Kohn, L. J. Sham, Phys. Rev. **140**, A1133 (1965).

[189] J. P. Perdew, A. Zunger, Phys. Rev. B **23**, 5048 (1981).

[190] D. M. Ceperley, B. J. Alder, Phys. Rev. Lett. **45**, 566 (1980).

[191] D. C. Langreth, J. P. Perdew, Phys. Rev. B. **21**, 5469 (1980).

[192] J. P. Perdew, J. A. Chevary, S. H. Vosko, K. A. Jackson, M. R. Pederson, D. J. Singh, C. Fiolhais, Phys. Rev. B **46**, 6671 (1992).

[193] J. P. Perdew, K. Burke, M. Ernzerhof, Phys. Rev. Lett. **77**, 3865 (1996).

[194] J. Heyd, J. E. Peralta, G. E. Scuseria, and R. L. Martin, J. Chem. Phys. **123**, 174101 (2005).

[195] I. N. Yakovkin, and P. A. Dowben, Surf. Rev. and Lett. **14**, 481 (2007).

[196] J. Heyd, G.E. Scuseria, M. Ernzerhof, J. Chem. Phys. **118**, 8207 (2003).

[197] F. Tran, and P. Blaha, Phys. Rev. Lett. **102**, 226401 (2009).

[198] G. Kresse and J. Hafner, Phys. Rev. B **47**, 558 (1993).

[199] G. Kresse and J. Hafner, Phys. Rev. B **49**, 14251 (1994).

[200] G. Kresse and J. Furthmüller, Comput. Mat. Sci. **6**, 15 (1996).

[201] G. Kresse and J. Furthmüller, Phys. Rev. B **54**, 11169 (1996).

[202] D. Vanderbilt, Phys. Rev. B **41**, 7892 (1990).

[203] P. E. Blöchl, Phys. Rev. B **50**, 17953 (1994).

[204] G. Kresse and D. Joubert, Phys. Rev. B **59**, 1758 (1999).

[205] http://cms.mpi.univie.ac.at/vasp/vasp/

[206] P. Laukkanen, M. P. J. Punkkinen, N. Räsänen, M. Ahola-Tuomi, M. Kuzmin, J. Lång, J. Sadowski, J. Adell, R. E. Perälä, M. Ropo, K. Kokko, L. Vitos, B. Johansson, M. Pessa, and I. J. Väyrynen, Phys. Rev. B **81,** 035310 (2010).

[207] M. P. J. Punkkinen, P. Laukkanen, K. Kokko, M. Ropo, M. Ahola-Tuomi, I. J. Väyrynen, H.-P. Komsa, T. T. Rantala, M. Pessa, M. Kuzmin, L. Vitos, J. Kollár, and B. Johansson, Phys. Rev. B **76**, 115334 (2007)

[208] M. P. J. Punkkinen, K. Kokko, L. Vitos, P. Laukkanen, E. Airiskallio, M. Ropo, M. Ahola-Tuomi, M. Kuzmin, I. J. Väyrynen, and B. Johansson, Phys. Rev. B **77**, 245302 (2008).

[209] C.-A. Chang, M. Heiblum, R. Ludeke, M.I. Nathan, Appl. Phys. Lett. **39**, 229 (1981).

[210] G.S. Petrich, A.M. Dabiran, P.I. Cohen, Appl. Phys. Lett. **61**, 162 (1992).

[211] M.B. Panish, R.A. Hamm, L.C. Hopkins, Appl. Phys. Lett. **56**, 2301 (1990).

[212] J.J. Harris, B.A. Joyce, P.J. Dobson, Surf. Sci. **103,** L90 (1981).

[213] A. Ohtake, J. Nara, T. Yasuda, N. Miyata, Phys. Rev. B **77**, 195309 (2008).

[214] V. Emiliani, A.I. Shkrebtii, C. Goletti, A.M. Frisch, B.O. Fimland, N. Esser, W. Richter, Phys. Rev. B **59,** 10657 (1999).

[215] D. Usanmaz, M. Çakmak, Ş. Ellialtıoğlu, Surf. Sci. **603,** 2683 (2009).

[216] U. Resch-Esser, N. Esser, C. Springer, J. Zagenhagen, W. Richter, M. Cardona, and B. O. Fimland, J. Vac. Sci. Technol. B **13**, 1672 (1995).

[217] M. Batzill, and U. Diebold, Progr. Surf. Sci. **79,** 47 (2005).

[218] J. L. Gole, and Z. L. Wang, Nano Lett. **8**, 449 (2001).

[219] B. Kumar, D. H. Lee, S. H. Kim, B. Yang, S. Maeng, and S.-W. Kim, J. Phys. Chem. C **114**, 11050 (2010).

[220] R. Sanjinés, C. Coluzza, D. Rosenfeld, F. Gozzo, Ph. Alméras, F. Lévy, and G. Margaritondo, J. Appl. Phys. **73**, 3997 (1993).

[221] G. Gaggiotti, A. Galdikas, S. Kačiulis, G. Mattogno, and A. Šetkus, J. Appl. Phys. **76**, 4467 (1994).

[222] J. A. Caraveo-Frescas, P. K. Nayak, H. A. Al-Jawhari, D. B. Granato, U. Schwingenschlögl, and H. N. Alshareef, ACS Nano (2013) (in press).